THE UNIVERSITY OF CHICAGO

DESIGN AND SYNTHESIS OF COLLOIDAL METALLIC NANOSTRUCTURES FOR PROGRAMMABLE SELF-ASSEMBLY

A DISSERTATION SUBMITTED TO

THE FACULTY OF THE DIVISION OF THE PHYSICAL SCIENCES

IN CANDIDACY FOR THE DEGREE OF

DOCTOR OF PHILOSOPHY

DEPARTMENT OF CHEMISTRY

BY

KYLE JOSEPH GIBSON

CHICAGO, ILLINOIS

DECEMBER 2018

This thesis is dedicated to my family.

TABLE OF CONTENTS

List of Figures

List of Tables

Acknowledgments

I would like to start by thanking my advisor, Yossi Weizmann, for his continuous support over the course of my graduate research. Yossi was willing to take a chance on me as a student with no experience in the field and teach me the ropes. He offered so many project ideas to me over the years and allowed me all the freedom to work on the projects that I was most interested in working on. His guidance truly shaped me into the scientist, researcher, and teacher that I am today, and for that I am eternally grateful.

I would also like to thank the professors and technicians that made my research at the University of Chicago possible. To my candidacy committee, Joseph Piccirilli, Ray Moellering, and Chuan He for directing me and my research, guiding me to become a better student. To my thesis committee, Luping Yu and Bozhi Tian, for the guidance especially at the end of my graduate career. To Yimei Chen and Joe Austin for all their help in the TEM facility, where I spent countless hours over the years. And to all other professors who have offered aid and guidance to research, writing, and anything and everything else.

To all the friends I have made since moving to Chicago, thank you for making the experience all that it was. From the very first day, I have always felt like I had a home in Chicago thanks to all the friends I had here.

To my family, especially my dad, thank you for all the support over the years, not just in graduate school. I obviously could not be where I am today without your love and support.

To my loving girlfriend Jenny, I am so glad that my time in Chicago brought us together. I cannot imagine my life without you. It takes an incredible person to ask a graduate student every single day about how work was. You are that special person to me who makes an otherwise boring life exciting every single day, and it makes me so happy that I get to share my life with you.

Abstract

Reliability and predictability in methods that produce pure, consistent, and monodisperse products is a hallmark in all aspects of chemistry. Within the subfields of nanomaterials and nanotechnology, due to the relatively short amount of time these areas of chemistry have had research dedicated to their study, there is room for improvement in the methods and techniques that are often used to synthesize these materials. I have been working on two aspects in this area of chemistry: to improve upon the synthetic techniques and mechanistic understandings of nanoparticle growth and to greatly expand the capabilities of discrete programmable self-assembly with highly uniform and robust universal building blocks. First, a purification technique known as depletion flocculation is demonstrated to purify gold bipyramids from the crude synthetic mixture containing roughly 70% shape impurities. The flocculation was shown possible owing to the use of benzyldimethylammonium chloride (BDAC) surfactant. The purified bipyramids were then used for further nanocrystal growth to create a new class of nanoparticles based on the original bipyramid seed. The bipyramids were also oxidized in the presence of surfactant at high temperatures to form highly monodisperse low aspect-ratio nanorods. The final structures of both the growth and oxidation procedures were shown to be highly dependent on the surfactant present in solution.

Second, universal building blocks for the purpose of discrete programmable self-assembly were synthesized by a two-step procedure. A partial polymer encapsulation is performed in a binary solvent system in combination with a dual ligand functionalization. The surface energy of the nanoparticle is tuned by coating with a specific ratio of hydrophobic ligand to hydrophilic ligand that dictates the eventual surface coverage of the diblock copolymer. The coverage of the nanoparticle surface by the polymer renders that area inert to further functionalization. The second

step involves the functionalization of the exposed surface by thiolated single-stranded DNA. The polymer confers site-specific and directional binding of the DNA, and the DNA allows for specific binding only to the complementary strand. This enables self-assembly between two nanoparticles functionalized with complementary DNA strands in a highly specific and preconceived fashion into discrete assemblies with exceptional control. I demonstrate 24 self-assemblies with the universal building blocks, many of which are not possible through any other self-assembly method. Finally, I show that the self-assembled structures can be functionalized with a stimuli-responsive DNA sequence. Specifically, in response to the pH of the solution, the triplex-capable DNA strand changes the interparticle distance, invoking an optical plasmonic response.

Chapter 1 – Introduction

1.1 The basics of nanomaterials

Nanomaterials are a class of materials that lies in a specific size regime, that is, between 1 and 100 nm. This size scale rests between that of atoms (typically 1 angstrom or 10^{-10} meters) and what is known as bulk, anything about 1 micron (10^{-6} meters) or larger. While both atomic chemistries and bulk chemistries have been studied for hundreds or even thousands of years, nanomaterials went largely unnoticed until the last few decades. However, this does not imply that nanomaterials as a whole did not exist, rather that they were not recognized or understood. Probably the oldest example of a nanomaterial in the world is the Ancient Roman relic the Lycurgus Cup[1]. This 4th-century AD cup was made with glass infused with gold-silver alloy nanoparticles. The optical properties of the nanoparticles grant the cup with a red color when viewed with light transmitted through the glass and a green color with light reflected off this glass. It wasn't for 1,600 years though before it was actually understood why the gold and silver infused in the glass would show the colors in the cup when traditionally gold and silver would appear as just that, gold and silver.

This introduces one of the most studied aspects of nanomaterials and that is their optical properties. These properties fall under two umbrellas, the quantum confinement associated with semi-conductor materials and surface plasmons associated with noble metal materials. Semi-conductor nanomaterials are also referred to as quantum dots, and themselves make up an incredibly deep and interesting field of study. However, this field lies distinct from the work presented in this thesis and will not be discussed in any detail.

Surface plasmons of noble metal nanomaterials, which include the gold-silver nanoparticles present in the Lycurgus Cup, are described as an oscillation of the electrons in the

conduction band[2]. For gold and silver nanoparticles, this oscillation frequency lies within the visible light spectrum, which gives rise to the plasmon resonance absorption. For example, most spherical gold nanoparticles exhibit an absorption peak between about 520 nm and 570 nm, which results in a characteristic red color[3]. The exact position of the absorption peak depends on several factors, most obvious and most measurable probably being the size of the nanoparticle. The larger the nanoparticle, the more red-shifted the absorption peak will be, that is, absorbing light of longer wavelengths. However, the absorption profile gets more complex and more interesting when dealing with nanoparticles of anisotropic shape.

Gold nanoparticle syntheses entered the modern scientific era in 1857 from Michael Faraday as a result of extensive series of studies on noble metals[4]. But it wasn't until the 1980's when the actual synthetic protocols were beginning to be explored. All early protocols focused on the creation of simple spherical nanoparticles. The first synthesis of an anisotropic nanoparticle came from the group of Catherine Murphy[5]. Using a seed-mediated synthesis in a solution of a cationic surfactant and a mild reducing agent, the group was able to synthesize, in a rather low yield, cylindrical gold nanorods. This protocol became the basis for an explosive number of methods to make an array of different shapes of various metallic make-ups.

The anisotropic shape present in the gold nanorod grants a platform to understand the intricacies of plasmonic absorptions. An absorption peak occurs when a light wave is absorbed after interacting with the nanoparticle. For a spherical nanoparticle, any light wave interacting with the nanoparticle will essentially "see" the nanoparticle along an identical axis to any other. For anisotropic shapes, such as a nanorod, multiple modes have to be considered. In the case of the nanorod, there are two axes that correspond to the length and to the width of the nanorod. When a light wave is traveling along the long axis of the nanorod, it causes a perpendicular oscillation of

the electrons. Likewise, a lightwave traveling through the width of the nanorod will cause an electron oscillation in the perpendicular direction. These two modes are known as the longitudinal and transverse plasmons, respectively, and they are reflected as separate peaks in the absorption peaks. For nanorods, the transverse absorbance peak is typically a small peak around 520 nm and the longitudinal absorbance peak is red-shifted and larger in intensity. Absorption profiles will change as the size and shape of the nanoparticle as well as the metallic makeup of the particle. The majority of modern nanoparticle synthesis research focuses on improving the yield and monodispersity of nanoparticles, new shapes to improve upon the desirable properties of the nanomaterials, and simplifying synthetic conditions[3, 6].

1.2 The basics of self-assembly

Another hallmark of nanomaterials lies within their self-assembly, specifically that nanoparticles can interact with each other when in close proximity. These interactions provide the motivation for researchers to develop new methods to assemble nanoparticles into pre-defined and controllable configurations[7, 8]. Much like in organic chemistry where atoms can be configured together into molecules to create an incredible array of properties, assembly of nanoparticles offers the opportunity to create something more than that of the constituent pieces[2]. Current limitations of traditional methods are mainly related to the precise size and arrangement of building blocks on the nano- or molecular- scale. By designing particles to arrange themselves via self-assembly, researchers have improved control over the synthesis of these size-scales and look to increase the diversity and programmability of different building block materials, such as metallic nanoparticles[9] or biological molecules[10].

Programmable self-assembly offers tools toward the construction of discrete structures, especially those on the nanoscale that would otherwise be impossible to make. These self-

assembled structures are capable of variety of uses ranging from nanomachinery, high-resolution sensing, detailed microscopy, high-performance optics and thermics, and any combination thereof. When combined with hyperspectral microscopy, self-assembled nanoparticles provide a unique tool for studying cellular activity and characteristics. Combining the nanoparticles with other functional materials, such as certain DNA motifs, allows for utilization of the unique absorbance properties of gold nanoparticles to sense certain solution conditions or the presence of other molecules. The use of multi-functional and fully customizable sensors would be a powerful tool for intracellular studies.

The field of nanoparticle self-assembly originated in 1996 with reports from Chad Mirkin and Paul Alivisatos showing DNA-functionalization of gold nanoparticles[11, 12]. These reports showed the use of DNA as a ligand on nanoparticles grants controllable, rational, and reversible assembly of colloidal nanoparticles. Now two decades later, DNA still represents the most powerful ligand in the field of programmable self-assembly. The promising use of DNA as a robust and predictable material has resulted in many subsequent reports showed its value. Application-based sensors mainly on DNA targets[13, 14, 15] and heavy metal ions[16] have been a large target for these types of assemblies. Additionally, advancing technology in the synthesis of designer DNA strands has greatly expanded the possibilities and ease of obtaining the thiolated-DNA strands used in gold nanoparticle self-assemblies. Another common self-assembly target is in the creation of core-satellite particle systems where one large nanoparticle is tethered isotropically to several smaller ones through DNA[17]. Similarly, core-satellite structures have since been expanded upon recently to include changing the central core to anisotropic particles[18] as well as assembling particles of other metallic composition[19, 20, 21].

All early self-assembly systems were based on isotropic nanoparticles, while reliable synthetic techniques for anisotropic gold nanocrystals were not available for a few more years. As discussed above, in the early 2000's the first chemical syntheses of gold nanorods appeared, and this set the stage for the explosion of gold nanocrystal work on size and shape syntheses to generate novel shapes and structures. Since the synthesis of gold nanorods, other shapes such as nanobranches[22], nanoprisms[23], nanocubes[24, 25], octahedron[26], icosahedron[27], nanoplates[28], and many other shapes and various modulations on existing particles have been shown[6].

The use of spherical gold nanoparticles and creating reversible aggregates through DNA hybridization were a hallmark of the early self-assemblies. The self-assembly ultimately forms an aggregate that brings the gold nanoparticles within close proximity of one another that induces plasmonic coupling, causing a red shift in the nanoparticle absorption that is often easily detected by the eye[11, 29]. The formation of this large-scale aggregate is impossible to quantitate beyond simple UV-Vis absorption due to the way that the assembly grows in an uncontrollable manner. The creation of discrete and measurable structures is important to the advancement of the field so that nanoparticle interactions can be studied in greater detail. Some methods allow for some greater predictability in the synthesis of discrete nanoparticle assembly structures, but many limitations to these designs plague their ultimate application. One main strategy to is to employ a scaffold assembly that enables nanoparticles to be tethered to the scaffold. One of the first examples came froma joint report by Alivisatos and Seeman showing DNA tensegrity triangles as scaffolds to create two-dimensional assemblies with alternating small and large gold nanoparticles[30]. Furthermore, discrete hexagonal structures were assembled using DNA rings with rigid vertices[31], where the hexagons were assembled with singly functionalized nanoparticles where the DNA was encoded with two separate recognition sequences. The recognition sequences were complementary

to each other and the rigid synthetic vertex was positioned between them. Stepwise formation of the hexagons was shown possible through subsequent addition of each of the 6 nanoparticle-DNA hybrids. The same group also showed that a more universal design to create triangles, squares, trapezoids, and rectangles capable of using multiple sizes of nanoparticles was possible[32]. This method unfortunately required monofunctionalization of the nanoparticles, involved a difficult subsequent purification, and the gel purification caused the method to suffer from limited batch size and low yield. Pre-hybridizing thiolated DNA strands can offer a simple route to nanoparticle dimers from a design standpoint, but this technique requires exact stoichiometric control of the DNA and nanoparticles or alternatively the use of gel purification[33, 34, 35].

Thiol ligands have been found that binding to gold nanorods gives a slight preference to the tips because of the more stable bond to the {111} facet[36, 37], and by exploiting this slight preference, a thiolated ABA tri-block copolymer can assemble linear end-to-end nanorods in a water:dimethylformamide (DMF) mixture[38]. Likewise, end-to-end nanorod assemblies used for SERS measurements could be assembled using simple polystyrene polymer ligands functionalized solely at the tips[39]. However, the slight preference for one facet over another reveals that it is strictly required to add a stoichiometric amount of the ligand to prevent the ligand from simply covering the entire surface. Gold nanoparticles can also be tethered to the outside of a double-helical protein structure to create the analogous double-helical gold nanoparticle structure[40]. The use of polystyrene microspheres was used to make highly controllable and directional binding modes[41]. The microspheres were cross-linked to create a cluster, and the central portion of the cluster was filled in using polymerizing styrene to create largely inert portions where only the protruding areas could be further functionalized. The directionality of the functionalized patches allowed the creation of valence-bonding patterns with these colloidal microparticles. However,

control over micrometer-sized particles operates under different principles than analogous nanometer-sized particles. Additionally, control over the anisotropy of gold nanorods can be gained to some degree by introducing silica encapsulations[42]. However, this method has currently only been applied to gold nanorods by once again taking advantage of the stability of the {111} facet, so it is limited in its application to nanoparticles of other shapes.

Self-assemblies using ligands other than DNA or other biomolecules, while uncommon, have also been developed. As mentioned above, gold nanorods assembled end-to-end utilizing thiolated ligands composed of either polystyrene or triblock co-polymer have been demonstrated[38, 39]. Similarly, thiolated polystyrene ligands present on gold bipyramids can create vertically aligned "forests" on a substrate[43]. Side-to-side assemblies of Au-tipped CdSe nanorods can be deposited vertically on a substrate with the aid of hydrogen-bonding of the capping ligands and minimizing the interactions between the nonpolar ligands and the polar solvent[44].

Examples of superlattice self-assemblies capable of utilizing various nanoparticle shapes have also been demonstrated. These is significantly higher order in 3-dimensional superlattices than the typical aggregates that result standard self-assembly techniques employing complementary strand-labeled nanoparticles[45]. The use of different nanoparticle sizes also allows for different close-packing structures[46]. Superlattices that assemble into Wulff polyhedra can be created using a complex heating and cooling method, where the system is heated slightly above the DNA melting temperature and then cooled at a very slow rate[47]. The cooling rate was found to be the most integral piece to polyhedron formation in these systems. Though a vast number of self-assembly products of a variety of shapes and sizes can be synthesized, there still is no single, robust method for the creation of the building blocks necessary for large-scale, high yield, solution based, programmable self-assembly utilizing both isotropic and anisotropic nanoparticles.

1.3 Scope of thesis

My graduate research focuses primarily on the topics introduced above, namely the synthesis and purification of gold nanoparticles and programmable self-assembly of discrete nanostructures. Specifically, different techniques are explored to improve and simplify the procedures currently available to nanoparticle syntheses without sacrificing things like purity and polydispersity. Secondly, a method of partial polymer encapsulation is used to generate novel building blocks to be used for site-specific, directional discrete self-assemblies and the application of these structures.

In Chapter 2, I will discuss the work on purifying gold bipyramids. The synthetic procedure yields only 30% bipyramids amongst nanoparticles of other various shapes. The purified gold bipryamids can then be used as a seed to grow a new class of bipyramid-related structures that maintain the high purity and monodispersity of the seed nanoparticle. Furthermore, the growth conditions employed for the regrowth offers insight into the relationship between surfactant and the resultant shape.

In Chapter 3, I discuss the use of a partial polymer encapsulation method to create a number of new building blocks to be used for programmable self-assembly. The polymer renders a specific portion of the nanoparticle inert, allowing for a subsequent functionalization step that is both site-specific and directional. The procedure for encapsulation is universal and can be applied to any nanoparticle size and shape. The building blocks allow for a number of new self-assemblies not possible through any other method.

In Chapter 4, I use the simple discrete self-assemblies of nanospheres and nanorods to explore the optical properties of the system. The use of triplex-capable DNA strands allows for

rapid and reversible gap changes in the dimer assemblies, invoking plasmonic coupling between the nanoparticles.

In Chapter 5, I conclude the thesis by offering insight into how the research presented within stands in the field of nanotechnology and nanomaterials. I offer possibilities for future directions of the projects and how those could impact the field as a whole.

1.4 References

1. Freestone I, Meeks N, Sax M, Higgitt C. The Lycurgus Cup — A Roman nanotechnology. *Gold Bulletin* 2007, **40**(4)**:** 270-277.

2. Eustis S, El-Sayed MA. Why gold nanoparticles are more precious than pretty gold: noble metal surface plasmon resonance and its enhancement of the radiative and nonradiative properties of nanocrystals of different shapes. *Chemical society reviews* 2006, **35**(3)**:** 209-217.

3. Daniel M-C, Astruc D. Gold nanoparticles: assembly, supramolecular chemistry, quantum-size-related properties, and applications toward biology, catalysis, and nanotechnology. *Chemical reviews* 2004, **104**(1)**:** 293-346.

4. Edwards PP, Thomas JM. Gold in a metallic divided state—from faraday to present-day nanoscience. *Angewandte Chemie International Edition* 2007, **46**(29)**:** 5480-5486.

5. Jana NR, Gearheart L, Murphy CJ. Wet Chemical Synthesis of High Aspect Ratio Cylindrical Gold Nanorods. *The Journal of Physical Chemistry B* 2001, **105**(19)**:** 4065-4067.

6. Grzelczak M, Pérez-Juste J, Mulvaney P, Liz-Marzán LM. Shape control in gold nanoparticle synthesis. *Chemical Society Reviews* 2008, **37**(9)**:** 1783-1791.

7. Cademartiri L, Bishop KJM. Programmable self-assembly. *Nat Mater* 2015, **14**(1)**:** 2-9.

8. Jones MR, Seeman NC, Mirkin CA. Programmable materials and the nature of the DNA bond. *Science* 2015, **347**(6224).

9. Henzie J, Grünwald M, Widmer-Cooper A, Geissler PL, Yang P. Self-assembly of uniform polyhedral silver nanocrystals into densest packings and exotic superlattices. *Nature materials* 2012, **11**(2)**:** 131.

10. Hartgerink JD, Beniash E, Stupp SI. Self-assembly and mineralization of peptide-amphiphile nanofibers. *Science* 2001, **294**(5547)**:** 1684-1688.

11. Mirkin CA, Letsinger RL, Mucic RC, Storhoff JJ. A DNA-based method for rationally assembling nanoparticles into macroscopic materials. *Nature* 1996, **382**(6592)**:** 607-609.

12. Alivisatos AP, Johnsson KP, Peng X, Wilson TE, Loweth CJ, Bruchez Jr MP*, et al*. Organization of'nanocrystal molecules' using DNA. *Nature* 1996, **382**(6592)**:** 609-611.

13. Elghanian R, Storhoff JJ, Mucic RC, Letsinger RL, Mirkin CA. Selective Colorimetric Detection of Polynucleotides Based on the Distance-Dependent Optical Properties of Gold Nanoparticles. *Science* 1997, **277**(5329)**:** 1078-1081.

14. Storhoff JJ, Elghanian R, Mucic RC, Mirkin CA, Letsinger RL. One-Pot Colorimetric Differentiation of Polynucleotides with Single Base Imperfections Using Gold Nanoparticle Probes. *Journal of the American Chemical Society* 1998, **120**(9)**:** 1959-1964.

15. Taton TA, Mirkin CA, Letsinger RL. Scanometric DNA array detection with nanoparticle probes. *Science* 2000, **289**(5485)**:** 1757-1760.

16. Kim Y, Johnson RC, Hupp JT. Gold nanoparticle-based sensing of "spectroscopically silent" heavy metal ions. *Nano Letters* 2001, **1**(4)**:** 165-167.

17. Mucic RC, Storhoff JJ, Mirkin CA, Letsinger RL. DNA-directed synthesis of binary nanoparticle network materials. *Journal of the American Chemical Society* 1998, **120**(48)**:** 12674-12675.

18. Gandra N, Abbas A, Tian L, Singamaneni S. Plasmonic planet–satellite analogues: hierarchical self-assembly of gold nanostructures. *Nano letters* 2012, **12**(5)**:** 2645-2651.

19. Pal S, Sharma J, Yan H, Liu Y. Stable silver nanoparticle–DNA conjugates for directed self-assembly of core-satellite silver–gold nanoclusters. *Chemical Communications* 2009(40)**:** 6059-6061.

20. Choi I, Song HD, Lee S, Yang YI, Kang T, Yi J. Core–satellites assembly of silver nanoparticles on a single gold nanoparticle via metal ion-mediated complex. *Journal of the American Chemical Society* 2012, **134**(29)**:** 12083-12090.

21. Schreiber R, Do J, Roller E-M, Zhang T, Schuller VJ, Nickels PC*, et al*. Hierarchical assembly of metal nanoparticles, quantum dots and organic dyes using DNA origami scaffolds. *Nat Nano* 2014, **9**(1)**:** 74-78.

22. Hao E, Bailey RC, Schatz GC, Hupp JT, Li S. Synthesis and optical properties of "branched" gold nanocrystals. *Nano Letters* 2004, **4**(2)**:** 327-330.

23. Ha TH, Koo H-J, Chung BH. Shape-controlled syntheses of gold nanoprisms and nanorods influenced by specific adsorption of halide ions. *The Journal of Physical Chemistry C* 2007, **111**(3)**:** 1123-1130.

24. Kou X, Sun Z, Yang Z, Chen H, Wang J. Curvature-directed assembly of gold nanocubes, nanobranches, and nanospheres. *Langmuir* 2008, **25**(3)**:** 1692-1698.

25. Wu X, Ming T, Wang X, Wang P, Wang J, Chen J. High-photoluminescence-yield gold nanocubes: for cell imaging and photothermal therapy. *Acs Nano* 2009, **4**(1)**:** 113-120.

26. Zhang J, Gao Y, Alvarez-Puebla RA, Buriak JM, Fenniri H. Synthesis and SERS properties of nanocrystalline gold octahedra generated from thermal decomposition of HAuCl4 in block copolymers. *Advanced Materials* 2006, **18**(24)**:** 3233-3237.

27. Xu J, Li S, Weng J, Wang X, Zhou Z, Yang K, *et al*. Hydrothermal syntheses of gold nanocrystals: from icosahedral to its truncated form. *Advanced Functional Materials* 2008, **18**(2)**:** 277-284.

28. Luo Y. Large-scale preparation of single-crystalline gold nanoplates. *Materials Letters* 2007, **61**(6)**:** 1346-1349.

29. Storhoff JJ, Lazarides AA, Mucic RC, Mirkin CA, Letsinger RL, Schatz GC. What Controls the Optical Properties of DNA-Linked Gold Nanoparticle Assemblies? *Journal of the American Chemical Society* 2000, **122**(19)**:** 4640-4650.

30. Zheng J, Constantinou PE, Micheel C, Alivisatos AP, Kiehl RA, Seeman NC. Two-dimensional nanoparticle arrays show the organizational power of robust DNA motifs. *Nano letters* 2006, **6**(7)**:** 1502-1504.

31. Aldaye FA, Sleiman HF. Sequential Self-Assembly of a DNA Hexagon as a Template for the Organization of Gold Nanoparticles. *Angewandte Chemie International Edition* 2006, **45**(14)**:** 2204-2209.

32. Aldaye FA, Sleiman HF. Dynamic DNA templates for discrete gold nanoparticle assemblies: control of geometry, modularity, write/erase and structural switching. *Journal of the American Chemical Society* 2007, **129**(14)**:** 4130-4131.

33. Zanchet D, Micheel CM, Parak WJ, Gerion D, Alivisatos AP. Electrophoretic isolation of discrete Au nanocrystal/DNA conjugates. *Nano Letters* 2001, **1**(1)**:** 32-35.

34. Zanchet D, Micheel CM, Parak WJ, Gerion D, Williams SC, Alivisatos AP. Electrophoretic and structural studies of DNA-directed Au nanoparticle groupings. *The Journal of Physical Chemistry B* 2002, **106**(45)**:** 11758-11763.

35. Yao H, Yi C, Tzang C-H, Zhu J, Yang M. DNA-directed self-assembly of gold nanoparticles into binary and ternary nanostructures. *Nanotechnology* 2006, **18**(1)**:** 015102.

36. Pan B, Ao L, Gao F, Tian H, He R, Cui D. End-to-end self-assembly and colorimetric characterization of gold nanorods and nanospheres via oligonucleotide hybridization. *Nanotechnology* 2005, **16**(9)**:** 1776.

37. Burrows ND, Vartanian AM, Abadeer NS, Grzincic EM, Jacob LM, Lin W, *et al*. Anisotropic nanoparticles and anisotropic surface chemistry. *The journal of physical chemistry letters* 2016, **7**(4)**:** 632-641.

38. Nie Z, Fava D, Rubinstein M, Kumacheva E. "Supramolecular" assembly of gold nanorods end-terminated with polymer "pom-poms": effect of pom-pom structure on the association modes. *Journal of the American Chemical Society* 2008, **130**(11)**:** 3683-3689.

39. Lee A, Andrade GF, Ahmed A, Souza ML, Coombs N, Tumarkin E, *et al*. Probing dynamic generation of hot-spots in self-assembled chains of gold nanorods by surface-enhanced Raman scattering. *Journal of the American Chemical Society* 2011, **133**(19)**:** 7563-7570.

40. Chen C-L, Zhang P, Rosi NL. A new peptide-based method for the design and synthesis of nanoparticle superstructures: construction of highly ordered gold nanoparticle double helices. *Journal of the American Chemical Society* 2008, **130**(41)**:** 13555-13557.

41. Wang Y, Wang Y, Breed DR, Manoharan VN, Feng L, Hollingsworth AD, *et al*. Colloids with valence and specific directional bonding. *Nature* 2012, **491**(7422)**:** 51.

42. Wang F, Cheng S, Bao Z, Wang J. Anisotropic Overgrowth of Metal Heterostructures Induced by a Site-Selective Silica Coating. *Angewandte Chemie International Edition* 2013, **52**(39)**:** 10344-10348.

43. Shi Q, Si KJ, Sikdar D, Yap LW, Premaratne M, Cheng W. Two-dimensional bipyramid plasmonic nanoparticle liquid crystalline superstructure with four distinct orientational packing orders. *ACS nano* 2016, **10**(1)**:** 967-976.

44. Zhao N, Liu K, Greener J, Nie Z, Kumacheva E. Close-packed superlattices of side-by-side assembled Au-CdSe nanorods. *Nano letters* 2009, **9**(8)**:** 3077-3081.

45. Nykypanchuk D, Maye MM, Van Der Lelie D, Gang O. DNA-guided crystallization of colloidal nanoparticles. *Nature* 2008, **451**(7178)**:** 549.

46. Macfarlane RJ, Lee B, Jones MR, Harris N, Schatz GC, Mirkin CA. Nanoparticle superlattice engineering with DNA. *science* 2011, **334**(6053)**:** 204-208.

47. Auyeung E, Li TI, Senesi AJ, Schmucker AL, Pals BC, de La Cruz MO, *et al*. DNA-mediated nanoparticle crystallization into Wulff polyhedra. *Nature* 2014, **505**(7481)**:** 73-77.

Chapter 2 – Synthesis and Purification of Gold Bipyramids and Related Structures

2.1 Introduction

One of the core feature of nanomaterials and nanotechnology, as in most synthetic fields, is the ability the make consistent, monodisperse, and pure products. The emerging field of nanotechnology has shown a wide variety of potential applications, including surface-enhanced Raman spectroscopy (SERS), drug delivery and therapeutics, catalysis and non-linear optics[1, 2, 3, 4, 5]. The main interest in noble metal nanoparticles, in general, is due to their plasmonic responses and local field enhancements[6, 7, 8], both of which are tunable through the size, shape, and metallic make-up of the particles. However, the properties that make these nanoparticles both interesting and desirable suffer from loss of monodispersity that is frequently associated with various morphologies of nanoparticles, and typically get worse the more exotic the structure. Due to the structure- and size-dependent character of localized surface plasmon resonance and local field enhancement, precise control over the synthesis of nanostructures would allow for a variety of programmable designs and highly tunable optical properties of the materials. In addition, the ability to attain monodisperse colloidal nanoparticles in high yield is a critical step in the development of the product toward eventual widespread use. Theoretical calculations predict stronger local field enhancement for bipyramids than in nanorods or other common shapes due to the sharpness of the tips[9]. It is for these reasons for the interest in gold bipyramids, which have shown remarkable size and shape monodispersity. However, the first synthetic approaches could only yield roughly 30% bipyramids in terms of shape purity, with the other shape impurities being pseudo-spherical (~60%) and rods (~10%)[10]. The yield could be improved by using quaternary ammonium surfactants with larger headgroups, such as cetyltributylammonium bromide,

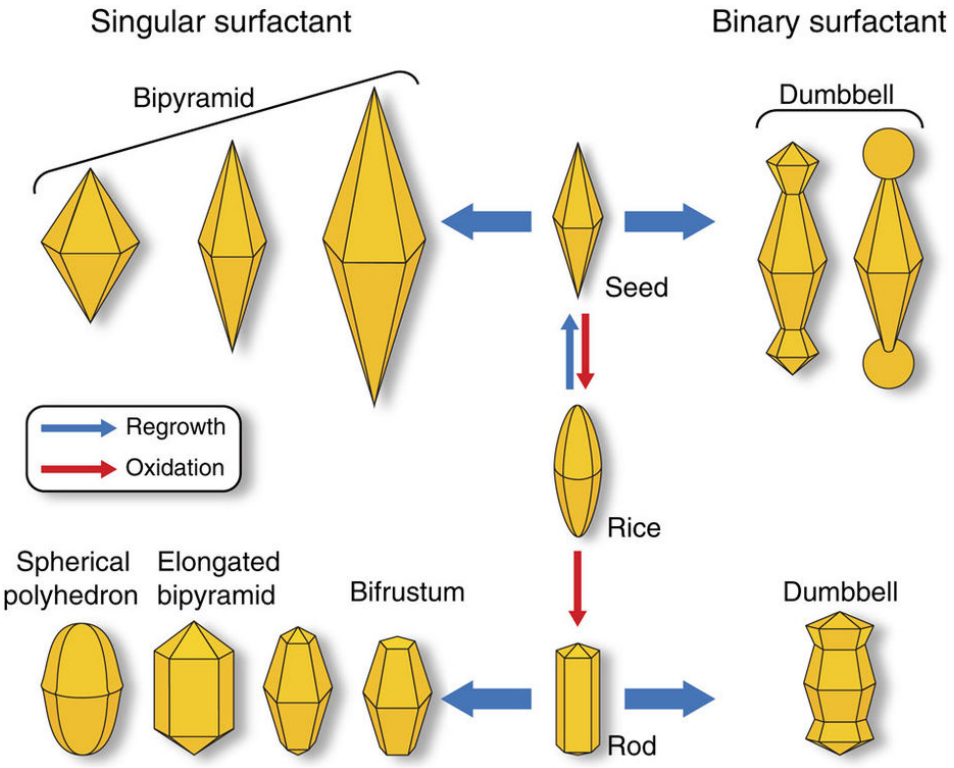

Figure 2.1 Schematic representation of the shape control of the bipyramids The various pathways to generate unique structures originating from the bipyramid are shown.

which was capable of improving the shape yield to as high as 60%[11, 12, 13]. The improvement on the yield with these larger headgroups was attributed to the slowing of the growth rate. The steric bulk of the headgroup on the surface of the nanoparticle blocked the Au^0 deposition much in the same way that Ag^+ blocks the surface of bipyramids and nanorods, explained in more detail below, through what is referred to as underpotential deposition[10]. Despite these improvements, pure gold bipyramids are unrealized through synthetic techniques alone.

Purification of some nanoparticle shapes, namely cubes and rods, had been shown possible through depletion-induced flocculation[14]. It was shown capable of removing spherical nanoparticles from the desired nanorods simply by adjusting the concentration of surfactant in solution. Demonstrated here was the first successful purification of a range of sizes of gold

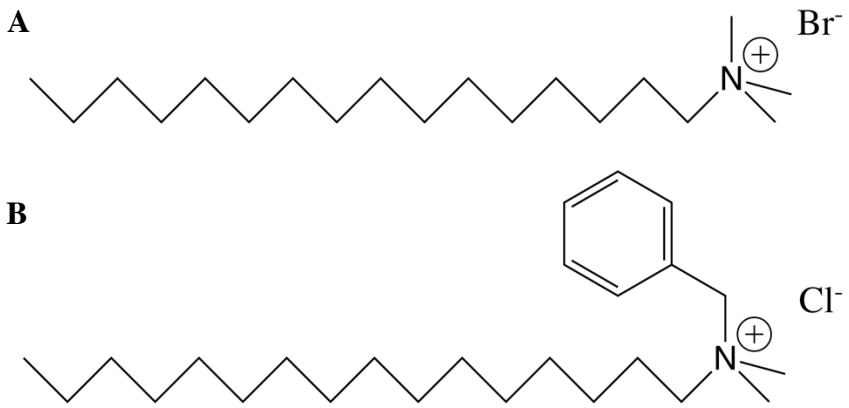

Figure 2.2 Structure of the surfactants that can be used for depletion flocculation (a) The structure of CTAB surfactant, which is used for the synthesis of gold bipyramids but cannot be used for the purification, which is explained below. **(b)** The structure of BDAC surfactant, which is used for depletion flocculation of gold bipyramids, but has little synthetic use for bipyramids.

bipyramids using the depletion flocculation method[15]. The use of benzyldimethylhexadecyl-ammonium chloride (BDAC) permits the flocculation to occur at reasonable surfactant concentrations (Figure 2.2). The purified bipyramid product can then be used as a highly monodisperse seed capable of generating a new family of nanoparticle shapes that retain this monodispersity. These new anisotropic gold nanoparticles include a variety of tip geometries as well as highly tunable size augmentations through either oxidative etching or seed-mediated growth. The conditions employed in the etching and growth processes also offer valuable insights into the growth mechanism difficult to realize with other gold nanostructures. The high-index facets and more complicated structure of the bipyramid lead to a wider variety of intriguing regrowth structures than in previously studied nanoparticles.

2.2 Results and Discussion

2.2.1 Purifying the Gold Bipyramids

To start, gold bipyramids were synthesized according to the published method by Liu and Guyot-Sionnest using seed-mediated growth[10], and subsequently purified by depletion

flocculation. BDAC was chosen for the purification due to the significantly higher micelle concentration than CTAB at the same concentrations (roughly 2.6 times more for equivalent surfactant concentration. According to the theoretical model proposed by Park[14], the high micelle concentration induces flocculation at much lower surfactant concentrations, helping to avoid certain issues that can generally arise at high surfactant concentrations such as high solution viscosity, solubility issues and the unpredictable transitions from spherical micelles to rod-like or worm-like micelles[14]. The model proposed by Park is shown and discussed below in Equation 2.1. Figure 2.4 shows representative ultraviolet–visible (UV-Vis) spectra and transmission electron microscopy (TEM) image for highly purified gold bipyramids over 90% (see also Figure 2.3 for additional TEM images of the range of sizes). The purification utilizes depletion attraction forces to selectively flocculate nanopaticles with high facial surface area, in this case the bipyramids. The strength of the attractive force is proportional to the volume of pure water generated during the approach of the two nanoparticles, which is likewise proportional to the possible contact area of the nanoparticles. Therefore, particles with large possible contact areas, such as the bipyramids, will selectively flocculate, while those with low possible contact areas, such as the spherical impurities, will remain in the supernatant (from Figure 2.4a, 1: as-synthesized bipyramids, 2: supernatant, 3: purified bipyramids). Bipyramids over 100nm become increasingly difficult to separate from pseudo-spherical impurities as the facial surface area of both bipyramids and pseudo-spherical impurities are increased, resulting in undesirable co-flocculation (Figure 2.3c).

Depletion flocculation as a concept was first proposed by Asakura and Oosawa in 1958, and applied as a purification technique for nanoparticles by Park in 2010. The first nanoparticle systems to be purified involved nanorods and nanospheres. Park introduced a model to predict when nanoparticles would begin to flocculate. The simplified equation, shown below in Equation

1, relates the effective micelle concentration and contact area of the nanoparticle to the potential, U. When $|U| \approx 4\text{-}5k_BT$, the particles will begin to flocculate out of solution.

$$|U| = \frac{(2r_m)A(c - cmc)}{n} N_0 k_B T \qquad \text{(Eq. 2.1)}$$

In Equation 2.1 above, r_m is the radius of the surfactant micelle, A is the possible contact area of the nanoparticle, c is the surfactant concentration, cmc is the surfactant's critical micelle concentration, n is the aggregation number of the surfacant micelle, N_0 is Avogadro's number, k_B is the Boltzmann constant, and T is the temperature. For the purpose of calculating the contact area of the bipyramid, the shape was assumed to be a pentagonal bipyramid with 10 equivalent triangular faces. Although the actual three-dimensional shape is up for debate, the application to the surface area calculation and ultimately the depletion force is largely unchanged. The constants for the surfactant micelles were all obtained from literature sources.

The reason BDAC was chosen for the depletion flocculation was its higher effective micelle concentration than CTAB. For BDAC, r_m=2.4 nm[16], cmc=0.0005 M[17], n=62[18] and for CTAB, r_m=3.0 nm[19], cmc=0.001 M[20], n=162[21]. This results in an effective micelle concentration roughly 2.6 times larger, and a potential to flocculate roughly 2.09 times higher (due to the smaller micelle size). The high micelle concentration is necessary because bipyramids, having ten identical faces, actually have a relatively low contact area compared to nanorods of similar size, which essentially have five faces.

The range of purified bipyramids only extends from 68 nm to 95 nm while the range of bipyramids available through the seed-mediated growth extends to sizes both shorter and longer than that. Shorter bipyramids are difficult to purify because the corresponding BDAC

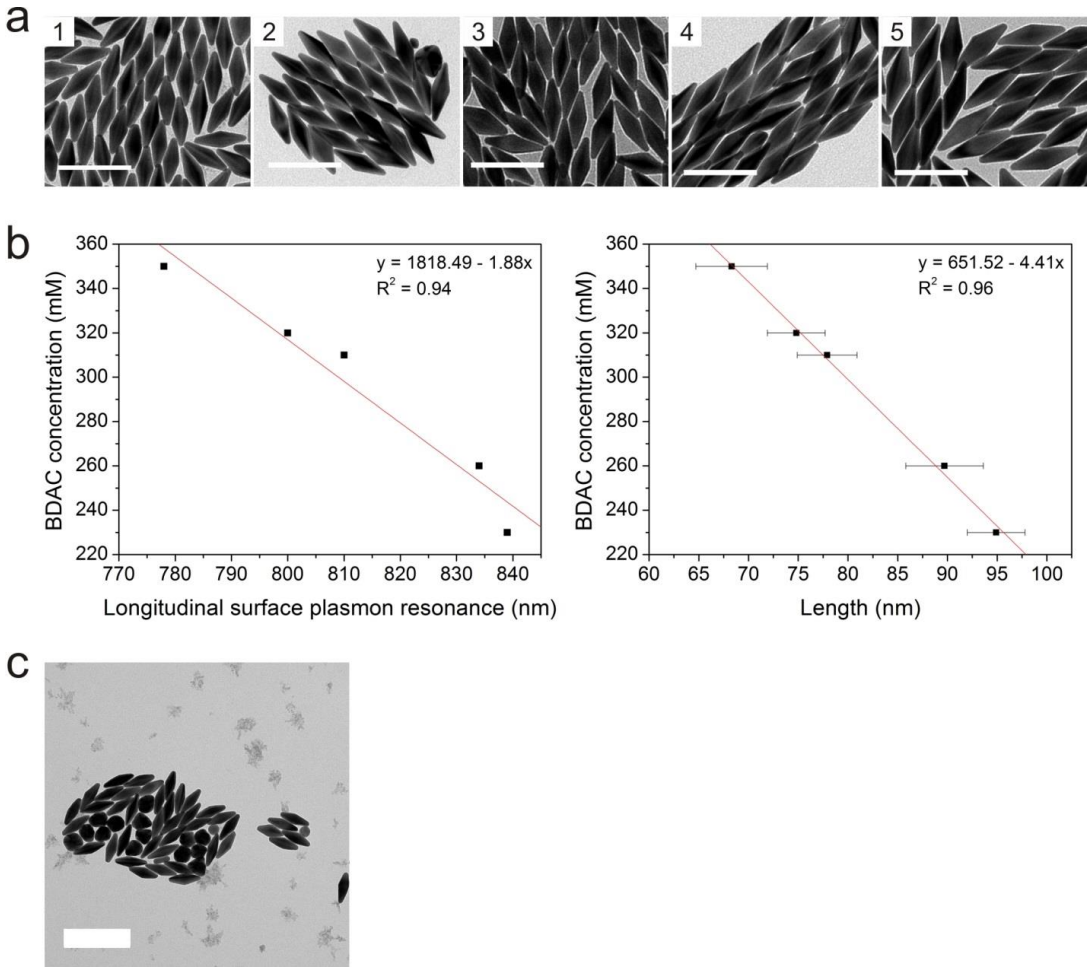

Figure 2.3 Purification of bipyramids **(a)** TEM images of purified bipyramids (1-5 corresponding to 110, 100, 95, 70 and 60 μL of seed solutions). Scale bars are 100 nm. **(b)** BDAC concentrations necessary for purification as a function of longitudinal surface plasmon resonance (LSPR) and length of bipyramid are shown. **(c)** Co-flocculation of both bipyramids and pseudo-spherical impurities when the purification is attempted with bipyramids synthesized >100 nm. Scale bar is 200 nm.

concentration necessary to purify is around 400 mM or more. At concentrations this high, the viscosity is too high to allow for the flocculation to occur in a reasonable time frame. For bipyramids synthesized larger than 95 nm, the psuedo-spherical impurities are also proportionally larger. As these impurities grow larger, they become less spherical and more faceted. These facets become large enough that they begin to co-flocculate with the bipyramids, effectively preventing any possible purification based on shape selectivity (Figure 2.3c).

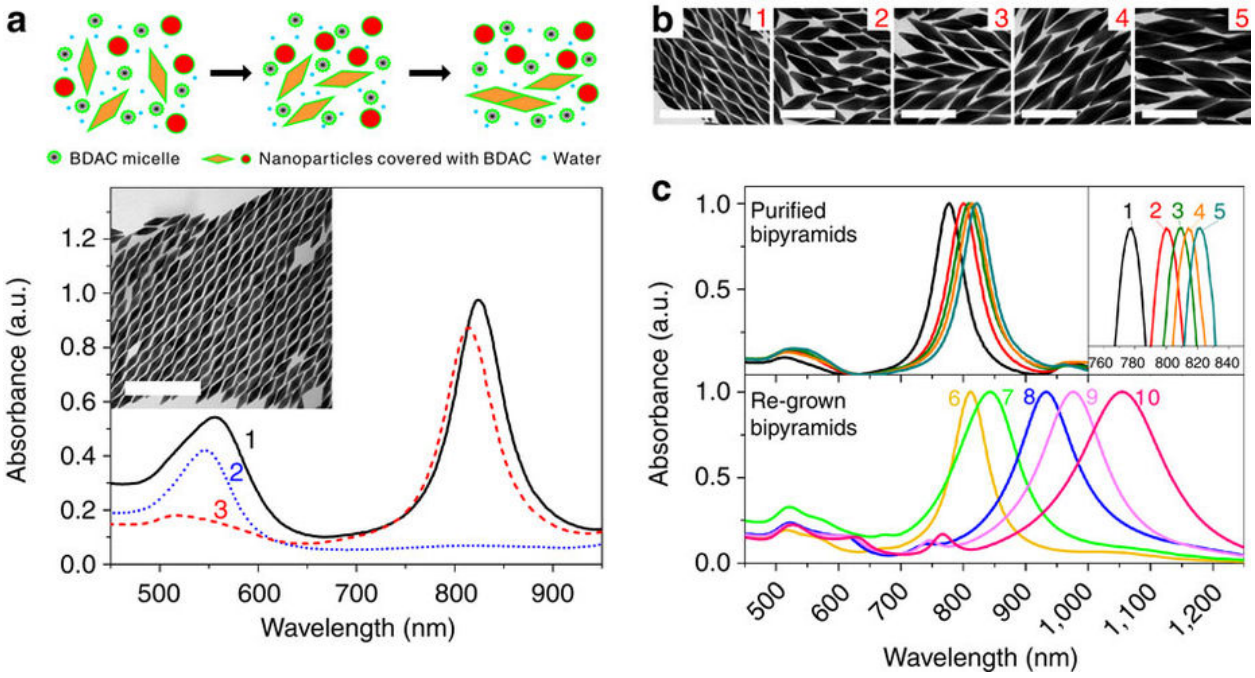

Figure 2.4 Various sizes of bipyramids generated from the purification and regrowth (a) Schematic illustration, ultraviolet–vis-near-infrared spectrum and TEM image of bipyramids resultant from the purification by depletion flocculation with BDAC. **(b)** The various sizes of bipyramids are regrown from the original bipyramid seed in a. Bipyramids shown in b (1–5) correspond to spectra 6–10 in c. **(c)** The normalized extinction spectra of purified (1–5) and regrown bipyramids (6–10) are shown. The inset shows an enlarged spectrum of the LSPR for the purified bipyramids. Full width at half maximum of LSPR peaks were measured as 58, 60, 63, 60, 59, 73, 113, 121, 126 and 154 nm or 21.4, 20.7, 19.7, 20.7, 21.0, 17.0, 11.0, 10.3, 9.8 and 8.1 eV for 1–10, respectively.

2.2.2 Synthesis of Bipyramid-Related Structures

On obtaining pure, monodisperse gold bipyramids, a variety of other gold nanostructures with novel shapes or changes in size were synthesized from the bipyramids in a process that can be described as seed-mediated growth. Because the 'seed' used in this case is monodisperse, the product obtained through these transformations is also monodisperse in both shape and size, with the polydispersities ranging from only 2 to 5%. Using the purified bipyramid as a seed, the limitations to size of both the synthesis and separation can be overcome, allowing an increase in particle size by over 100 nm with high purity. TEM images in Figure 2.4b and UV–Vis

No.	Length (nm)	Width (nm)	AR	LSPR (nm)
1	68.3 ± 3.6	22.8 ± 1.2	3.0	778
2	74.8 ± 2.9	22.7 ± 1.5	3.3	800
3	77.9 ± 3.0	24.5 ± 1.5	3.2	810
4	80.4 ± 2.8	23.6 ± 1.2	3.4	814
5	94.9 ± 2.9	30.8 ± 1.6	3.1	822
6	113.1 ± 3.9	34.7 ± 1.4	3.3	811
7	141.0 ± 4.8	47.9 ± 1.4	3.0	844
8	172.3 ± 4.3	51.8 ± 2.2	3.3	933
9	202.7 ± 3.2	56.7 ± 2.0	3.6	975
10	239.7 ± 5.0	64.5 ± 3.6	3.7	1054

Table 2.1 Measurements of purified and regrown bipyramids. The table shows the summary of the lengths and widths, aspect ratios (AR), and longitudinal surface plasmon resonance (LSPR) peaks, corresponding to extinction spectra 1-10 in Figure 2.4c.

spectra 6–10 in Figure 2.4c show the range of sizes of the regrown bipyramids obtained by adding either a different amount of bipyramid seeds or adjusting the concentration of reactants in growth solution (see Tables 2.1 and 2.3 for detailed size measurements and synthetic conditions). The full width at half maximum of the longitudinal surface plasmon resonance (LSPR) peak is between 58 and 153nm and these values, which compare favorably to that of nanorods (between 100– 200 nm or 6.2–12.4 eV for similar sizes)[22, 23], also confirm the monodispersity of the bipyramids. It has also been observed that the aspect ratio can be altered slightly during the regrowth by either changing the pH or the amount of $AgNO_3$ in the growth solution (Figure 2.5b).

2.2.3 Synthesis of Bipyramid dumbbells

In addition to enlarging the bipyramids, regrowth of bipyramids by changing the synthetic conditions introduces several new structures to be added to the toolbox of gold nanoparticles, but also offers powerful insights into the growth mechanism yet unrealized with nanostructures of simpler shape. Regrowth of gold nanospheres and gold nanorods is well studied, and the

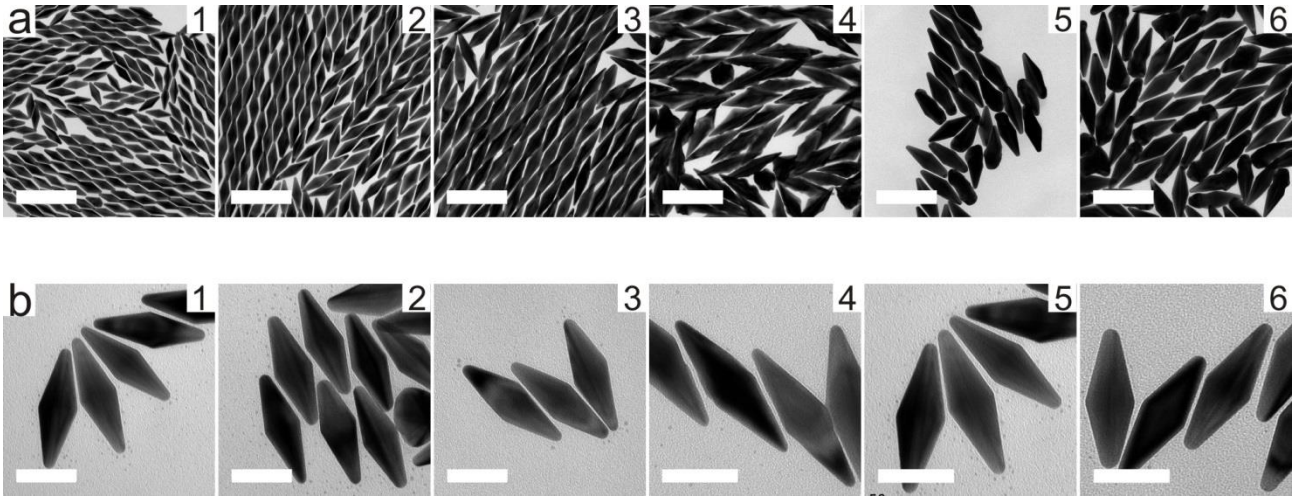

Figure 2.5 Regrown bipyramids with varying H+, Ag+ and seed concentrations (a) TEM images of enlarged bipyramids resulting from regrowth with different concentration of reactants using 100 μL seeds (1-4) and 5 μL seeds (5-6). **(b)** TEM images of regrown-bipyramids with different amount of AgNO3 (1-3) and HCl (4-6). See also Table 2.3 for detailed synthetic conditions. It is worth noting that a high concentration of gold precursor (>10 mM) in the growth solution containing 0.1M CTAB can cause the formation of CTAB-Au complex (orange color) that can affect the crystalline structure of the bypiramids, resulting in a rough surface (1-4 in panel a). Additionally, a volume of seed solution too small can cause erratic growth and yield undesired shape impurities (5-6 in panel a). All scale bars in a and b are 200 nm and 50 nm, respectively.

transformation of nanorods to dumbbells has revealed much about the intricacies of nanoparticle growth conditions. However, both the nanosphere and nanorod fail to offer the complex crystal facets and twinned shape that the bipyramid provides. We first compared the regrowth of bipyramids using different surfactants (CTAB, cetyltrimethylammonium chloride (CTAC) and BDAC) as well as their mixtures. For standard growth solution with individual surfactants, size augmentation was dominant over any structural changes. Size augmentation of bipyramids with CTAB provided the best shape uniformity and surface smoothness, compared with both BDAC and CTAC (Figure 2.6a, condition 1, and Figure 2.7). These results can be explained by considering the different binding affinities of CTAB and BDAC, that is, $Br^- > Cl^-$, and also the degree of underpotential deposition in the presence of Ag^+ ions onto the gold surface[10, 24, 25, 26]. The

regrowth with CTAC resulted in random shape growth and aggregation because centrifugation with CTAC to remove remaining CTAB reduces particle stability, which is consistent with reported result for nanorod growth using CTAC (Figure 2.7)[27, 28]. According to reports of nanorod growth using cationic headgroup with bromide anion as a counterpart, larger headgroups lead to nanorods of higher aspect ratio and slowed growth rate, implying a higher binding affinity and resulting in a more stable bilayer on the particle surface[11, 12, 13, 24]. The results from our observation and literature suggest that the affinity of surfactants in the presence of Ag^+ ions could be extended to CTAB > BDAC > CTAC.

Systematic studies were conducted with the three possible binary surfactant combinations, that is, CTAB/CTAC, CTAB/BDAC and BDAC/CTAC (Figure 2.7). Despite changing the molar ratios, overgrowth at the tips was not observed and only somewhat observed for BDAC/CTAB or CTAC/BDAC, respectively (Figure 2.7a). Intriguingly, the molar ratio of surfactants in binary systems showed a huge influence on the regrowth of bipyramids, especially at the tip region. Previously, mixed surfactants as capping agents have been used for adjusting the aspect ratio of gold nanorods[13, 24], Ag-tipped overgrowth of gold nanorods[29], and tetrahedral-like gold nanotripods[30]. However, the role of each component for the growth is still ambiguous due to the complexity of interactions. As mentioned previously, the binding affinity of CTAB is greater than that of CTAC. However, as the ratio of CTAC:CTAB is increased to between 90:1 and 900:1, an equilibrium exists where CTAC occupies some of the surface area. Evidently, the CTAC is localized to the tip region where the binding preference of CTAB over CTAC is minimal. In this case, growth at the less protected ends capped by CTAC results in the observed tip overgrowth utilizing the shape-directing properties of the halide (Figure 2.6b, condition 6)[24, 25, 26, 29]. When the ratio is either too high or too low or when pure CTAB is used, the tip growth is not observed as

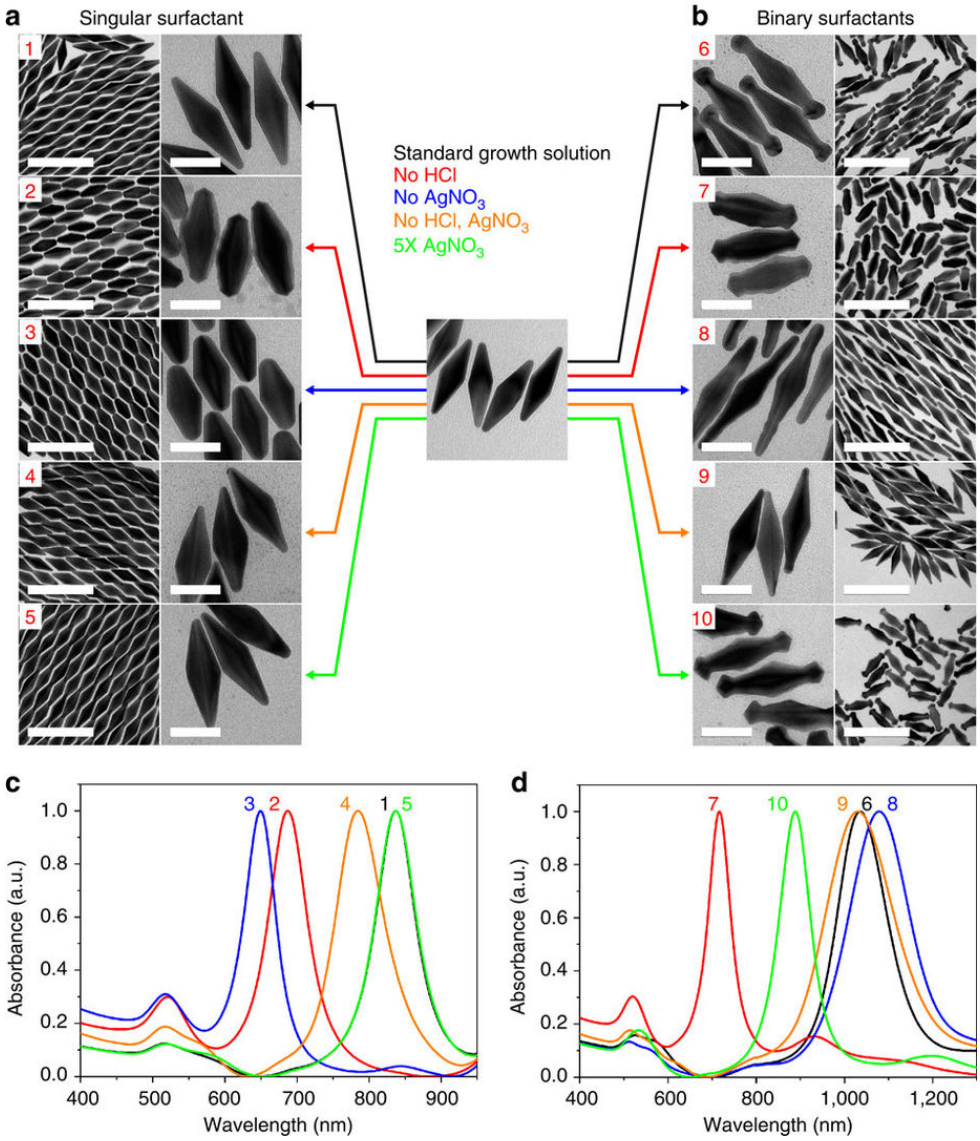

Figure 2.6 Shape-controlled bipyramids regrown with either singular and binary surfactants are shown (a,b) TEM images of the monodisperse, regrown structures from purified bipyramid seeds with singular surfactant (conditions 1–5) and binary surfactants (conditions 6–10). The colored arrows indicate the specific conditions for regrowth (see also Table 2.3 for detailed conditions). Scale bars, 200 nm (low magnification); 50 nm (high magnification). **(c,d)** Normalized ultraviolet–vis–near-infrared spectra of regrown structures with singular surfactant (1–5 in c correspond to 1–5 in a) and binary surfactants (6–10 in d correspond to 6–10 in b), respectively. See Table 2.1 for detailed size measurements.

size augmentation becomes the dominant growth mode as the surface is covered uniformly in a single surfactant (Figure 2.6a, condition 1, and Figure 2.7). This experimental observation is

qualitatively consistent with reported results for adjusting aspect ratio of gold nanorod and Ag-tipped overgrowth of gold nanorods using a BDAC/CTAB mixed surfactant system[24, 29].

Fig. No.	Length (nm)	STDEV*	PD* (%)	Width (nm)	STDEV*	PD* (%)	AR*	Tip Width (nm)	STDEV*	PD* (%)
2.6a1	99.5	2.6	2.6	30.2	0.9	3.0	3.3			
2.6a2	86.4	2.5	2.9	35.9	1.1	3.0	2.4			
2.6a3	74.5	2.6	3.6	32.5	0.8	2.6	2.3			
2.6a4	99.8	4.4	4.4	34.7	1.1	3.1	2.9			
2.6a5	107.6	3.3	3.1	33.4	1.3	3.8	3.2			
2.6b6	115.5	5.9	5.1	30.0	1.5	5.1	3.8	17.3	2.6	15.2
2.6b7	84.3	3.5	4.1	30.4	1.6	5.1	2.8	22.3	1.5	6.5
2.6b8	137.7	7.6	5.5	28.5	1.1	4.0	4.8	11.9	0.9	7.6
2.6b9	100.8	3.7	3.7	27.1	1.1	4.2	3.7			
2.6b10	97.7	4.9	4.0	31.1	1.7	5.3	3.1	22.5	1.4	6.4
2.12a2	58.3	3.2	3.8	23.4	1.2	5.2	2.5			
2.12a3	46.3	2.1	3.6	22.8	1.0	4.3	2.0			
2.14a1	76.2	2.5	3.4	33.9	1.1	3.2	2.2			
2.14a2	52.3	2.4	3.2	39.4	1.9	4.8	1.3			
2.14a3	52.5	1.9	3.0	39.3	1.0	2.5	1.3			
2.14a4	60.5	3.3	2.8	38.7	1.6	4.2	1.6			
2.14a5	82.3	2.7	2.5	33.9	0.9	2.6	2.4			
2.14b	65.7	2.3	2.3	35.7	2.7	7.5	1.8	34.4	2.4	7.0

Table 2.2 Dimensions of regrown structures, both bipyramids and oxidatively-etched nanorods, with singular and binary surfactants. *STDEV= standard deviation, PD= polydispersity, AR= aspect ratio.

By carefully modifying the reaction conditions, we were also able to control the tip shape of dumbbell-like bipyramids to further confirm the role of components in the growth solution. Figure 2.6 shows TEM images and UV-Vis-NIR spectra of a variety of monodisperse regrown structures from bipyramids with singular or binary surfactants. We observed marked changes at

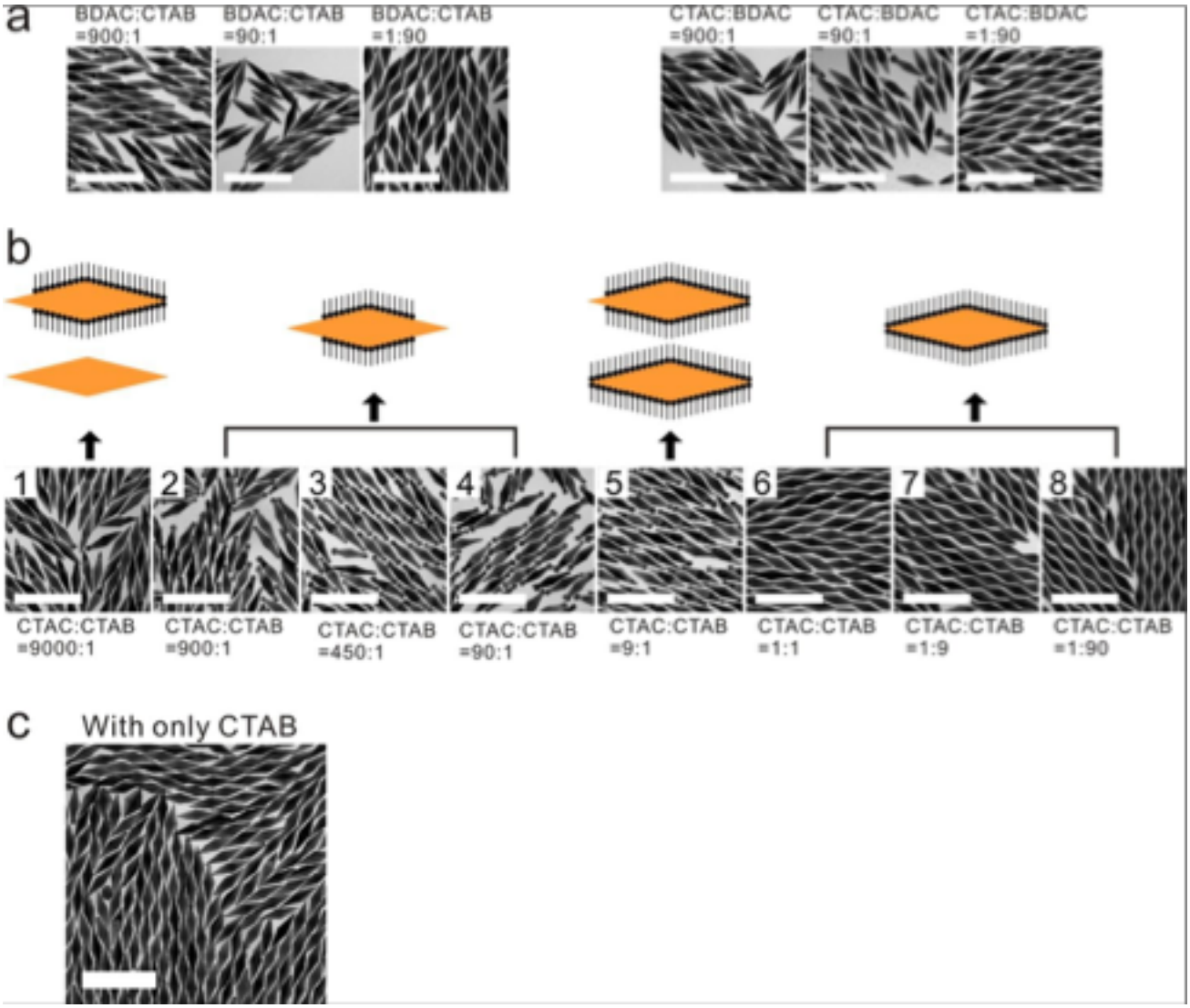

Figure 2.7 Systematic studies of the three possible binary surfactant combinations and ratios The growth solution consists of 2 mM HAuCl4, 2 mM AgNO3, 1 M HCl and 20 mM ascorbic acid for all syntheses shown in this figure. **(a)** TEM images of the regrown bipyramids with BDAC/CTAB and CTAC/BDAC binary surfactant conditions. **(b)** TEM images of the regrown bipyramids with CTAC/CTAB binary surfactant condition and illustrative schematic propsing the binding of the surfactant to the bipyramid surface. The black surfactant represents the CTAB while the exposed area is representative of the surface area binded by CTAC, which is likely responsible for the specific growth at the tips due to its weaker binding. **(c)** TEM image of the regrown bipyramids using an identical amount of CTAB in b-4 without CTAC or BDAC, only a minimal amount of tip overgrowth was observed. All scale bars are 200 nm.

the bipyramid tips including spherical-, rod- and bipyramid-like tips with binary surfactants. The standard growth solution of bipyramids in these experiments consisted of 91.9 mM of $HAuCl_4$,

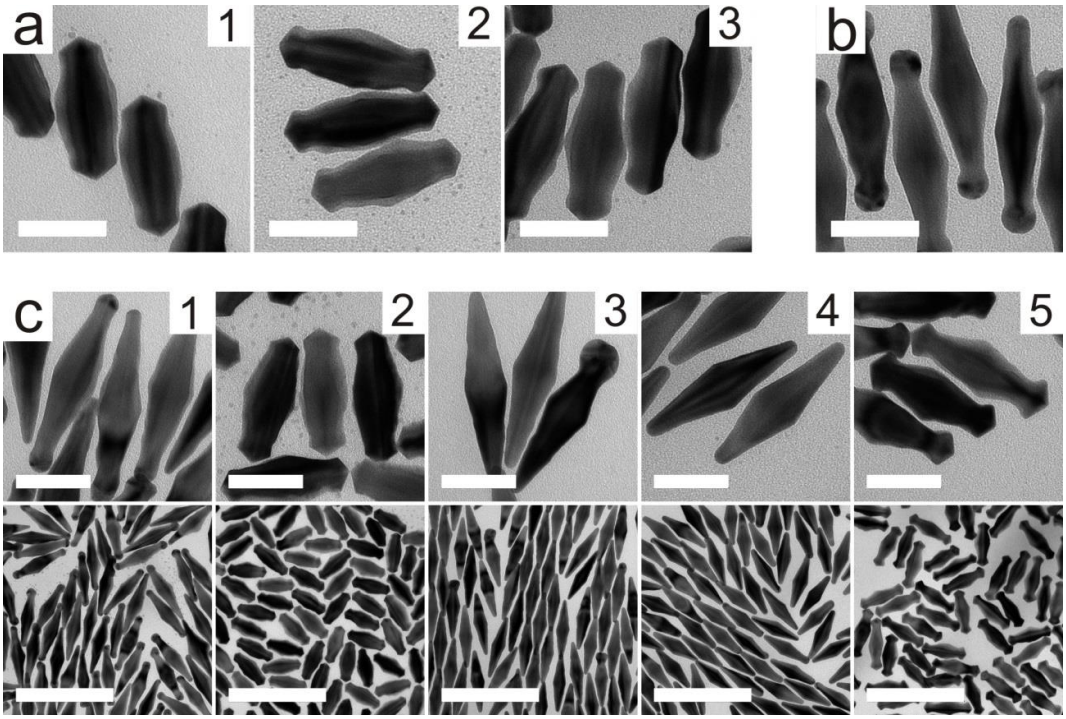

Figure 2.8 Regrown bipyramids with binary surfactants (a) TEM images of regrown structures in Figure 2.6b-7 with different amounts of AgNO3 and with no added HCl. The regrowth solution consists of 2 mM HAuCl4 (50 μL), 20 μL of nanopure water in place of 1 M HCl (20 μL) and 10 mM ascorbic acid (8 μL) with varying concentrations of AgNO3; 10 μL of 1 mM, 2 mM and 4 mM corresponding to images 1 through 3 above, with binary surfactant [CTAC]:[CTAB] = 90:1. **(b)** TEM image of regrown structures in Figure 2.6b-6 with more HCl used. The regrowth conditions are identical to those used in Figure 2.6b-6, except 30 μL of 1 M HCl was used. **(c)** TEM images of regrown structures with binary surfactants [CTAC]:[CTAB] = 900:1. The regrowth conditions are identical to those used in Figure 2.6: specifically, 1 is standard growth solution, 2 has no HCl, 3 has no AgNO3, 4 has no HCl and no AgNO3, and 5 has 5x AgNO3. All scale bars are 200 nm and 50 nm for low and high magnification images, respectively.

18.4 mM of $AgNO_3$, 0.0184 N of HCl and 147 mM of L-ascorbic acid. The molar ratio of [ascorbic acid] / [$HAuCl_4$] was 1.6 in Figure 2.6 to ensure complete reduction of Au^{3+} to Au^0.[29] If less ascorbic acid is used, remaining Au^{3+} acts as an oxidant, and an etching process becomes dominant, resulting in shortened bipyramids (Figure 2.9)[31]. The major factors for the shape changes in these reactions were HCl and $AgNO_3$. It is reported that the reduction rate of Au^{3+} can be increased by increasing the pH of the solution, which can cause fast deposition along the existing crystal face, leading to growth of the nanorod in all directions having shorter aspect ratio[32, 33]. The pH of the

growth solution is 1.74 for the case of standard growth solution and 3.62 for the growth solution without HCl. Under both of these conditions, reduction of Ag^+ can be neglected due to the increased redox potential of ascorbic acid[34]. It is now established that a monolayer of silver can be deposited onto a particular surface of gold during the growth through underpotential deposition, thus stabilizing the surface and slowing the growth rate[10, 25, 26, 35]. The growth rate of all facets in the structure can be altered depending on the degree of surface coverage by underpotential deposition of silver ions, and therefore differing growth rates of particular facets will determine the final structure of the nanoparticle.

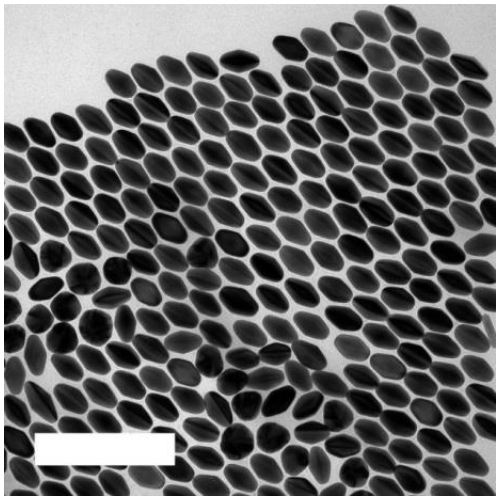

Figure 2.9 TEM image of oxidatively etched bipyramids using Au3+ remaining from the growth solution The regrowth solution consists of 2 mM HAuCl4 (50 μL), 2 mM AgNO3 (10 μL), 1 M HCl (20 μL) and 10 mM ascorbic acid (8 μL) with 0.9 mL of 0.1 M CTAB. Note that the molar ratio of [ascorbic acid]/[HAuCl4] in this case is 0.8 compared with 1.6 in standard growth solution. Scale bar, 250 nm.

The results in Figure 2.6a, condition 2, and Figure 2.6b, condition 7, show predominant growth along the short axis with sharp apices. As compared with growth in standard growth solution, a faster growth rate is expected in all directions for bipyramids without HCl at pH 3.62. However, the growth rate at the tip is greatly inhibited, because of the presence of Ag^+ ions, which

can more easily access the tip region, resulting in underpotential deposition. The high curvature of the tip region results in lower surfactant packing density than on the bipyramid faces, allowing additional room for Ag^+ to deposit in the intersurfactant regions[29]. This results in a stepped facet formed along the long axis of the bipyramids, thereby sharpening the bipyramid tip for both[10]. The growth for binary surfactants showed increased overgrowth at the tip than for singular case because it has less coverage of CTAB layer accelerating the growth along the tip region. For binary surfactants, adding more or less $AgNO_3$ without HCl resulted in little elongation and unrestricted growth of the width, especially at the tips, indicating that increased inhibition of growth along the long axis can greatly alter the shape of particle (Figure 2.8a). Likewise, in the experiments without $AgNO_3$ at pH 1.76, fast growth is expected due to the absence of Ag ions, however, slower than the case without both HCl and $AgNO_3$ due to the effect of the pH on the reducing reduction power of ascorbic acid. The reaction proceeds with a rate that allows for controlled growth due to the low pH, but the absence of Ag^+ ions, normally yielding a stepped crystal facet at this pH for bipyramids, results in facilitated growth of a nanorod-like structure[10, 25, 26]. Without Ag^+ ions to block certain growth facets, bipyramids grown in a singular CTAB surfactant system were synthesized with low aspect ratio (~2.3) and poorly defined tips; due to the even coverage of the singular surfactant and lack of Ag underpotential deposition, growth occurred evenly in all directions (Figure 2.6a, condition 3). Interestingly, rod-like tips were formed in the binary surfactant system (Figure 2.6b, condition 8). Similar to the above case, it is believed that overgrowth at the tip region was induced from the reduced surface coverage of CTAB in the binary system. In the absence of Ag^+, the overgrowth was accelerated and bypassed the stepped structure to form the rod-like structures at the tips.

Figure 2.6a, condition 4, and Figure 2.6b, condition 9, show the regrowth of bipyramids

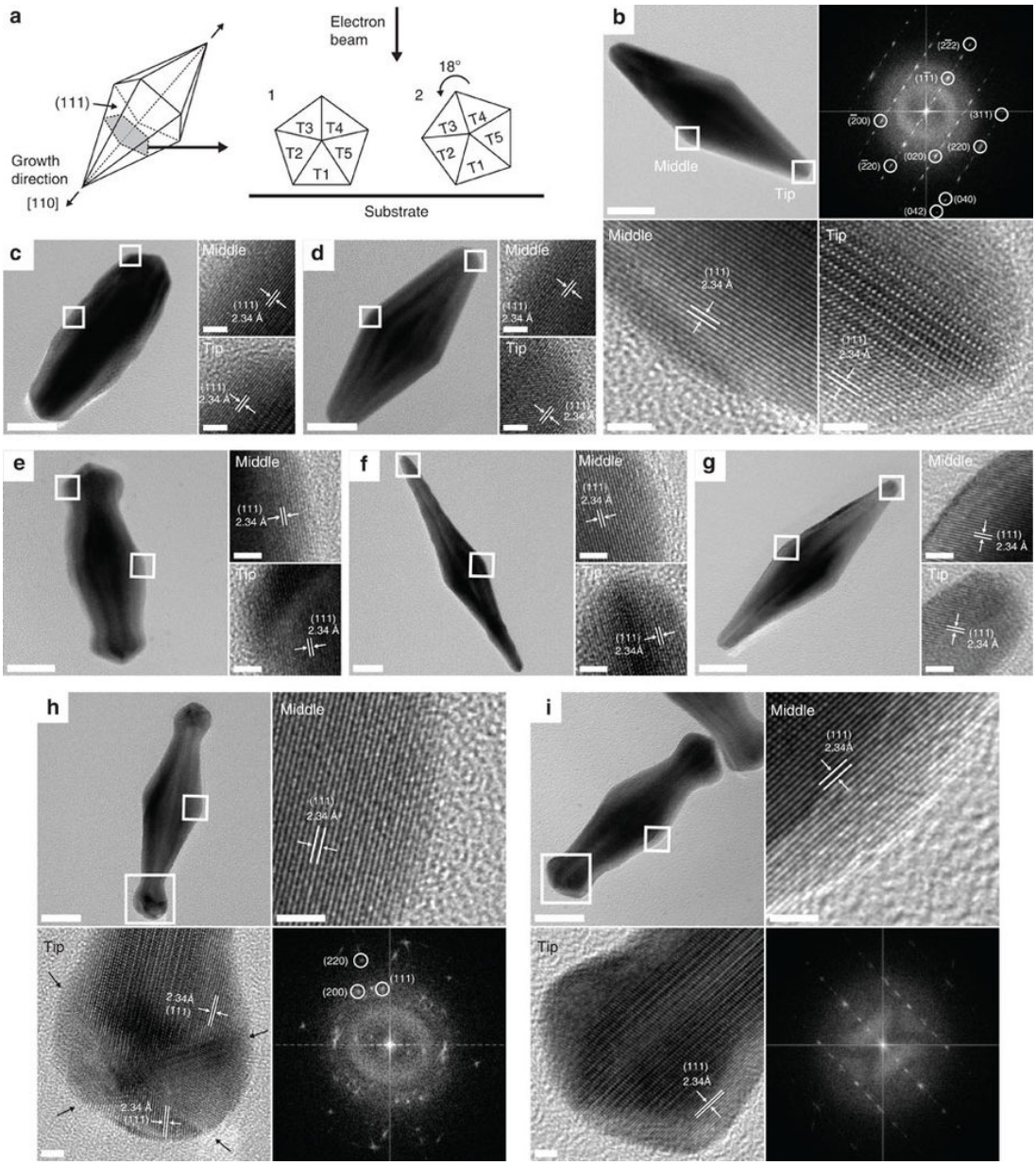

Figure 2.10 HR-TEM images and FFT patterns of regrown bipyramids with singular and binary surfactants (a) Schematic illustrations for cyclic penta-tetrahedral twinning of bipyramids. The grey area shows the cross-section of the bipyramid perpendicular to the growth direction. Each twinning plane is labelled from T1 to T5. Schematic on the right of the panel shows most of the possible orientations of bipyramids on the substrate with respect to the beam direction. Regrown bipyramids in Figure 2.6a—conditions 1–3 for b–d, respectively; Figure 2.6b—conditions 7–9 for e–g, respectively; Figure 2.6b—conditions 6 and 10 for h and i, respectively. Magnified images showing the lattice fringes represent the areas marked with white boxes at the tip and middle of particles. The black arrows in h indicate the twin planes of the spherical tips in the dumbbell-shaped structures. Scale bars, 20 nm (low-magnification images); 2 nm (high-magnification images).

without both HCl and $AgNO_3$. In this case, a much faster growth rate is expected than the former two cases, either without HCl or without $AgNO_3$. Due to a greatly faster deposition and the absence of Ag inhibition, rapid addition of Au^0 atoms occurs on the stepped surface of bipyramids evenly in all directions. This results in particle maintaining its original bipyramid shape for both the singular and binary surfactant systems. The aspect ratio for binary surfactants was slightly higher than the singular case because of the lessened CTAB coverage as mentioned above, resulting in a small preference for growth at the tip and a slightly elongated particle.

Meanwhile, additional $AgNO_3$ (5x more than standard growth conditions) shows significant morphological changes at the tip region in binary surfactants, given less coverage of CTAB at the tip than the singular surfactant. Distinct crystalline structures identical to bipyramids were formed at the tips at both ends (Figure 2.6b, condition 10). However, negligible changes were observed from singular CTAB surfactant (Figure 2.6a, condition 5). These results indicate that insufficient protection from CTAC surfactant can be more sensitive for inhibition of growth from underpotential deposition of Ag^+, allowing for easier access to the tip end, resulting in significant shape changes. The addition of more acid in this case results in negligible changes for both singular and binary surfactants (Figures 2.5 and 2.8). The UV-Vis-NIR spectra in Figure 2.6c,d reflects the various structural changes of regrown bipyramids dependent on the growth conditions. Because most of regrown structures show changes in length, significant peak shift of longitudinal plasmon peaks with narrow widths were observed.

The crystalline structure of individual regrown bipyramids with singular and binary surfactants was determined by high- resolution TEM (HR-TEM) and fast Fourier transform (FFT) patterns (Figure 2.10). Figure 2.10b shows HR-TEM images and the corresponding FFT patterns of enlarged bipyramids resulting from the regrowth with a singular surfactant and standard growth

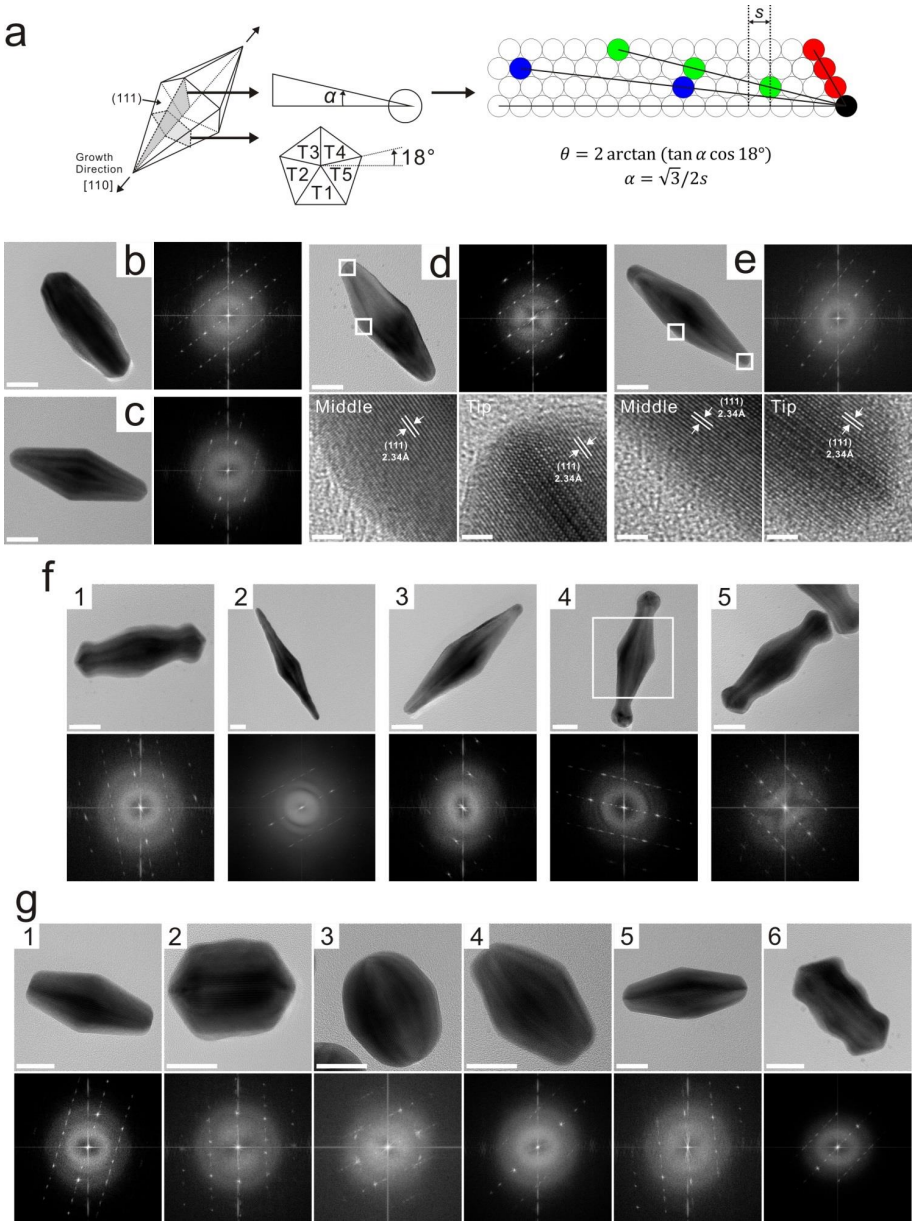

Figure 2.11 HR-TEM images and FFT patterns of regrown structures with singular and binary surfactants (a) Illustrations for cyclic penta-tetrahedral twinning of bipyramids. Each twinning plane is labelled from T1 to T5. The two gray areas show the cross-section of the bipyramid perpendicular to the growth dirction and inter-plane between T4 and T5. The equation shows the relationship between measured tip angle (θ) of the structures in orientation 1 in Figure 2.10a and average step length (s). Regrown bipyramids in Figures 2.10c **(b)**, 2.10d **(c),** 2.6a-4 **(d),** 2.6a-5 **(e),** 2.10e **(f-1),** 2.10f **(f-2),** 2.10g **(f-3),** 2.10h **(f-4**, FFT shows boxed area), 2.10i **(f-5),** 2.14a-1 **(g-1),** 2.14a-2 **(g-2)**, 2.14a-3 **(g-3),** 2.14a-4 **(g-4),** 2.14a-5 **(g-5)** and 2.14b **(g-6)**, respectively. Magnified images showing the lattice fringes represent the areas of marked white boxes at the tip and middle of particles. All scale bars are 20 nm and 2 nm for low and high magnification images, respectively.

solution. The magnified images in Figure 2.10b show clear lattice fringes at the tips and middle of the particles. It shows that both fringes are parallel to the growth axis and twinned along the long axis. The spacing between lattice fringes is confirmed as 0.234 nm by direct measurement, corresponding to the (111) facets of the bipyramids. The FFT pattern in Figure 2.10b shows a diffraction pattern of the bipyramid corresponding to orientation 1 in Figure 2.10a. The indexed reflections in the FFT pattern correspond to the lattice parameters: d_{111} = 0.234 nm, d_{220} = 0.143 nm, d_{222} = 0.118 nm, d_{200} and d_{020} = 0.204 nm, d_{311} = 0.122 nm, d_{400} = 0.102 nm, and d_{420} = 0.091 nm. Reflections indexed as $(1\bar{1}1)$, (311), and (220) are scattered from T3 and T4. Reflections indexed as $(\bar{2}00)$, (020) and (220) are from T1. The remaining reflections that are not indexed are induced by multiple scattering effect. All measured values are within an error range of ±2% compared with bulk data and agree well with reported results, indicating that regrown bipyramids are penta-twinned with face-centered cubic structure[36, 37, 38, 39]. All of the regrown bipyramids with either singular or binary surfactants are confirmed to have the same FFT pattern as a bipyramid in Figure 2.10b (Figure 2.11). The tip angles (y) of bipyramids in Figure 2.10b were measured to be 27.02 ± 1.35°, which correspond to (117) high-index facets having an average step length of ~3.5 atoms (Figure 2.11a)[10]. However, the identity of this high-index facet varies as the tip angles differ from that of bipyramids[10, 40, 41, 42]. If the tip angle is smaller than bipyramids in Figure 2.10b, the average step length can be >3.5, which can be indexed as {11*l*}, where *l*>7. Likewise, when the tip angle is larger than that of bipyramids, the average step length can be <3.5, which can be indexed as {11*l*}, where *l*<7. Interestingly, HR-TEM images and FFT of the dumbbell-like bipyramid in Figure 2.10h show multiply twinned spherical structures at both tips. (The black arrows in Figure 2.10h indicate the twin planes of the spherical tips.) The circular reflections in Figure 2.10h correspond to the lattice parameters: d_{111} = 0.229 nm, d_{220} = 0.143 nm and d_{200} = 0.203

nm, respectively. This circular type of FFT pattern resembles spherical particles having pentagonal symmetry, also known as decahedra[36, 37, 39, 43].

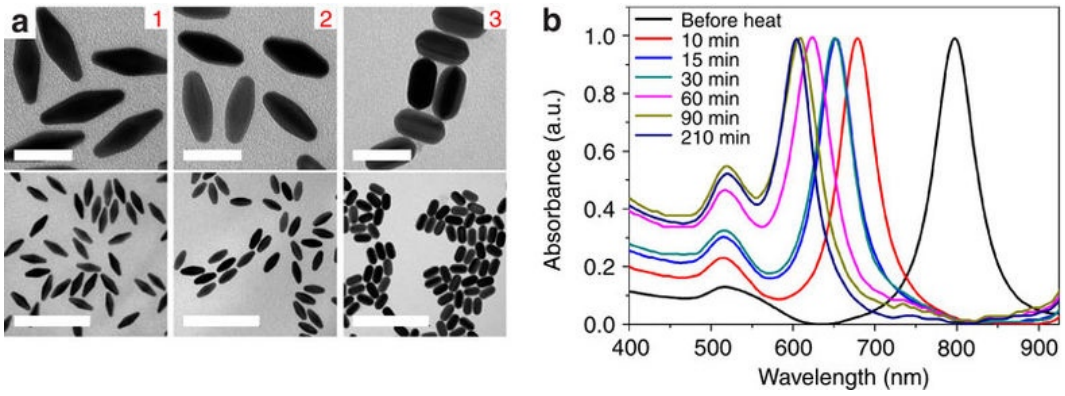

Figure 2.12 Etched structures from oxidative etching with BDAC surfactant and heating at 120 °C (a) TEM images of the etched structures resulting from heating for 10, 30 and 90 min, shown from 1 to 3. Scale bars, 50 nm (high magnification); 200 nm (low magnification). **(b)** Normalized ultraviolet–vis–near- infrared spectra of etched structures resultant of increasing the heating time.

2.2.4 Oxidative etching of bipyramids

Gold bipyramids can also undergo oxidative etching utilizing molecular oxygen dissolved in solution. Cycling oxidations and reductions of gold atoms can slowly shape the nanoparticle through a time-dependent aging process[44]. Additive oxidants such as hydrogen peroxide have been shown to accelerate the etching process and to reshape nanoparticles through atomic substraction and addition, but result in nanoparticles with poor shape and size dispersity[11, 45]. Taking advantage of the purity of the gold bipyramids and their inherent monodispersity, this etching process has been adapted to create other monodisperse structures. Because of the high-energy nature of the bipyramid facets and sharp tips, these highly reactive particles are susceptible to oxygen as an etchant despite it being a weak oxidant. As seen in Figure 2.12a, bipyramids begin to etch at the tips and are continuously sculpted to rice shaped and eventually rod shaped as the reaction progresses at 120 °C and in the presence of 0.1 M BDAC. UV-Vis-NIR spectra in Figure 2.12b

show continuous changes that are consistent with the structural changes as seen in the TEM images. In the presence of BDAC as a protective agent and etchant, the purified gold bipyramids facilitate a four-electron oxidation of four Au^0 atoms to Au^+, forming the gold chloride salt and simultaneously reducing molecular oxygen to water. The high temperature of the system then allows for disproportionation at the surface of the nanoparticle, depositing Au^0 atoms back onto

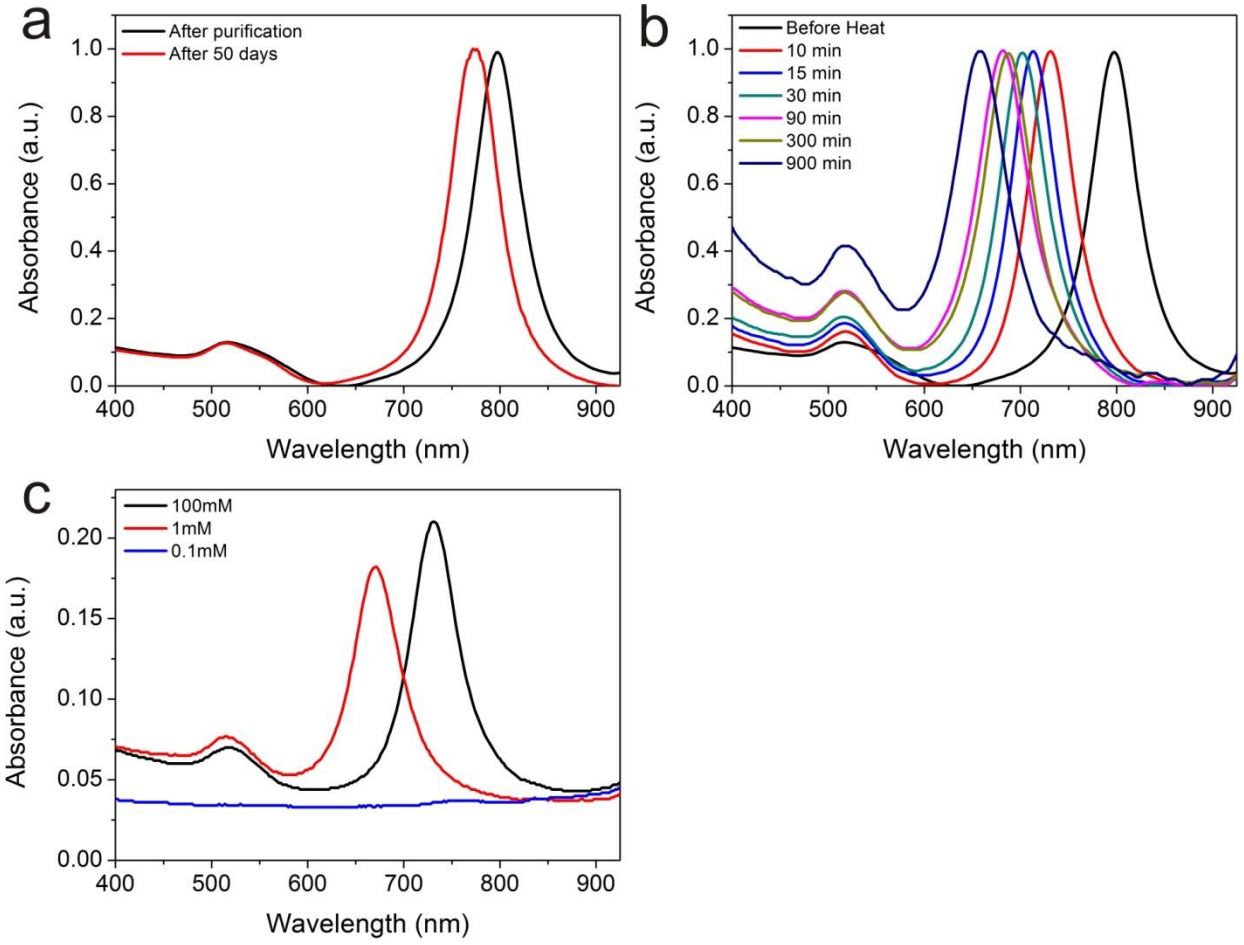

Figure 2.13 UV-Vis-NIR spectra resulting from oxidative etching (a) UV-Vis-NIR spectra of bipyramids immediately after purification and after 50 days stored at room temperature. **(b)** UV-Vis-NIR spectra from oxidatively etching the bipyramids in the presence of 100 mM CTAB at 120 °C. After 10, 15, 30, 90, 300 and 900 min, the vials were cooled down with room temperature water to halt the oxidative process. **(c)** Spectra from heating for 10 min at 120 °C with 100 mM, 1 mM, 0.1 mM CTAB. The effect of CTAC was not studied because of the low stability of the bipyramids in the presence of CTAC.

the surface in low-energy and low-defect areas[44]. This process cycles, continuously removing atoms at defect areas and replacing them in defect-free areas, until the particle reaches an energy minimum, in this case a gold nanorod. At room temperature, a similar kinetic process still occurs, but resulting in a blue-shift of the LSPR peak of less than a couple nanometers every day (Figure

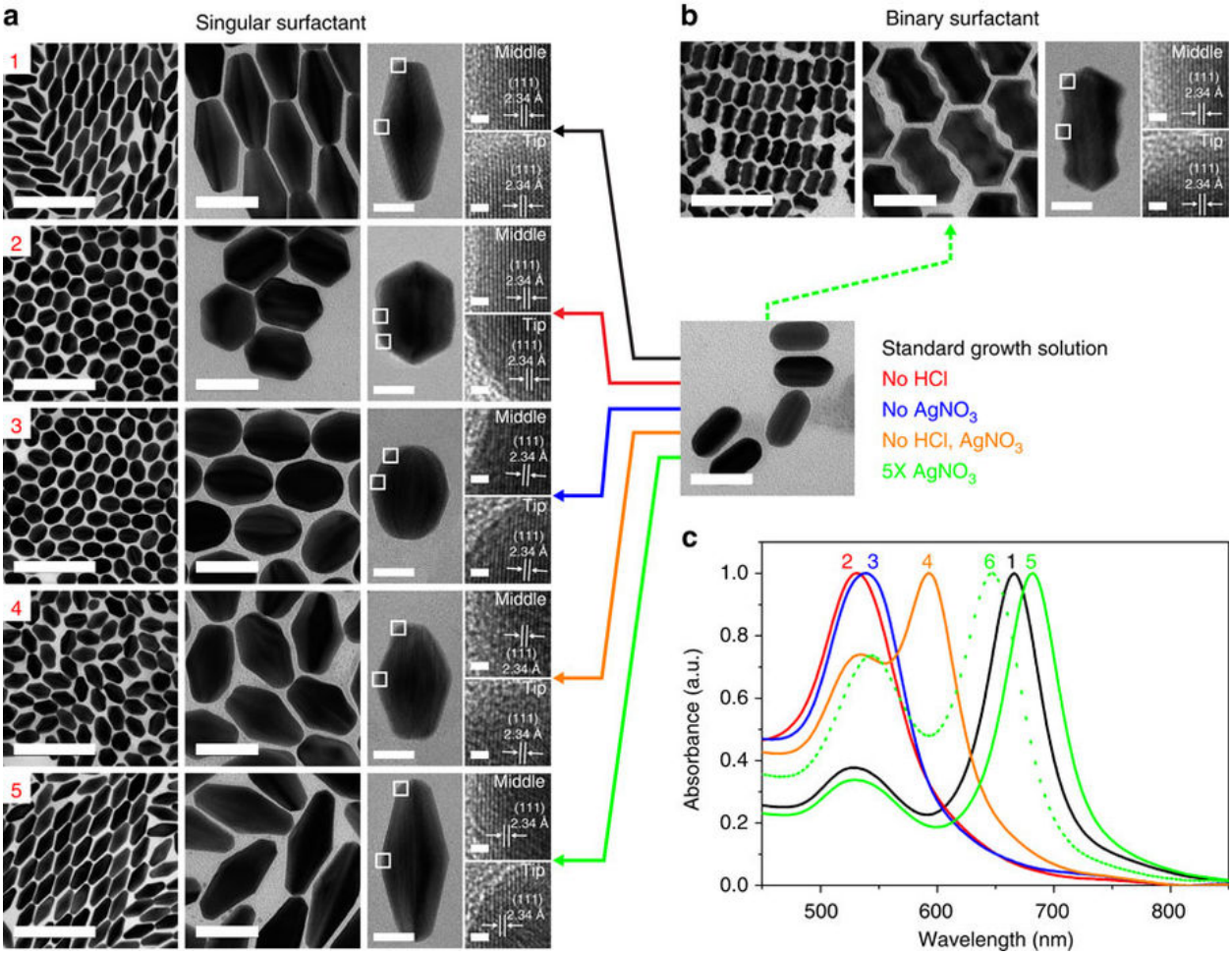

Figure 2.14 Controlling the shape of oxidatively etched nanorods through the regrowth with singular and binary surfactants (a,b) TEM and HR-TEM images of monodisperse, regrown structures from the oxidatively etched nanorods in Figure 2.12a (90 min heating) with singular surfactant (a) and binary surfactants (b). The colored arrows indicate the specific conditions for regrowth (See also Table 2.3 for detailed conditions). Magnified images showing the lattice fringes represent the areas marked with white boxes at the tip and middle of particles. **(c)** Normalized UV-Vis-NIR spectra of the regrown structures with singular surfactant (1–5 correspond to 1–5 in panel a) and binary surfactants (6 corresponds to b) are shown. See Table 2.2 for detailed size measurements. Scale bars, 200, 50, 20 and 1 nm (from low to high magnification respectively).

2.13a). This indicates the thermodynamic nature of the reaction, and that the etching of the bipyramid to the nanorod could be further accelerated by increasing the temperature. When CTAB is used as a protective agent and etchant, the reaction slows, requiring nearly an order of magnitude longer to obtain the analogous structures to the ones obtained from heating for 30 mins in Figure 2.12a (Figure 2.13b). These reaction rates are qualitatively consistent with generally accepted reactivates of halides[44]. It is noteworthy that the etching reaction rate can be increased by decreasing the concentration to the critical micelle concentration of the surfactant (1mM), which results in lessened protection of the nanoparticles from the oxidative species (Figure 2.13c).

To extend our regrowth strategy to other structures, we further synthesize regrown structures using the monodisperse etched structures as seeds with both singular and binary surfactants. Figure 2.14 shows TEM images and UV-Vis-NIR spectra of regrown structures using the rod shape particles from etching as seeds. The growth behaviors from etched particles using unitary and binary surfactants were confirmed to be very similar, likely to due to the absence of the sharp tips that affect the tip of gold bipyramids. Interestingly, the rice shape particles from the etching can be reversed to the original structure of bipyramids when the standard growth solution is used for the regrowth (Figure 2.15). On the other hand, the regrowth of rod shape particles with standard growth solution cannot be fully reversed to the bipyramids, instead forming a bifrustum, ultimately lacking the sharp tips of a bipyramid (Fig. 2.14a condition 1). Applying the same growth conditions as bipyramids, new types of nanostructures from bifrustum to short dumbbell were synthesized using the etched particles, with plasmonic resonances covering the short wavelength region between 500 and 800nm. All of the regrown structures from the etched rod-shaped particles using singular or binary surfactants are also confirmed to have similar FFT patterns as the bipyramids in Figure 2.10b (Figure 2.11).

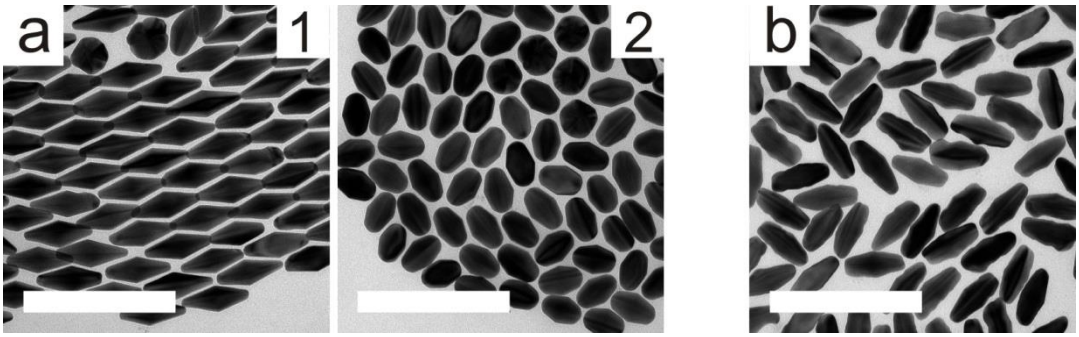

Figure 2.15 Regrown structures from oxidatively-etched particles (a) Regrown structures from etched rice-shaped particles in Figure 2.12a-2 with a standard growth solution (1) and growth solution without AgNO3 (2) with CTAB singular surfactant (See also Table 2.3 for details). **(b)** TEM image of regrown structure from etched rod-shaped particle as in Figure 2.10a-3 with standard growth solution with binary surfactants [CTAC]:[CTAB] = 90:1. All scale bars are 200 nm.

2.2.5 Conclusion

The regrowth strategy we have described has successfully synthesized various, novel gold nanoparticle geometries based on the bipyramid shape. The purity and monodispersity of the bipyramid results in a likewise pure and uniform product ranging from augmented bipyramids, dumbbells with spherical, pointed, and rod-like tips, bifrustums and spherical polyhedra. Regrowth of bipyramids in a single surfactant can be controllably tuned to give a length of well over 200 nm and a longitudinal plasmonic resonance peak well into the near-infrared range, as well as allowing for control of the aspect ratio. Regrowth with binary surfactant systems offer insight into the localization of particular surfactants on the particle surface. When combined with varying concentrations of acid and silver offer the opportunity to yield unique geometries. In addition, the high-energy nature of the bipyramid structure allows for controllable oxidative etching using only molecular oxygen as the etchant to create highly monodisperse nanorice and nanorod structures, which have additionally been regrown using the same procedure. Finally, the various growth conditions starting from the highly monodisperse but twinned structure of the bipyramids allows

to create noble metal nanoparticles of a wide range of size and shape with unprecedented narrow distribution, and this will be key in future efforts to assemble these structures for shaping the optical response for potential applications in self-assembly, non-linear optics and surface-enhanced Raman spectroscopy (SERS).

2.3 Methods

2.3.1 Synthesis and purification of gold bipyramids

The gold bipyramids were synthesized according to the previous literature procedure. Briefly, gold seeds were prepared with 18.95 mL of ultrapure water, 0.25 mL of 10 mM $HAuCl_4$ and 0.5 mL of freshly prepared 10 mM sodium citrate, followed by adding 0.3 mL of fresh and ice-cold 10 mM $NaBH_4$ under 500 rpm with magnetic stirrer at room temperature. The reaction mixture was stirred for 2 h, and aged for a week before use. The solution resulted in an orange-pink color. After aging, seed solutions are stable for a month and give reproducible results for the synthesis of bipyramids.

The bipyramids were grown in a solution containing 10 mL of 0.1 M CTAB, 0.5 mL of 0.01 M $HAuCl_4$, 0.1 mL of 0.01 M $AgNO_3$, 0.2 mL of 1 M HCl, 0.08 mL of 0.1 M ascorbic acid, and varying amounts of seed solution; shown were seed volumes of 110, 100, 95, 80 and 60 μL corresponding to 1–5 in Figure 2.3a and Table 2.1. The solution was gently stirred at 400 rpm, and was kept in an oil bath at 30 °C for 2 h. The colloid was centrifuged at 13,000g at 30 °C for 15 min, and washed with 10 mL of 1 mM CTAB, performed twice. After removing the supernatant, the precipitate was redispersed in 3 mL of 1 mM CTAB solution for further purification. Volumes of 0.5 M BDAC solution and ultrapure water were added to the 3 mL of crude bipyramid solution to obtain 10 mL of solution with the desired BDAC concentration. The concentration of BDAC desired is dependent on the size of the gold bipyramids and was determined experimentally (Figure

2.3). Concentrations of BDAC used were 230, 260, 310, 320 and 350 mM corresponding to the bipyramids prepared with 60, 70, 95, 100 and 110 μL of seed solutions, respectively. The solution was mixed and left undisturbed in an incubator at 30 °C for 11 h. The resulting pink supernatant was carefully removed, and 3 mL of 1 mM CTAB was added to the vial to redisperse the precipitate. The vial was then sonicated for 1 min. The resulting purified solution (brown in colour) was centrifuged at 8,000g for 8 min and washed with 1 mL of 1 mM CTAB, repeated twice, to remove the excess BDAC. Finally, the purified bipyramids were redispersed in 1.5 mL of 1 mM CTAB solution to be used for all regrowth reactions. The purified bipyramids in Figure 2.4a prepared with 80 mL of seed solution were used as seeds for all regrowth reactions.

2.3.2 Size augmentation of bipyramids

The size of gold bipyramids can be controlled using either a different concentration of growth solution or different amount of purified seed solution. For the typical preparation of regrowth solution, 0.9 mL of 0.1 M CTAB solution was kept for 5 min in an oil bath at 30 °C with magnetic stirring at 400 rpm. $HAuCl_4$, $AgNO_3$, HCl and ascorbic acid were then added sequentially as detailed in Table 1 and kept for 5 min. Finally, an amount of purified bipyramid seed solutions (Table 1) was added and kept for 2 h. To maintain the reaction volume constant, the varied amount of purified bipyramid seed solutions were adjusted to 0.1 mL with 1 mM CTAB. The resulting solution was centrifuged at 7,000g for 8 min and washed with 1 mM CTAB, repeated twice, then redispersed in 1 mM CTAB for further characterization.

2.3.3 Controlling the shape of nanoparticles

Various tips and unique shape of structures can be controlled with single or binary surfactants along with modified growth solutions as detailed in Table 2.3. The procedure with a single surfactant is similar to the enlarging of the bipyramid, except the condition adding

Fig. No.	Surfactant		$HAuCl_4$		$AgNO_3$		AA*		1 N HCl	Vol.(μL) of BP* seeds	pH*	[CTAB]:[CTAC]
	0.1M CTAB Vol.(μL)	0.1M CTAC Vol.(μL)	Conc.(M)	Vol.(μL)	Conc.(M)	Vol.(μL)	Conc.(M)	Vol.(μL)	Vol.(μL)			
2.4c-6	900	-	0.002	50	0.002	10	0.02	8	20	50 (in 1 mM CTAB)	1.73	CTAB only
2.4c-7										10 (in 1 mM CTAB)		
2.4c-8			0.004	50	0.004	10	0.04	8		30 (in 1 mM CTAB)		
2.4c-9										20 (in 1 mM CTAB)		
2.4c-10										10 (in 1 mM CTAB)		
2.5a-1	900	-	0.001	50	0.001	10	0.01	8	20	100 (in 1 mM CTAB)	1.73	CTAB only
2.5a-2			0.004		0.004		0.04					
2.5a-3			0.01		0.01		0.1					
2.5a-4			0.02		0.02		0.2					
2.5a-5			0.002		0.002		0.02			5 (in 1 mM CTAB)		
2.5a-6			0.004		0.004		0.04					
2.5b-1					0.002							
2.5b-2					0.004							
2.5b-3					0.008							
2.5b-4			0.002				0.02		20 (0.2N)	100 (in 1 mM CTAB)	2.435	
2.6a-1, 2.5b-5					0.002				20		1.73	
2.5b-6									24		1.656	
2.7b-1	-	900	0.002	50	0.002	10	0.02	8	20	100 (in 0.1 mM CTAB)	1.73	1:9000
2.7b-2										100 (in 1 mM CTAB)		1:900
2.7b-3										100 (in 2 mM CTAB)		1:450
2.6b-6, 2.7b-4										100 (in 10 mM CTAB)		1:90
2.7b-5										100 (in 100 mM CTAB)		1:9
2.7b-6	400	500										1:1
2.7b-7	800	100	0.002	50	0.002	10	0.02	8	20			9:1
2.7b-8	800	10 (0.01M)	0.002	50	0.002	10	0.02	8	20			90:1
2.6a-2	900	-	0.002	50	0.002	10	0.02	8	20μL DIW added	100 (in 1 mM CTAB)	3.62	CTAB only
2.6a-3					10μL DIW added				20		1.73	
2.6a-4									20μL DIW added		3.62	
2.6a-5					0.01	10			20		1.73	
2.6b-7	-	900	0.002	50	0.002	10	0.02	8	20μL DIW added	100 (in 10 mM CTAB)	3.62	90:1
2.6b-8					10μL DIW added				20		1.73	
2.6b-9									20μL DIW added		3.62	
2.6b-10					0.01	10			20		1.73	
2.14a-1	900	-	0.002	50	0.002	10	0.02	8	20	Rod seeds from etching 100 (in 1 mM CTAB)	1.73	CTAB only
2.14a-2									20μL DIW added		3.62	
2.14a-3					10μL DIW added				20		1.73	
2.14a-4									20μL DIW added		3.62	
2.14a-5					0.01	10			20		1.73	
2.14b		900	0.002	50	0.01	10	0.02	8	20	Rod seeds from etching 100 (in 10 mM CTAB)	1.73	90:1
2.15a-1	900	-	0.002	50	0.002	10	0.02	8	20	Rice seeds from etching 100 (in 1 mM CTAB)	1.73	CTAB only
2.15a-2					10μL DIW added							
2.15b	-	900			0.002	10				Rod seeds from etching 100 (in 10 mM CTAB)		90:1

Table 2.3 The regrowth conditions employed with either singular or binary surfactants. Total reaction volume remains constant across all trials (1.088 mL). *AA=Ascorbic Acid, BP=Bipyramid, pH=calculated values.

chemicals. For the synthesis without HCl, $AgNO_3$ or both, the same volume of nanopure water is added to the regrowth solution in its stead. For excess amount of $AgNO_3$, a higher concentration of solution is used with the same volume as the standard regrowth solution. 100 μL of purified bipyramid seed solution in 1 mM CTAB is added to the prepared regrowth solution and kept for 2h. For the typical preparation of regrowth solution with binary surfactants, 0.1 M CTAC was kept

for 5 min in an oil bath at 30 °C with magnetic stirring at 400 rpm. 100 μL of purified bipyramid seed solution is centrifuged at 7,000g and redispersed in 0.1 mL of desired concentration of CTAB solution to adjust the ratio between the surfactants (CTAC and CTAB). The reactants with purified bipyramid seed were added same as above and kept at 30 °C for 2 h to complete the reaction. The resulting solution was centrifuged at 7,000g for 8 min and washed with 1 mM CTAB, repeated twice, then redispersed in 1 mM CTAB for further characterization.

2.3.4 Oxidative etching of bipyramids

For oxidative etching, 100 μL of purified bipyramids in 1 mM CTAB was added to 900 μL of 100 mM BDAC solution with no other reagents. A glass vial with screw cap was sealed with Teflon tape to prevent the leakage of vapor during the heating. The sealed vial was placed in an oil bath pre-heated at 120 °C and kept under stirring at 300 rpm with magnetic stirrer. Use caution when heating the sealed container as pressure will build inside the flask. Properly sealing the vial is also crucial to controlling the reaction speed, as any leaks will accelerate the reaction. After 10, 15, 30, 60, 90 and 210 min, the vials were cooled to room temperature with a water bath to halt the oxidative process. The resulting solution was centrifuged at 8,000g for 8 min and washed with 1 mM CTAB, repeated twice and then redispersed in 100 mL of 1 mM CTAB for further regrowth and characterization. See Table 2.3 for the detailed conditions for regrowth.

2.4 References

1. Lee JH, Nam JM, Jeon KS, Lim DK, Kim H, Kwon S, *et al*. Tuning and maximizing the single-molecule surface-enhanced Raman scattering from DNA-tethered nanodumbbells. *ACS Nano* 2012, **6**(11)**:** 9574-9584.

2. Liu GL, Yin Y, Kunchakarra S, Mukherjee B, Gerion D, Jett SD, *et al*. A nanoplasmonic molecular ruler for measuring nuclease activity and dna footprinting. *Nature Nanotechnology* 2006, **1**(1)**:** 47-52.

3. Lee JH, You MH, Kim GH, Nam JM. Plasmonic nanosnowmen with a conductive junction as highly tunable nanoantenna structures and sensitive, quantitative and multiplexable surface-enhanced Raman scattering probes. *Nano Letters* 2014, **14**(11)**:** 6217-6225.

4. Ghosh P, Han G, De M, Kim CK, Rotello VM. Gold nanoparticles in delivery applications. *Advanced Drug Delivery Reviews* 2008, **60**(11)**:** 1307-1315.

5. Darbha GK, Singh AK, Rai US, Yu E, Yu H, Ray PC. Selective detection of mercury (II) ion using nonlinear optical properties of gold nanoparticles. *Journal of the American Chemical Society* 2008, **130**(25)**:** 8038-8043.

6. Eustis S, El-Sayed MA. Why gold nanoparticles are more precious than pretty gold: Noble metal surface plasmon resonance and its enhancement of the radiative and nonradiative properties of nanocrystals of different shapes. *Chemical Society Reviews* 2006, **35**(3)**:** 209-217.

7. Prodan E, Radloff C, Halas NJ, Nordlander P. A Hybridization Model for the Plasmon Response of Complex Nanostructures. *Science* 2003, **302**(5644)**:** 419-422.

8. Savage KJ, Hawkeye MM, Esteban R, Borisov AG, Aizpurua J, Baumberg JJ. Revealing the quantum regime in tunnelling plasmonics. *Nature* 2012, **491**(7425)**:** 574-577.

9. Liu M, Guyot-Sionnest P, Lee TW, Gray SK. Optical properties of rodlike and bipyramidal gold nanoparticles from three-dimensional computations. *Physical Review B - Condensed Matter and Materials Physics* 2007, **76**(23).

10. Liu M, Guyot-Sionnest P. Mechanism of silver(I)-assisted growth of gold nanorods and bipyramids. *Journal of Physical Chemistry B* 2005, **109**(47)**:** 22192-22200.

11. Kou X, Ni W, Tsung CK, Chan K, Lin HQ, Stucky GD*, et al*. Growth of gold bipyramids with improved yield and their curvature-directed oxidation. *Small* 2007, **3**(12)**:** 2103-2113.

12. Kou X, Zhang S, Tsung CK, Yeung MH, Shi Q, Stucky GD*, et al*. Growth of gold nanorods and bipyramids using CTEAB surfactant. *Journal of Physical Chemistry B* 2006, **110**(33)**:** 16377-16383.

13. Kou X, Zhang S, Tsung CK, Yang Z, Yeung MH, Stucky GD*, et al*. One-step synthesis of large-aspect-ratio single-crystalline gold nanorods by using CTPAB and CTBAB surfactants. *Chemistry - A European Journal* 2007, **13**(10)**:** 2929-2936.

14. Park K, Koerner H, Vaia RA. Depletion-induced shape and size selection of gold nanoparticles. *Nano Letters* 2010, **10**(4)**:** 1433-1439.

15. Lee J-H, Gibson KJ, Chen G, Weizmann Y. Bipyramid-templated synthesis of monodisperse anisotropic gold nanocrystals. *Nature communications* 2015, **6**.

16. Rodríguez JR, Czapkiewicz J. Conductivity and dynamic light scattering studies on homologous alkylbenzyldimethylammonium chlorides in aqueous solutions. *Colloids and Surfaces A: Physicochemical and Engineering Aspects* 1995, **101**(2-3)**:** 107-111.

17. Bakshi M, Kaur I. Head-group-induced structural micellar transitions in mixed cationic surfactants with identical hydrophobic tails. *Colloid and Polymer Science* 2003, **281**(1)**:** 10-18.

18. Alargova R, Kochijashky I, Zana R. Fluorescence study of the aggregation behavior of different surfactants in aqueous solutions in the presence and in the absence of gas. *Langmuir* 1998, **14**(7)**:** 1575-1579.

19. Berr S. Solvent isotope effects on alkytrimethylammonium bromide micelles as a function of alkyl chain length. *Journal of Physical Chemistry* 1987, **91**(18)**:** 4760-4765.

20. Li N, Liu S, Luo H. A new method for the determination of the first and second CMC in CTAB solution by resonance Rayleigh scattering technology. *Analytical letters* 2002, **35**(7)**:** 1229-1238.

21. Aswal V, Goyal P. Role of different counterions and size of micelle in concentration dependence micellar structure of ionic surfactants. *Chemical physics letters* 2003, **368**(1-2)**:** 59-65.

22. Ye X, Zheng C, Chen J, Gao Y, Murray CB. Using binary surfactant mixtures to simultaneously improve the dimensional tunability and monodispersity in the seeded growth of gold nanorods. *Nano Letters* 2013, **13**(2)**:** 765-771.

23. Chen H, Shao L, Li Q, Wang J. Gold nanorods and their plasmonic properties. *Chemical Society Reviews* 2013, **42**(7)**:** 2679-2724.

24. Nikoobakht B, El-Sayed MA. Preparation and growth mechanism of gold nanorods (NRs) using seed-mediated growth method. *Chemistry of Materials* 2003, **15**(10)**:** 1957-1962.

25. Langille MR, Personick ML, Zhang J, Mirkin CA. Defining rules for the shape evolution of gold nanoparticles. *Journal of the American Chemical Society* 2012, **134**(35)**:** 14542-14554.

26. Lohse SE, Burrows ND, Scarabelli L, Liz-Marzán LM, Murphy CJ. Anisotropic noble metal nanocrystal growth: The role of halides. *Chemistry of Materials* 2014, **26**(1)**:** 34-43.

27. Garg N, Scholl C, Mohanty A, Jin R. The role of bromide ions in seeding growth of Au nanorods. *Langmuir* 2010, **26**(12)**:** 10271-10276.

28. Vigderman L, Khanal BP, Zubarev ER. Functional gold nanorods: Synthesis, self-assembly, and sensing applications. *Advanced Materials* 2012, **24**(36)**:** 4811-4841.

29. Park K, Vaia RA. Synthesis of complex Au/Ag nanorods by controlled overgrowth. *Advanced Materials* 2008, **20**(20)**:** 3882-3886.

30. Umar AA, Oyama M. High-yield synthesis of tetrahedral-like gold nanotripods using an aqueous binary mixture of cetyltrimethylammonium bromide and hexamethylenetetramine. *Crystal Growth and Design* 2009, **9**(2)**:** 1146-1152.

31. Rodríguez-Fernández J, Pérez-Juste J, Mulvaney P, Liz-Marzán LM. Spatially-directed oxidation of gold nanoparticles by Au(III)-CTAB complexes. *Journal of Physical Chemistry B* 2005, **109**(30)**:** 14257-14261.

32. Kim F, Sohn K, Wu J, Huang J. Chemical synthesis of gold nanowires in acidic solutions. *Journal of the American Chemical Society* 2008, **130**(44)**:** 14442-14443.

33. Sohn K, Kim F, Pradel KC, Wu J, Peng Y, Zhou F*, et al*. Construction of evolutionary tree for morphological engineering of nanoparticles. *ACS Nano* 2009, **3**(8)**:** 2191-2198.

34. Pal T, De S, Jana NR, Pradhan N, Mandal R, Pal A*, et al*. Organized media as redox catalysts. *Langmuir* 1998, **14**(17)**:** 4724-4730.

35. Personick ML, Langille MR, Zhang J, Mirkin CA. Shape control of gold nanoparticles by silver underpotential deposition. *Nano Letters* 2011, **11**(8)**:** 3394-3398.

36. Lisiecki I, Filankembo A, Sack-Kongehl H, Weiss K, Pileni M. Structural investigations of copper nanorods by high-resolution TEM. *Physical Review B - Condensed Matter and Materials Physics* 2000, **61**(7)**:** 4968-4974.

37. Lisiecki I. Size, shape, and structural control of metallic nanocrystals. *Journal of Physical Chemistry B* 2005, **109**(25)**:** 12231-12244.

38. Johnson CJ, Dujardin E, Davis SA, Murphy CJ, Mann S. Growth and form of gold nanorods prepared by seed-mediated, surfactant-directed synthesis. *Journal of Materials Chemistry* 2002, **12**(6)**:** 1765-1770.

39. Zhou G, Yang Y, Han S, Chen W, Fu Y, Zou C*, et al*. Growth of nanobipyramid by using large sized Au decahedra as seeds. *ACS Applied Materials and Interfaces* 2013, **5**(24)**:** 13340-13352.

40. Xiao J, Liu S, Tian N, Zhou ZY, Liu HX, Xu BB*, et al*. Synthesis of convex hexoctahedral Pt micro/nanocrystals with high-index facets and electrochemistry-mediated shape evolution. *Journal of the American Chemical Society* 2013, **135**(50)**:** 18754-18757.

41. Tian N, Zhou ZY, Sun SG. Platinum metal catalysts of high-index surfaces: from single-crystal planes to electrochemically shape-controlled nanoparticles. *Journal of Physical Chemistry C* 2008, **112**(50)**:** 19801-19817.

42. Mettela G, Boya R, Singh D, Kumar GVP, Kulkarni GU. Highly tapered pentagonal bipyramidal Au microcrystals with high index faceted corrugation: Synthesis and optical properties. *Scientific Reports* 2013, **3**.

43. Elechiguerra JL, Reyes-Gasga J, Yacaman MJ. The role of twinning in shape evolution of anisotropic noble metal nanostructures. *Journal of Materials Chemistry* 2006, **16**(40)**:** 3906-3919.

44. Long R, Zhou S, Wiley BJ, Xiong Y. Oxidative etching for controlled synthesis of metal nanocrystals: Atomic addition and subtraction. *Chemical Society Reviews* 2014, **43**(17)**:** 6288-6310.

45. Tsung CK, Kou X, Shi Q, Zhang J, Yeung MH, Wang J*, et al*. Selective shortening of single-crystalline gold nanorods by mild oxidation. *Journal of the American Chemical Society* 2006, **128**(16)**:** 5352-5353.

Chapter 3 – Controllable Self-Assembly of Gold Nanostructures

3.1 Introduction

One of the most unexplored spaces in nanotechnology involves the ability to controllably and reliably assemble nanomaterials into well-defined macrostructures. When it comes to assembling nanomaterials into small, discrete, and well-defined structures, few techniques exist that are capable of reliable and consistent products. Furthermore, the use of anisotropic nanoparticles in self-assembly is extremely limited. This is due to the difficulty in regiospecific surface encoding associated with breaking the identical chemical environment on NPs. In this study, we demonstrate that the NPs' surfaces can be selectively blocked with a diblock copolymer (polystyrene-b-polyacrylic acid) by tuning the interfacial free energies of the ternary system involving the NPs, solvent and the copolymer, which results in different accessibilities to the NPs' surfaces in a controlled manner. Through the modification of the polymer-free surface region with single-stranded DNA, regiospecific and programmable surface encoding has been realized. The resultant interparticle binding potential is thereby specific and directional, and thus allows for an increased degree of complexity of potential self-assemblies. The versatility of this regiospecific surface encoding strategy has been demonstrated on various NPs of isotropic or anisotropic shape. As a result, we have constructed a total of 24 distinct complex nanoassemblies using programmable interaction between these regiospecific DNA-encoded NPs.

In recent years**,** nanoparticles (NPs) have ignited people's enthusiasm with their remarkable properties and far-reaching applications[1,2,3,4,5,6,7,8,9,10,11]. Many interesting phenomena, such as surface plasmon coupling, exciton coupling, plasmon-exciton interactions, and magnetic coupling, originate from the NPs assembly, in which NPs organize in purposeful ways and interact with one another[12,13,14]. Solution-based self-assembly is one of the practical assembly strategies to

realize the spontaneous organization of large numbers of individual NPs into ordered structures in different dimensions[15, 16, 17, 18, 19]. Whilst important developments have emerged in this field, it is still challenging to program NPs to self-assemble into pre-determined configurations, which require both specific and directional interactions. To achieve specific interactions, surface encoding of NPs with DNA was developed and applied for various NPs with different size, shape and composition. The recognition hybridizations between the complementary DNA strands on different NPs has been demonstrated to make the NPs self-assemble into a wide variety of periodic organizations.

To make the interaction between DNA-encoded NPs also directional, non-uniform surface encoding has been utilized as a reliable means. For NPs with isotropic shape, non-uniform surface encoding has been realized by attaching a single copy[20] or discrete pattern[21] of single-stranded DNA (ssDNA) directly[22, 23, 24], localizing the bonding ability to a small area. A series of discrete self-assemblies (dimer, trimer, tetramer) of NPs have been created from these non-uniformly encoded isotropic NPs[21]. Since the binding of the terminal thiol of the ssDNA is not selective enough to distinguish the various surface chemistries associated with different facets, the ssDNA attaches almost randomly to the NPs. Although it is not a problem for isotropic NPs, this nonselective attachment of ssDNA on those with anisotropic shapes, such as nanorods (NRs) or nano-triangular-prisms (TPs), is expected to generate a mixture of non-uniformly encoded NPs. In order to overcome this limitation, a regiospecific surface encoding method is necessary. One strategy in literature is to encapsulate the uniformly encoded NPs into DNA nanostructures, then the addressable surface properties of DNA nanostructures are transferred temporarily to the inside NPs. The disassembly of the outer DNA shell will recover the uniformly encoded NPs[25]. Another

strategy has split the surface encoding into two steps: first blocking the undesired NP surfaces to prevent functionalization, and then modifying the exposed region with DNA[26].

Immobilization of the target NPs onto a template, normally a planar substrate[27], microparticle[22] or emulsion[28], is a well-established strategy to achieve the partial blocking by means of steric effect, and has been well developed to achieve regiospecific encoding of isotropic NPs[29, 30]. In addition, the core-shell strategy has been also adopted to block the surface of NPs[31, 32, 33], where the shell (silica or polymer) only partially covers the core. Chemical patchiness on anisotropic NPs can be also achieved by utilizing the different packing densities[34], aggregation states or chemical properties[35, 36] of a single chemical species on different parts of the surface. Using a polymer as blocking material, Hongyu Chen and coworkers found that the coverage of polymer on NPs varied from full to partial when hydrophilic ligands were combined with hydrophobic ones[37]. This strategy has been demonstrated on both isotropic gold nanospheres (AuNSs) and anisotropic gold nanorods (AuNRs) to create patchy NPs (Janus AuNSs and two-end free AuNRs, respectively), and the partial coverage was attributed to ligand segregation on NPs. We now believe the association of the polymer on the NP surface is a three-phase wetting problem between NPs, polymer and solvent, so the final morphology of NP@polymer depends on the balance of the interfacial tensions between these three phases. Specifically, fine control over the interfacial tensions can be gained by manipulating the ratio of the solvent mixture as well as the ratio of the two types of ligands. We hypothesize that more variable and precise control over the distribution of polymer on NPs could be achieved via a carefully designed and empirically tested ligand/solvent system, making both the size and location of the blocked surface area controllable independently to achieve the regiospecific encoding of NPs. We have expanded upon the partially-encapsulated nanoparticles previously demonstrated to include six new building blocks that have

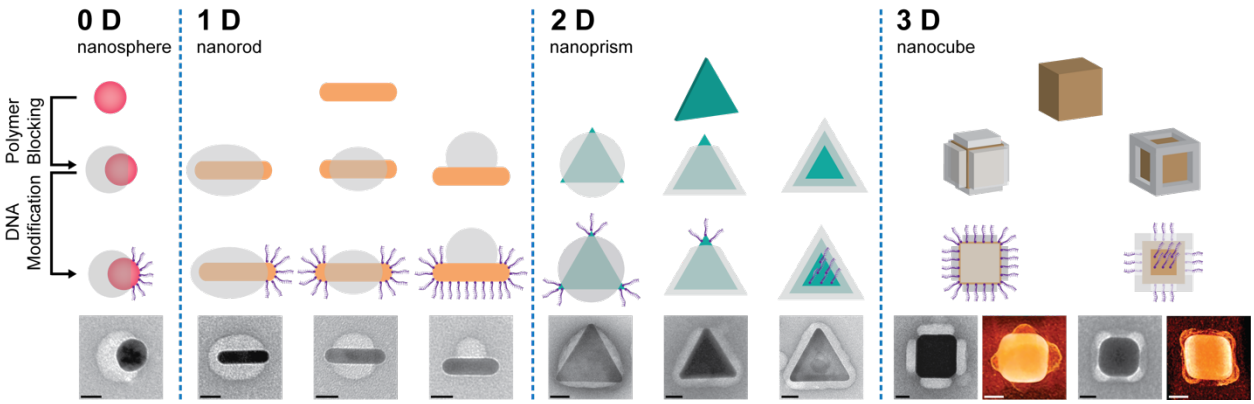

Figure 3.1 Directional and Programmable Encapsulated NPs. Left column shows the colloidal metal NPs with different sizes, shapes and compositions, which can be converted into rseNPs through polymer blocking and DNA modification. Middle left column: controllable polymer blocking will break the homogeneous surface chemistry of NPs, creating specific binding sites on it. Middle right column: DNA modification on polymer-free surface region provides specific binding force on the binding site. Right column shows the TEM images of the corresponding rseNPs. To distinguish the uncovered surface region from the polymer blocked parts, the contrast for the blocking materials-diblock copolymer PS-PAA is enhanced by negative stain with $(NH_4)_6Mo_7O_{24}$. Scale bars, 20 nm.

not been shown before. In addition, we show that the polymer-free surface regions of NPs are accessible for ssDNA modification, thus enabling regiospecific functionalization. This two-step process successfully converts the NPs into surface-encoded nanoparticles (rseNPs) with a high yield. The location and size of the polymer-free surface regions assure directionality and saturability of the interactions between different NPs, and the sequence-specific hybridization of DNA imparts specificity of these interactions. The presented approach is a significant step toward NP building blocks with highly addressable surfaces that allow for the deliberate design and synthesis of sophisticated self-assembled nanostructures.

3.2 Results and Discussion

3.2.1 Synthesis of rseNPs

The transformation of NPs into rseNPs is achieved by a two-step approach: polymer blocking of NP followed by its DNA modification, as summarized in Figure 3.1. The versatility of this approach is reflected in two aspects. Firstly, this approach is applicable to the NPs with different elemental compositions, sizes, shapes, and surface ligands, which include citrate stabilized Au nanospheres (AuNSs), CTAB stabilized Au nanorods (AuNRs), Au triangular nanoprisms (AuTPs), Au nanocubes (AuNCs) and Pd nanocubes (PdNCs). Secondly, the approach allows for selective encoding of the different surface regions of the NPs, creating rseNPs with different binding orientations. For example, the same AuNRs can be blocked in different ways, leaving only one end, two ends or one side available for counterparts to bind (Figure 3.2c).

We first demonstrated our proposed approach on citrate-stabilized AuNSs[37] as shown in Figure 3.2a and 3.2b. The polymer blocking was conducted in one pot by mixing AuNSs (30 nm), amphiphilic diblock copolymer (polystyrene-b-polyacrylic acid, PS-PAA) and two ligands in DMF-H_2O binary solvent, and then heating the solution at 105 °C for 1.5 hours (Figure 3.2a). The heating effect was directly observed during the encapsulation of AuNRs, as shown in Figure 3.3. If only hydrophobic ligand (1,2-Dipalmitoyl-*sn*-Glycero-3-Phosphothioethanol, PSH, L_A) was used, the PS-PAA blocked the entire surface of the AuNSs, resulting in fully encapsulated AuNS@PS-PAA core-shell structure (*f*-30AuNS). In contrast, heating the mixture in the presence of the hydrophilic ligand (2-methylaminoethanol, 2-MAE, L_B) alone generated mainly AuNSs that are free of polymer shell. When both L_A and L_B were present in the mixture, the surfaces of AuNSs were partially blocked by the polymer, forming Janus AuNS@PS-PAA core-shell structures (*j*-30AuNS).

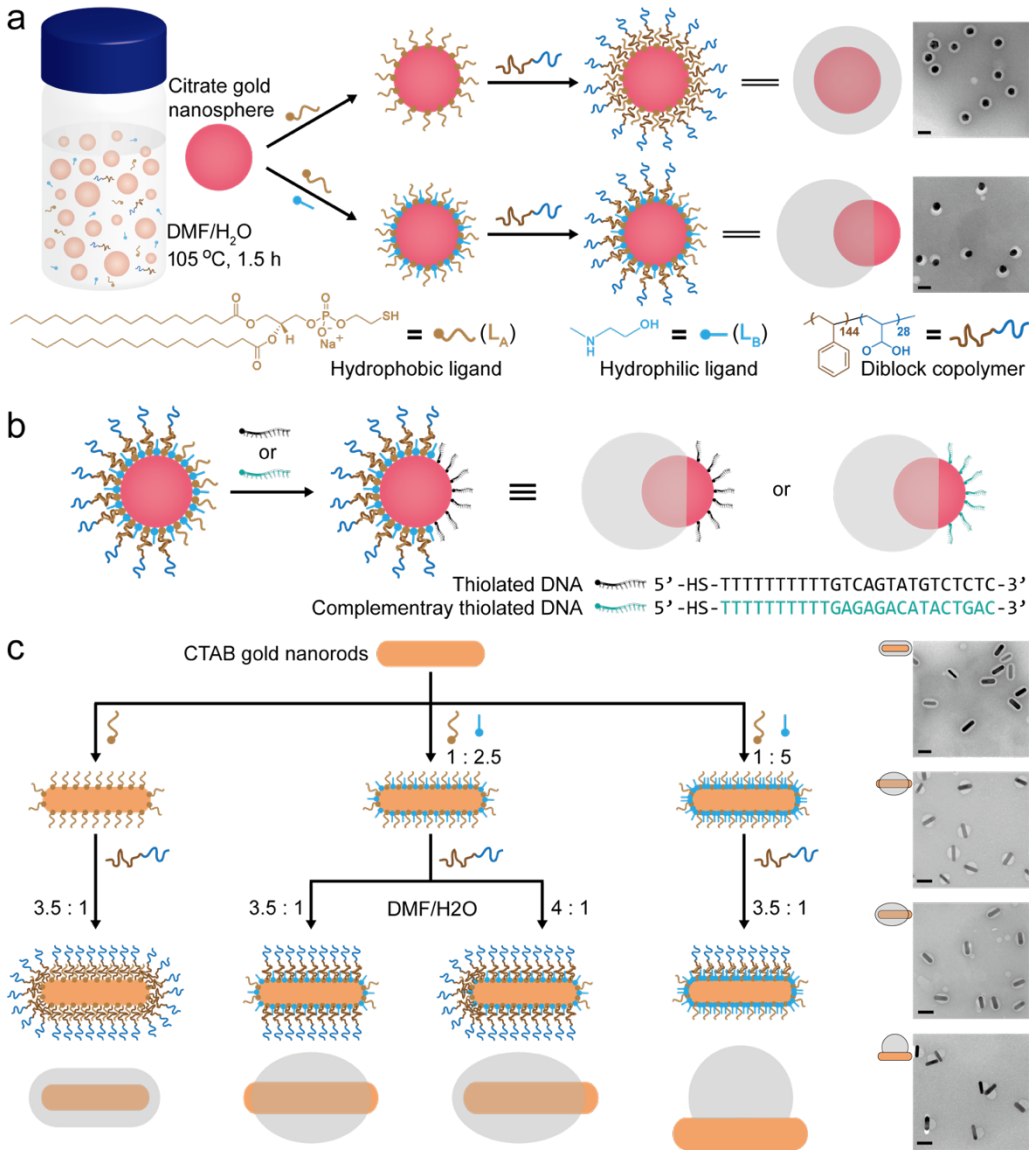

Figure 3.2 Fabrication of rseNPs. a) Generation of NP@PS-PAA core-shell structures by mixing NPs, polymer, ligands together in DMF-H2O mixed solvent and heating for 1.5 hour. The polymer coverage on the AuNS surface is controlled with the concentrations of LA and LB in the solvent mixture. TEM images showed the difference between the fully and partially blocked AuNS. **b)** The thiolated single-stranded DNA was chosen to selectively modify the polymer-free surface region of NPs, after prior reduction to release the thiol group. c, The AuNR@PS-PAA core-shell structure was generated in a similar way to the creation of AuNS@PS-PAA. The thickness of polymer shell depends on the ratio of DMF to H2O, though the polymer coverage on the AuNR was determined by the ligand ratio, allowing for the synthesis of in fully blocked, one-end uncovered, two-end uncovered and one-side uncovered structures. Scale bar, 50 nm.

3.2.2 Understanding the encapsulation through Torza and Mason model

To understand the different coverage of polymer on AuNSs, we consider this system as the contact of two phases (AuNS and PS-PAA) in a medium (DMF-H_2O solvent mixture). The resulting equilibrium is dictated by three interfacial free energies, which are denoted by $\sigma_{Au\text{-}solvent}$ ($\sigma_{Au\text{-}sol}$), $\sigma_{Au\text{-}polymer}$ ($\sigma_{Au\text{-}pol}$), and $\sigma_{polymer\text{-}solvent}$ ($\sigma_{pol\text{-}sol}$), and can be readily predicted from the spreading coefficient $S_i = \sigma_{jk} - (\sigma_{ij} + \sigma_{ik})$, as described by Torza and Mason[38], where each component in the right side of the equation represents one kind of interfacial free energy. Depending on the relative magnitudes of these energies, the flowing phase (PS-PAA) may completely or partially engulf the

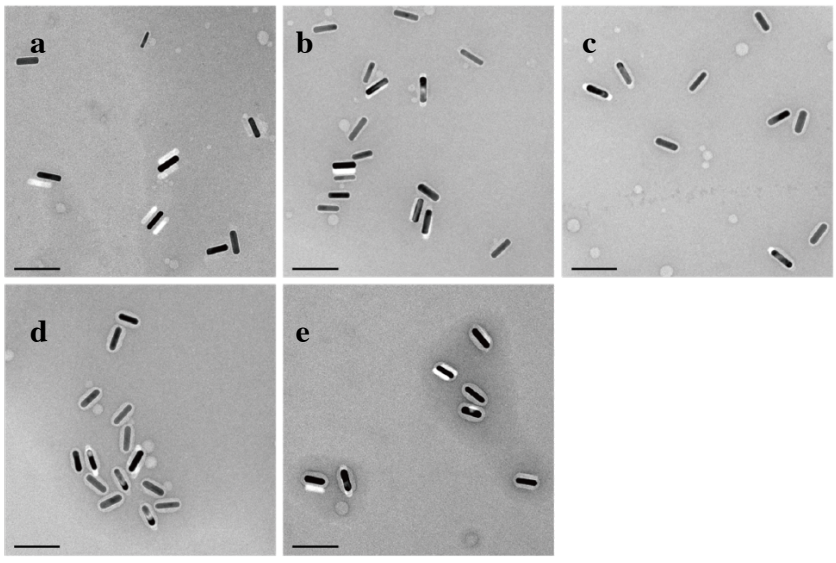

Figure 3.3 Polymer encapsulation of AuNRs at different temperature. TEM images of the AuNR@polymer structures incubated **a.** at 20 °C, **b.** at 60 °C, **c.** at 85 °C, **d.** at 100 °C, and **e.** at 110 °C while all the other experimental conditions are same to the sample f-AuNR-3 in Table 3.1. An increase of the heating temperature leads to thicker and more uniform polymer shell on AuNR surface. When the temperature is above 100 °C, the uniform polymer shell with smooth surface was formed. Scale bars, 100 nm.

solid phase (AuNS) (Figure 3.4). When the solvent ratio varies in a small range, the interfacial free energy $\sigma_{Au\text{-}sol}$, which relies on the hydrophobicity of the gold surface, can be tuned through the

binding of the ligands. Since the polymer composition is fixed, the interfacial free energy $\sigma_{Au\text{-}pol}$ relies on the ligand ratio, which dictates the hydrophobicity of the gold surface. Last, $\sigma_{pol\text{-}sol}$ is correlated to the solvent mixture because the solubility of PS block depends on solvent polarity. Therefore, we reason that, under the experimental conditions, the above three interfacial free energies can be manipulated by changing the solvent ratio and ligand ratio (Figure 3.4).

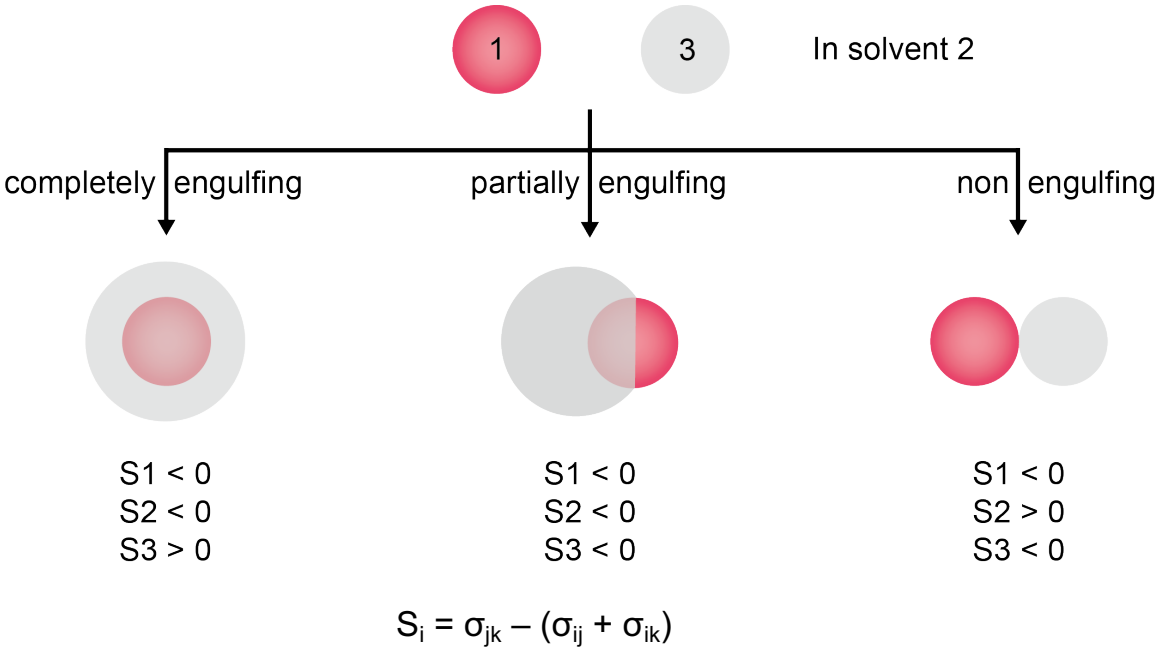

Figure 3.4 | Equilibrium configurations for two immiscible phase 1 (AuNS) and 3 (polymer) in solvent 2 (DMF/H_2O). Torza and Mason developed a model to explain how three immiscible phases interact energetically via the spreading coefficient Si, which is the overall interfacial energy from the perspective of a phase i. By independently assessing each phase (1 to 3), it is possible to qualitatively judge which interactions will be favorable and which will not, leading to various degrees of encapsulation.

This model can be applied to our current system, with the three interfacial energies in Torza and Mason's model assimilated as follows; $\sigma_{Au\text{-}Solvent}$ represents the interfacial energy between the Au surface (bare, or with ligands) and the DMF/H_2O solvent, $\sigma_{Au\text{-}Polymer}$ represents the interfacial energy between the Au surface and the polymer micelles, $\sigma_{Solvent\text{-}Polymer}$ represents the interfacial

energy between the DMF/H_2O solvent system and the polymer micelles. The equation to calculate the overall interfacial surface from the perspective of a particular phase [$S_i = \sigma_{jk} - (\sigma_{ij} + \sigma_{ik})$] will lead to three different regimes depending on how the relative magnitude of the interfacial energies. In other words, Au is phase 1, the solvent is phase 2, and the polymer is phase 3 in the model, and the interfacial energies S_1, S_2 and S_3 correspond the overall balance of the interfacial surface energies from the perspective of Au (S_{Au}), the solvent ($S_{solvent}$), and the polymer micelle ($S_{polymer}$) respectively.

The variables that are changed in our system, for various resultant encapsulations, are the ligand ratio and the DMF/H_2O solvent ratio. The ligand ratio affects the interfacial energies of Au with the solvent and the polymer, with more (hydrophobic) L_A lowering $\sigma_{Au\text{-}Polymer}$ and leading greater engulfment of the Au by the polymer micelles, and more (hydrophilic) L_B lowering $\sigma_{Au\text{-}Solvent}$ and leading to a larger Au-solvent interface with less overall encapsulation. Experiments have shown that the exclusive presence of L_A results in full encapsulation ($S_{polymer} > 0$), the exclusive presence of L_B results in no encapsulation ($S_{solvent} > 0$), and that the balance in ratio of L_A and L_B leads to partial encapsulation, as seen in Table 3.1. The solvent ratio will affect the size of the polymer micelles in the encapsulation mixture, with a higher proportion of DMF (to H_2O) lowering $\sigma_{Solvent\text{-}Polymer}$, leading to a more favorable solvent-polymer interface, and therefore large micelles. These larger micelles in turn lead to more extensive encapsulation, as can be seen in Table 3.1. The equation for S_i is of little use for understanding the details of partial encapsulation (as S_{Au}, $S_{solvent}$ and $S_{polymer}$ are in balance, all close to 0), though allows adequate prediction and understanding of the results seen in Table 3.1. Overall, it is possible to qualitatively understand

the data presented here by applying Torza and Mason's model with the ligand ratio and solvent ratio as the controlling variables.

3.2.3 Encapsulation of basic building blocks

In the presence of only hydrophobic ligand (PSH, L_A), the AuNS surface is hydrophobic due to the binding of L_A. In the process of polymer blocking, $\sigma_{Au\text{-}sol}$ increased but $\sigma_{Au\text{-}pol}$ decreased ($\sigma_{Au\text{-}sol} >> \sigma_{Au\text{-}pol}$). In order to minimize the energy of the system, the interface between Au and solvent was replaced by the interface between Au and PS, making it favorable for PS-PAA to completely engulf AuNS, forming *f*-AuNS. With only hydrophilic ligand (2-MAE, L_B) binding to the AuNS surface, $\sigma_{Au\text{-}sol}$ is much smaller than $\sigma_{Au\text{-}pol}$ ($\sigma_{Au\text{-}sol} << \sigma_{Au\text{-}pol}$), making it unfavorable for PS-PAA to engulf AuNS. In this case, the PS-PAA would rather self-aggregate to form micelles than associate with the AuNS surface. When both L_A and L_B are present on the AuNS surface, where $\sigma_{Au\text{-}sol}$ and $\sigma_{Au\text{-}pol}$ are approximately the same magnitude ($\sigma_{Au\text{-}sol} \sim \sigma_{Au\text{-}pol}$), AuNS being partially covered by PS-PAA is favored to minimize the interfacial energies, forming *j*-AuNS or other types of partially encapsulated AuNSs.

The generality of our strategy is further demonstrated on CTAB stabilized AuNRs to create 1-D rseNPs (Figure 3.1 and 3.2c) (for clarity, each rseNPs is designated by the dimensions of the core so that, nanosphere, nanorod, nanoprism and nanocube are designated 0-D, 1-D, 2-D, and 3-D, respectively). Due to their non-spherical nature, there are a greater number of potential polymer arrangements around the anisotropic nanoparticle cores. As a result, three different types of 1-D rseNPs were created from the same AuNR: one-end free (1*e*-AuNR), two-end free (2*e*-AuNR) and one-side free (1*s*-AuNR). The synthesis of 1-D rseNPs also demonstrates the applicability of this principle to NPs stabilized with CTAB, another key stabilizing agent besides citrate.

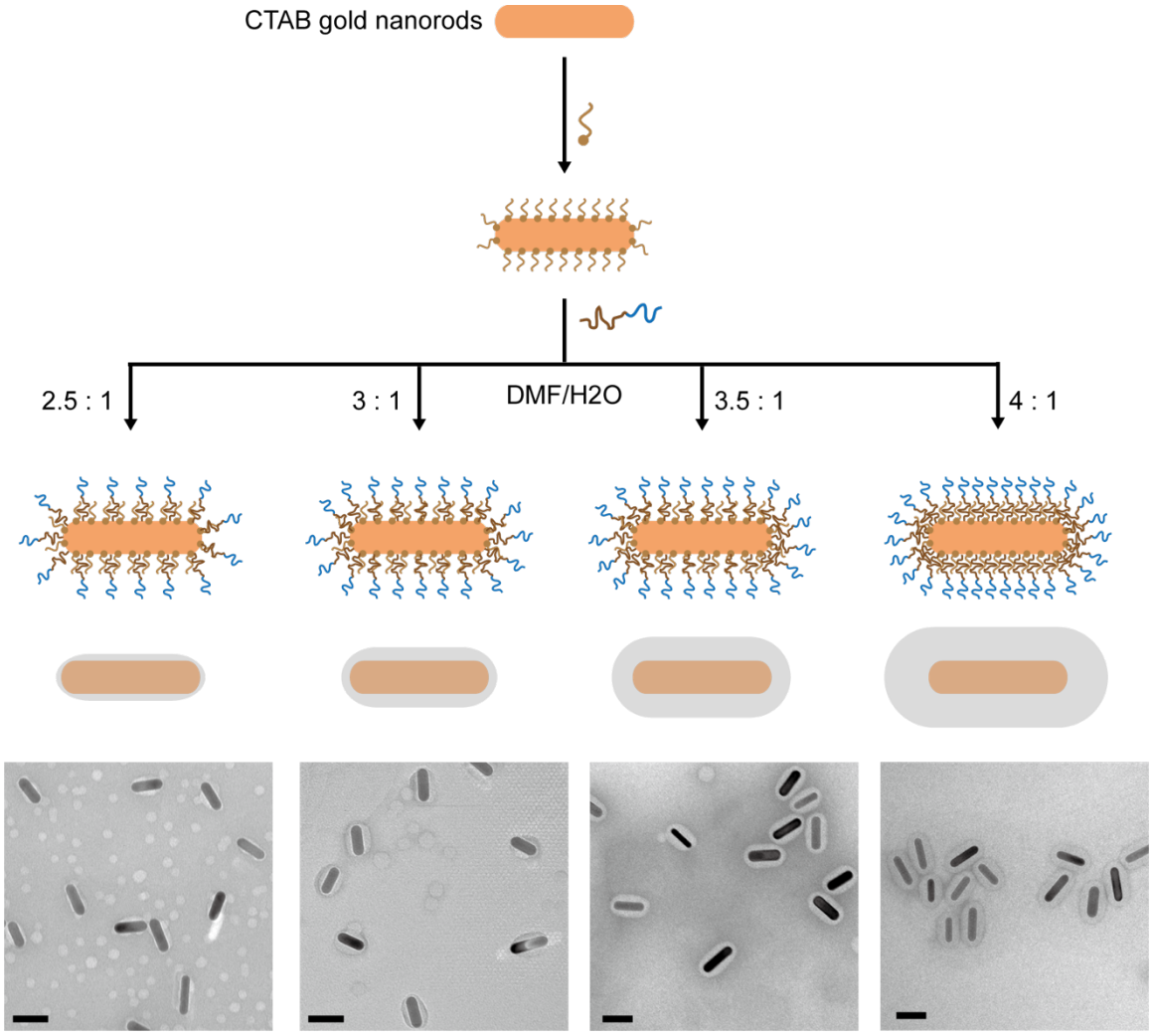

Figure 3.5 Control of the polymer shell thickness The AuNR@PS-PAA core-shell structure was generated in a similar way to the creation of AuNS@PS-PAA. The thickness of polymer shell depends on the ratio of DMF to H2O, 4.8 nm (2.5:1), 8.4 nm (3.0:1), 11.0 nm (3.5:1), 13.6 nm (4.0:1), as shown in TEM images. Scale bar, 50 nm.

Due to the interfacial free energy $\sigma_{pol\text{-}sol}$, the solvent ratio has a significant effect on the micelle size of PS-PAA, as reflected by the thickness of the polymer shell on fully encapsulated AuNRs. When the DMF/H_2O ratio increased from 2.5 to 4 with other parameters kept constant, the uniformity of the polymer shell has been improved, and their thickness increased gradually from 4.8 to 13.6 nm (Figure 3.2c and 3.5). Accordingly, the aggregation number (number of polymer molecules constituting a micelle) is correlated with the solvent ratio, and a higher

DMF/H_2O ratio forms a thicker shell surrounding the AuNR. The ability to control the thickness of the polymer shell further diversifies the structures of 1-D rseNPs, which will be discussed later.

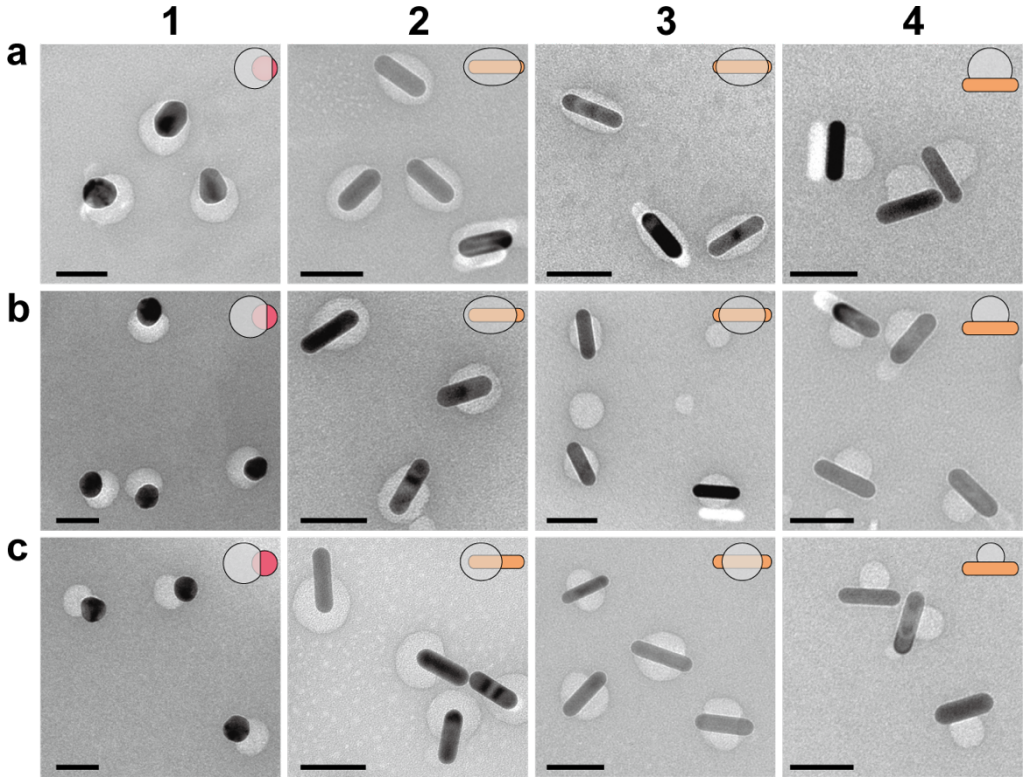

Figure 3.6 Control of the uncovered area. TEM images of different kinds of rseNPs with varied sizes of the polymer-free surface regions which can be adjusted with the encapsulation conditions. **a)** NPs with relatively small uncovered area are created at high LA-to-LB ratio. **b)** Under identical conditions but a higher concentration of LB, larger uncovered area is obtained on the same NPs. **c)** Further increasing the concentration of LB, the uncovered area on NPs also increase. rseNPs with similar shapes but different sizes of uncovered area will enrich the potential diversity of the self-assemblies further. Scale bars, 50 nm.

The dependence of polymer association on the surface energy, which can be tuned by adjusting the ligand ratio of L_A to L_B as demonstrated in the AuNR system. A larger L_B-to- L_A ratio (more hydrophilic lig) results in a greater polymer-free region; as the concentration of L_B increases, with the other conditions kept constant ([L_A] = 0.16 mM, DMF/H_2O = 3.5/1), the structure of the AuNR@PS-PAA changes from fully blocked (*f*-AuNR) to two-end free (*2e*-AuNR) and then one-side free (*s*-AuNR) (Figure 3.2c). The polymer prefers to cover the middle

of the AuNR because the flat surface of the middle prism is more favorable for the polymer to achieve compact packing. This can be explained by the decrease of $\sigma_{Au\text{-}pol}$ on the flat surface over the curved ends of the nanorod. The flat surfaces are more hydrophobic in nature as the long hydrophobic chains of L_A will result in higher methyl density than for the corresponding interface at the curved surfaces[39]. On a curved surface, the hydrophobic ligand occupies a cone-shaped area, which is less dense of hydrophobic methyl groups, and thus has less favorable $\sigma_{Au\text{-}pol}$. To obtain the 1*e*-AuNR structure, modifying the ligand ratio (i.e. $\sigma_{Au\text{-}pol}$) did not prove effective, and instead the discovered method was to change the DMF-H_2O ratio (3.5 to 4.0), decreasing $\sigma_{pol\text{-}sol}$, and leading to a larger PS-PAA-solvent interface that could accommodate more Au-polymer interactions, whilst also allowing $\sigma_{Au\text{-}sol}$ to remain competitive.

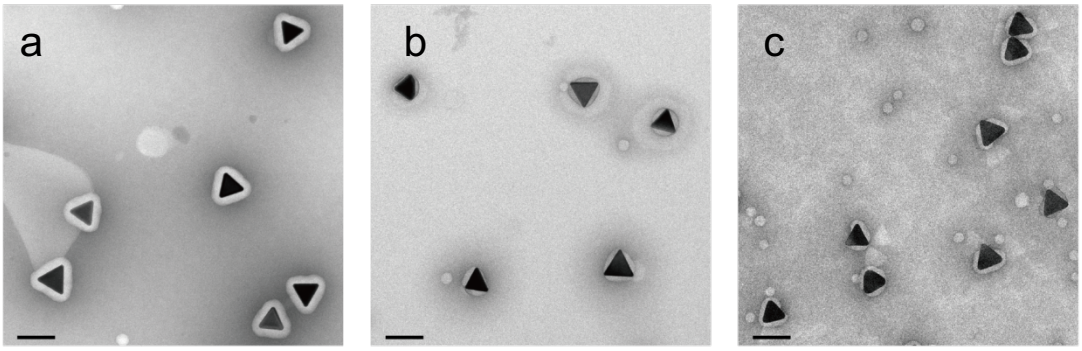

Figure 3.7 Fabrication of 2-D rseNPs from gold triangular nanoprism. Through tuning the solvent ratio and the ligand ratio, the polymer coverage on AuTP surface is varied, generating fully blocked (a, f-AuTP), three-vertex uncovered (b, 3v-AuTP) and one-vertex uncovered (c, 1v-AuTP) rseNPs. The detailed experimental conditions to control polymer coverage on the surface of AuTP are listed in Supplementary Table 1. Scale bars, 100 nm.

2-D and 3-D rseNPs were also created using AuTPs (Figure 3.7) and AuNCs (Figure 3.8), following a procedure similar to the one used to create 0-D and 1-D rseNPs. It is more favorable for the polymer to achieve compact packing on the flat facets of AuTP than the vertices with high curvature, in the presence of L_B. Two different types of 2-D rseNPs were created from the same AuTP, termed as three-vertex free (3*v*-AuTP) and one-vertex free (1*v*-AuTP) (Figure 3.7b and

3.7c). The transformation from 3*v*- to 1*v*-AuTP follows the same principle as the transformation from 2*e*- to 1*e*-AuNR, as mentioned before.

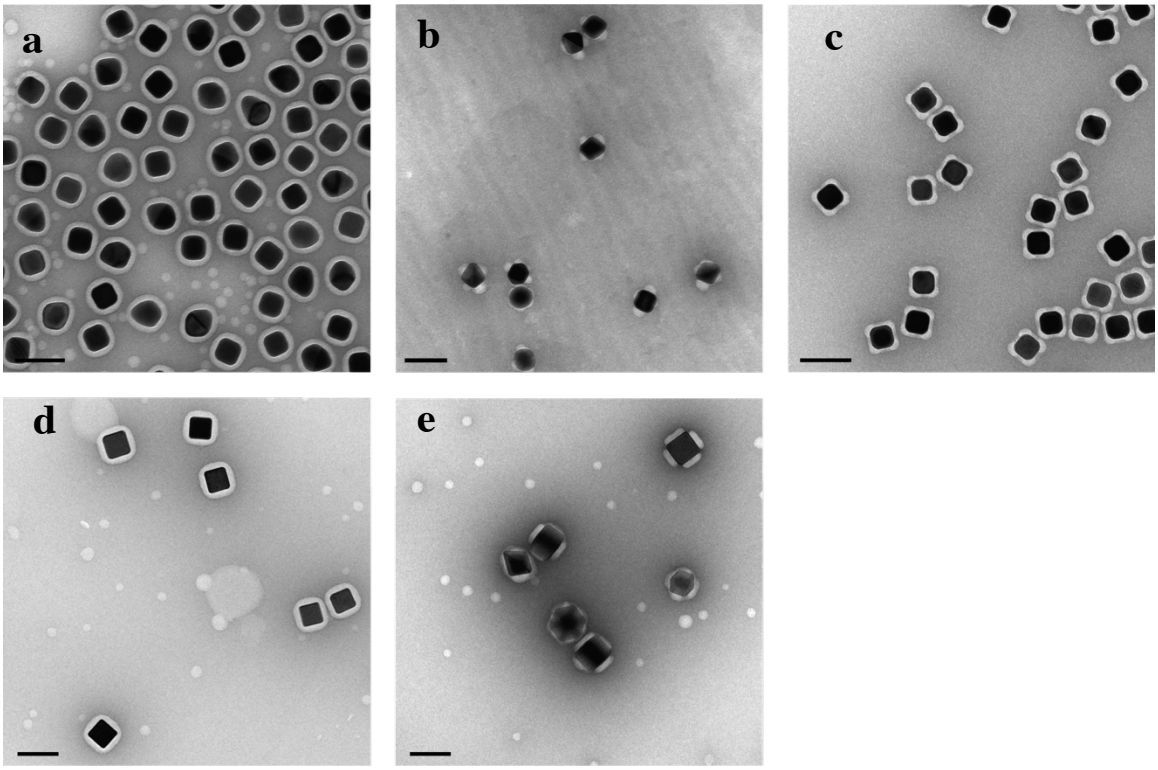

Figure 3.8 | Fabrication of 3-D rseNPs from gold and palladium nanocubes. Through tuning the solvent ratio and the ligand ratio, the polymer coverage on AuNC and PdNC surface is varied, generating fully blocked (a, f-AuNC; d, f-PdNC), edge and vertex uncovered (b, v-AuNC; e, v-PdNC), center of facet uncovered (c, c-AuNC) rseNPs. The detailed experimental conditions to control polymer coverage on the surface of AuNC are listed in Supplementary Table 1. Scale bars, 100 nm.

Two types of 3-D rseNPs based on the same AuNC with opposite polymer coverage were created by changing the identity of the hydrophilic ligand L_B at a certain pH. Using 4-mercaptobenzoic acid (4-MBA) as the hydrophilic ligand, the polymer preferred to cover the six flat facets of the cubes and leave all the edges and vertices free. Under acidic conditions, while using 2-MAE as the hydrophilic ligand, the polymer selectively covered all the edges and vertices, leaving the center of six facets free (*c*-AuNC, Figure 3.8c). When this approach was applied to PdNCs, polymer blocking similar to that of *v*-AuNC was formed where the polymer selectively

Nanoparticle			DMF	Polymer			H2O		Hydrophilic			Hydrophobic			HCOOH/NaOH				
Type	Size (nm)	Name	Vol. (uL)	Conc. (mM)	Vol. (uL)	Final Conc. (mM)	Vol. (uL)	DMF/H2O	Conc. (mM)	Vol. (uL)	Final Conc. (mM)	Conc. (mM)	Vol. (uL)	Final Conc. (mM)	Conc. (mM)	Vol. (uL)	Final Conc. (mM)	Yield (%)	A (%)
AuNS	19.8 ± 1.3	f-20AuNS	602	0.25	150	0.04	188	4	--	--	--	2.74	60	0.16				99	--
		j-20AuNS-1					186			2	0.2							95	15
		j-20AuNS-2					185		100	3	0.3							96	47
		j-20AuNS-3					184			4	0.4							98	78
	29.9 ± 2.4	f-30AuNS					188		--	--	--							99	--
		j-30AuNS-1					185			3	0.3							93	24
		j-30AuNS-2					184		100	4	0.4							95	52
		j-30AuNS-3					183			5	0.5							96	73
AuNR	L: 54.3 ± 3.4 W: 14.1 ± 1.1	f-AuNR-1	552	0.25	150	0.04	268	2.5	--	--	--	2.74	60	0.16				99	--
		f-AuNR-2	555				235	3	--	--	--							99	--
		f-AuNR-3	581				209	3.5	--	--	--							99	--
		f-AuNR-4	602				188	4	--	--	--							99	--
		2e-AuNR-1					205			4	0.4							88	9
		2e-AuNR-2	581				204	3.5		5	0.5							90	24
		2e-AuNR-3					203			6	0.6							93	33
		1e-AuNR-1					205			4	0.4							81	14
		1e-AuNR-2	602				203	4	100	5	0.5							86	35
		1e-AuNR-3					201			6	0.6							90	47
		s-AuNR-1					201			8	0.8							92	--
		s-AuNR-2	581				199	3.5		10	1							95	--
		s-AuNR-3					197			12	1.2							94	--
AuTP	72.7 ± 10.6	f-AuTP	602	0.25	150	0.04	188	4	--	--	--	2.74	60	0.16				99	--
		3v-AuTP	581				203	3.5	100	6	0.6							92	--
		1v-AuTP	602				182	4		6	0.6							78	--
AuNC	44.4 ± 2.6	f-AuNC	592	0.25	150	0.04	198	3.75	--	--	--	2.74	60	0.16	100**	8	0.8	99	--
		c-AuNC	592				186	3.75	100	4	0.4							96	--
		v-AuNC	592				191	3.75	20	7	0.14							85	--
PdNC	47.5 ± 4.9	f-PdNC	602	0.25	150	0.04	188	4	--	--	--	2.74	60	0.16				99	--
		v-PdNC	602				178	4	20	10	0.2							95	--

Table 3.1 The size distribution of nanoparticles and the blocking conditions employed to create various rseNPs. Total reaction volume remains constant across all trials (1.0 mL). AuNS = gold nanosphere, AuNR = gold nanorod, AuTP = gold triangular nanoprism, AuNC = gold nanocube. The yield of rseNPs is calculated over 100 nanoparticles of each from TEM images. The hydrophobic ligand is 2-dipalmitoyl-*sn*-glycero-3-phosphothioethanol (sodium salt) (PSH), and the hydrophilic ligand is 2-(methylamino)ethanol (2-MAE), whereas 4-mercaptobenzoic acid (4-MBA) was used to prepare v-AuNC and v-PdNC. ** concentration of formic acid.

bound to the faces of the cube (Figure 3.8e). Although the variability of the polymer blocking on nanocubes has only been empirically determined, from these observations we believe that: (1) the different hydrophilic ligands bind to the nanocube surfaces with slightly different affinities, affecting the interfacial energies enough to create the opposite polymer binding, and (2) the pH of the system, which can change the size and morphology of the self-assembled polymer micelle[40], could act as another variable of $\sigma_{pol\text{-}sol}$ enabling further tuning of the encapsulation process through the surface energy. The structural information of the AuNC@PSPAA structures was obtained using 3-D electron tomography to visualize a location of polymer on the cube surfaces. All other

rseNPs can be conclusively determined using standard TEM projection viewing, however, the nanocube structures due to their characteristics, necessitates 3-D probing to unambiguously establish the distribution of polymer and binding modes. The proposed structures of c-AuNC and v-AuNC were confirmed by tomography.

The size of the polymer-free surface region can also be tuned through the adjustment of the ratio of L_A to L_B in the solvent mixture. This ratio will dictate the relative binding densities of the ligands on the NP surface, as well as the surface energy, and therefore the polymer coverage: essentially, the more L_B present, the larger the polymer-free area is (Figure 3.6). Through tuning the sizes of the polymer-free regions, the saturabilities of the counterpart binding on rseNPs can be varied, consequently increasing the potential variety of self-assembled structures.

After polymer blocking, we replaced the surface ligands (L_A and L_B) on the polymer-free region with thiolated ssDNA. This process is performed in a buffer at a pH of 8.0, followed by incremental increases of the NaCl concentration[41] (Figure 3.2b). A buffer of pH=8.0 was chosen for DNA stability and so that the deprotonation of PAA provided sufficient electrostatic repulsion to prevent the polymer shells from aggregation at a high NaCl concentration. The success of ligand exchange was reflected by the higher stability of DNA-*j*-AuNS at high salt concentration (500 mM NaCl) than that of *j*-AuNS. The obtained DNA_1- and DNA_2-*j*-AuNS have the same morphology with *j*-AuNS, demonstrating that the thiol-modified ssDNA could only replace the ligands on the polymer-free region of the NP surface and does not affect the polymer encapsulation.

To confirm the presence of and quantify the amount of DNA present on the rseNPs surface, we used FAM-labeled DNA to functionalize the polymer-free surface. We performed the standard salt-aging procedure to load the DNA onto the surface and subsequently cleaved the DNA from the surface with a large excess of DTT[41]. By measuring the fluorescence of the cleaved DNA, we

can quantify the packing density of DNA on the surface. As expected the *f*-AuNS and *f*-AuNR showed no signs of DNA encoding, confirming that polymer-blocking prevents any ligand exchange. The *j*-AuNS, 1*e*-AuNR and 2*e*-AuNR all show roughly equivalent packing density of DNA, roughly one DNA strand every 30-60 nm^2 (Figure 3.9). As a control we also functionalized and cleaved DNA from bare NSs and NRs and found a packing density of one strand every 5-6 nm^2. This value agrees well with the literature on DNA packing density on AuNPs[41]. The difference in packing density can most likely be attributed to incomplete ligand exchange. Due to the strength of the Au-S bond, the presence of L_A on the polymer-free regions would likely inhibit the ligand exchange of the rseNPs and result in a lower packing density.

3.2.4 Encapsulation of other nanoparticles

The encapsulation of other nanoparticle shapes, especially gold bipyramids, became of interest as a method to further explore the limitations and mechanism behind the complex process. To begin, there was much interest in the encapsulation of gold bipyramids as a method to harness the interesting properties that exist at the tips. Encapsulation mimicking that of the 1e-AuNR on a gold bipyramid could allow more in-depth studies into the complex interactions between nanoparticles. For example, although field enhancement is well-defined and measurable[42], interactions in bulk scale involving the utilization of field enhancement have proven difficult to realize, as the localization to the tips remains very difficult for gold nanorods and yet unrealized for gold bipyramids.

Our exploration into the encapsulation of gold bipyramids explored many variations to the conditions that dictated the process. The standard conditions and range of ligand amounts and ratios as well as DMF/H_2O ratios never could show successful 1-end encapsulation. However, the 2-end encapsulation was consistent and worked over a much larger range of conditions than for

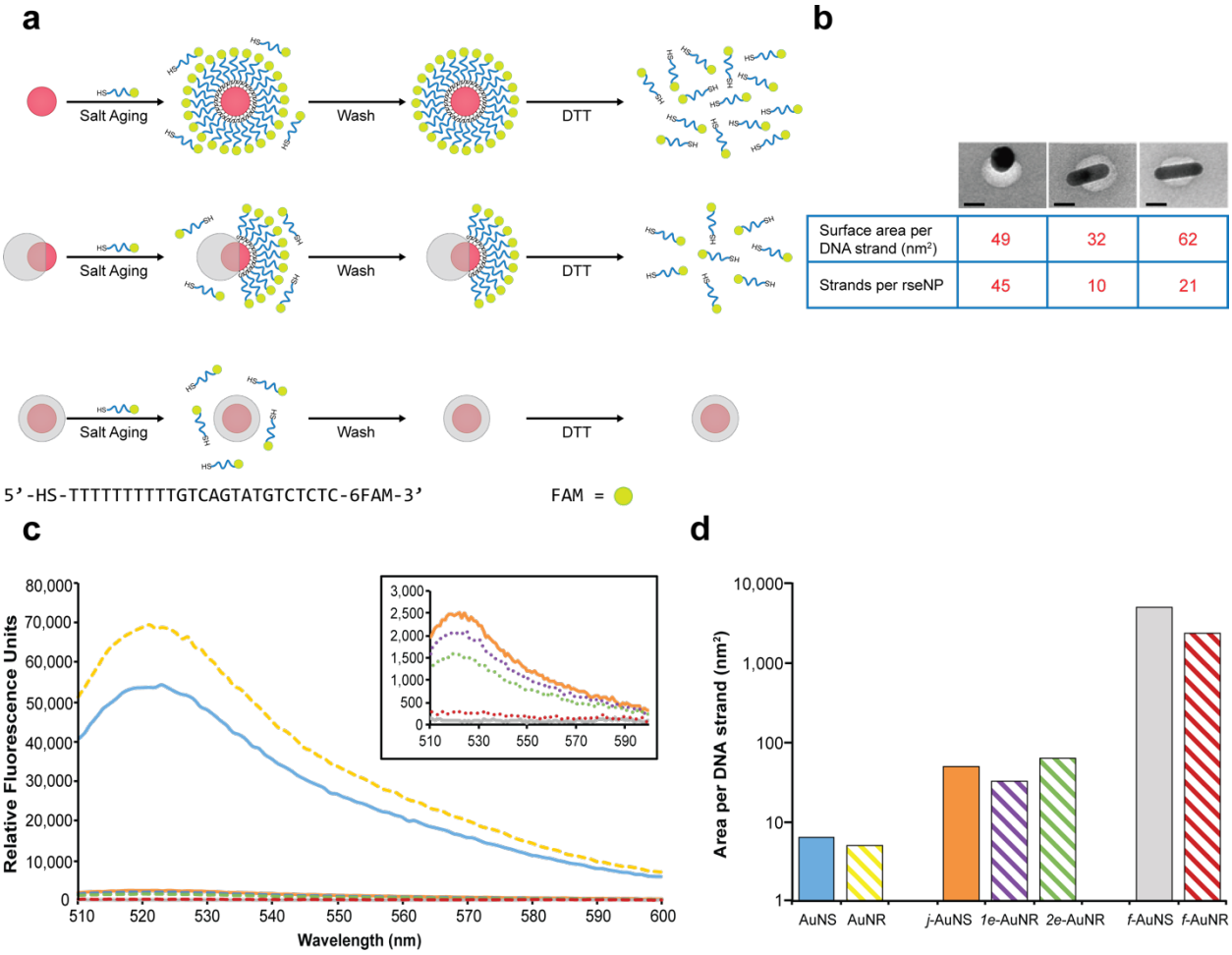

Figure 3.9 DNA loading of bare, partially-encapsulated, and full-encapsulated AuNSs and AuNRs. a) The scheme for the determination of the DNA loading on the surface of bare AuNS, j-AuNS, and f-AuNS. The experiment was also performed on bare AuNR, 1e-AuNR, 2e-AuNR, and f-AuNR. The experimental details are listed below. **b)** The values found for each of the three example partially-encapsulated nanoparticles. The top row shows the average area in nm2 occupied by each DNA strand based on the DNA loading found. The bottom row shows the number of expected DNA strands on the exposed area for the example nanoparticles shown above. Scale bars, 25 nm. **c)** The raw emission spectra overlay from the seven different nanoparticle DNA samples, specifically AuNS-solid blue, AuNR-dotted yellow, j-AuNS-solid orange, 1e-AuNR-dotted purple, 2e-AuNR-dotted green, f-AuNS-solid gray, and f-AuNR-dotted red. The inset shows the samples with lower emission values. **d)** The average area occupied by each DNA strand for each of the seven samples. The colors of the bars correspond to the lines of the spectra in part c. The y-axis is presented in log scale. For comparison, the average area per DNA strand of the fully-encapsulated nanoparticles (right side of the graph) are several thousand square nanometers per strand, which equates to much less than one strand per nanoparticle.

the nanorod counterpart. Our hypothesis regarding this observation led us to compare the relative size of the nanoparticle and the polymer micelle.

The PSPAA polymer micelles became well-studied throughout a series of papers in the late 1990's. This work clearly inspired our predecessors in the nanoparticle encapsulation work as the PSPAA micelles were formed in similar conditions to the ones employed in the encapsulation method. PSPAA was dissolved in DMF and H_2O was slowly added to force the polymer into a spherical micelle[43]. The water content in solution as well as the block lengths and ratios could change the size of the resulting micelle by small amounts[44]. Later on, additives to the solution were also shown to affect the micelle size[45, 46]. Typically, for polymer sizes similar to the one used in our work, the micelle size was typically around 35 nm in diameter. That size compares similarly to the spherical nanoparticles, between 20 and 30 nm, and nanorods, 50 by 15 nm. However, typical bipyramid synthesis yields a length of around 80 nm and a width of 25 nm at the widest point. In addition, the formation of 2-end encapsulated bipyramids indicates the micelle lacks enough size and volume to fully engulf the sides and one full end of the nanoparticle.

We further explored the conditions of the encapsulation by attempting to maximize the micelle size in solution. In accordance with the literature, the addition of acid, raising the DMF/H_2O ratio, or changing the PSPAA block ratios would be the easiest methods to enlarge the micelles formed in solution. We used a polymer where the polystyrene block was increased by a factor of 27% and the polyacrylic acid block was decreased by a factor of 13%, resulting in a micelle size roughly 12% larger according to the formula derived by Eisenberg and Zhang[44], shown below in Equation 3.1. However, the use of any one method or even of all three methods combined, failed to enlarge the micelle to a size that would suitably encapsulate bipyramids of standard synthesis size.

$$R_{core} \propto {N_{PS}}^{0.4} {N_{PAA}}^{-0.15} \qquad \text{(Eq. 3.1)}$$

To further test this hypothesis, we moved to simpler model and one that we had already studied in depth, the gold nanorod. The entirety of the work presented in this chapter as well as in Chapter 5 with regards to gold nanorods used the size 50 x 15 nm, which resulted in consistent and predictable encapuslations. However, to test this hypothesis, nanorods of larger sizes in both

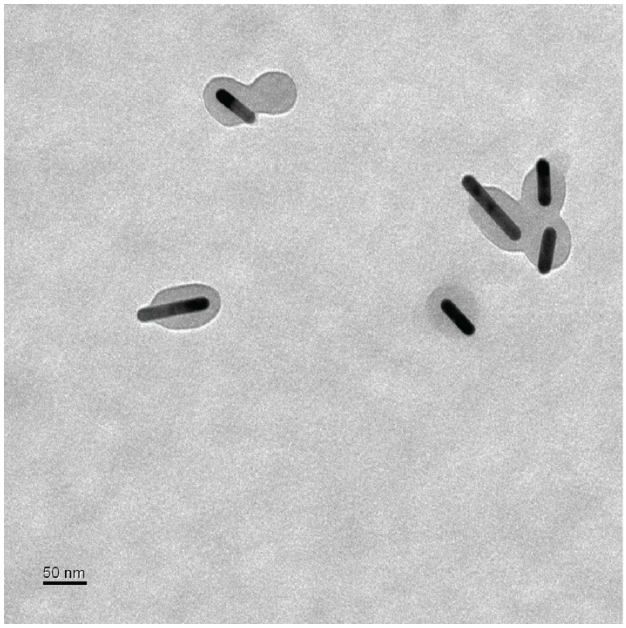

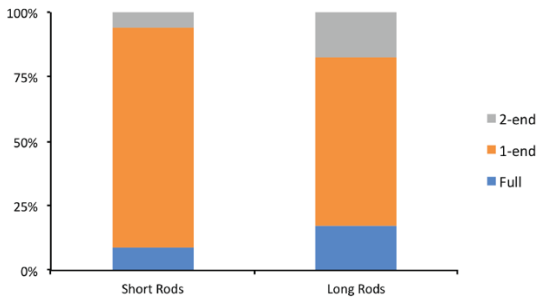

Sample	Length	Width
1	50.8 +/- 5.5	14.2 +/- 1.5
2	104.0 +/- 11.	16.3 +/- 1.6

Figure 3.10 1-end encapsulation of nanorods of varying length. a) TEM image of mixed sample of 1-end encapsulated nanorods showing desired coverage of both long and short nanorods. Scale bar, 50 nm. **b)** Bar graph comparing the relative yields of each encapsulation from the mixed sample of long and short nanorods. **c)** Measurement data for the nanorod samples detailing the lengths of the two samples with widths of very little to negligible difference.

dimensions were synthesized. Specifically, in addition to the nanorods typically used, two sets of longer nanorods and two sets of wider nanorods were employed. Surprisingly, the nanorods with increased length showed possible to encapsulate with one end exposed. However, increased width in the nanorods did not allow for one end exposed. All trials were independently confirmed to encapsulate as well as in the same mixture.

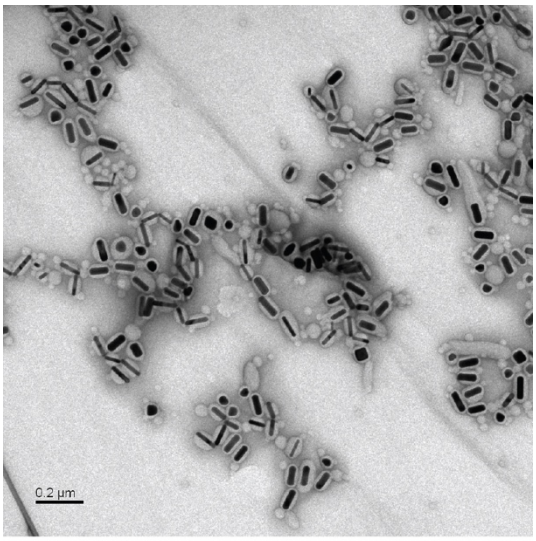

Type	Length	Width
Full	81.5 +/- 9.1	28.4 +/- 4.5
1-end	79.3 +/- 13.8	22.8 +/- 4.0
2-end	87.1 +/- 13.1	18.8 +/- 3.0

Figure 3.11 Encapsulation of nanorods of same length and variable widths. a) TEM image showing sample of mixed nanorods encapsulated with one-end conditions. The percentage of fully-encapsulated and two-end encapsulated nanorods are substantially higher in this sample with the desired one-end product being the lowest percentage constituent. **b)** Table summarizing the dimensions of each encapsulation type. Note that all lengths are within one standard deviation from each other, but the encapsulation type changes with the widths of the nanorods.

These results indicate that the ability to form the eccentric encapsulation may depend on the volume of the nanoparticle that needs to be encapsulated. The volume increase of nanorods increasing only along the long axis scales proportionally, while a change to the radius of the nanorod scales the volume with the square of the radius. While this result offers no insight into a solution to one-end encapsulation of bipyramids, it offers hope for eventually discovering a result. This could presumably be achieved with either smaller bipyramids or further enlarging the polymer micelle with either a longer polystyrene portion or a shorter polyacrylic acid portion.

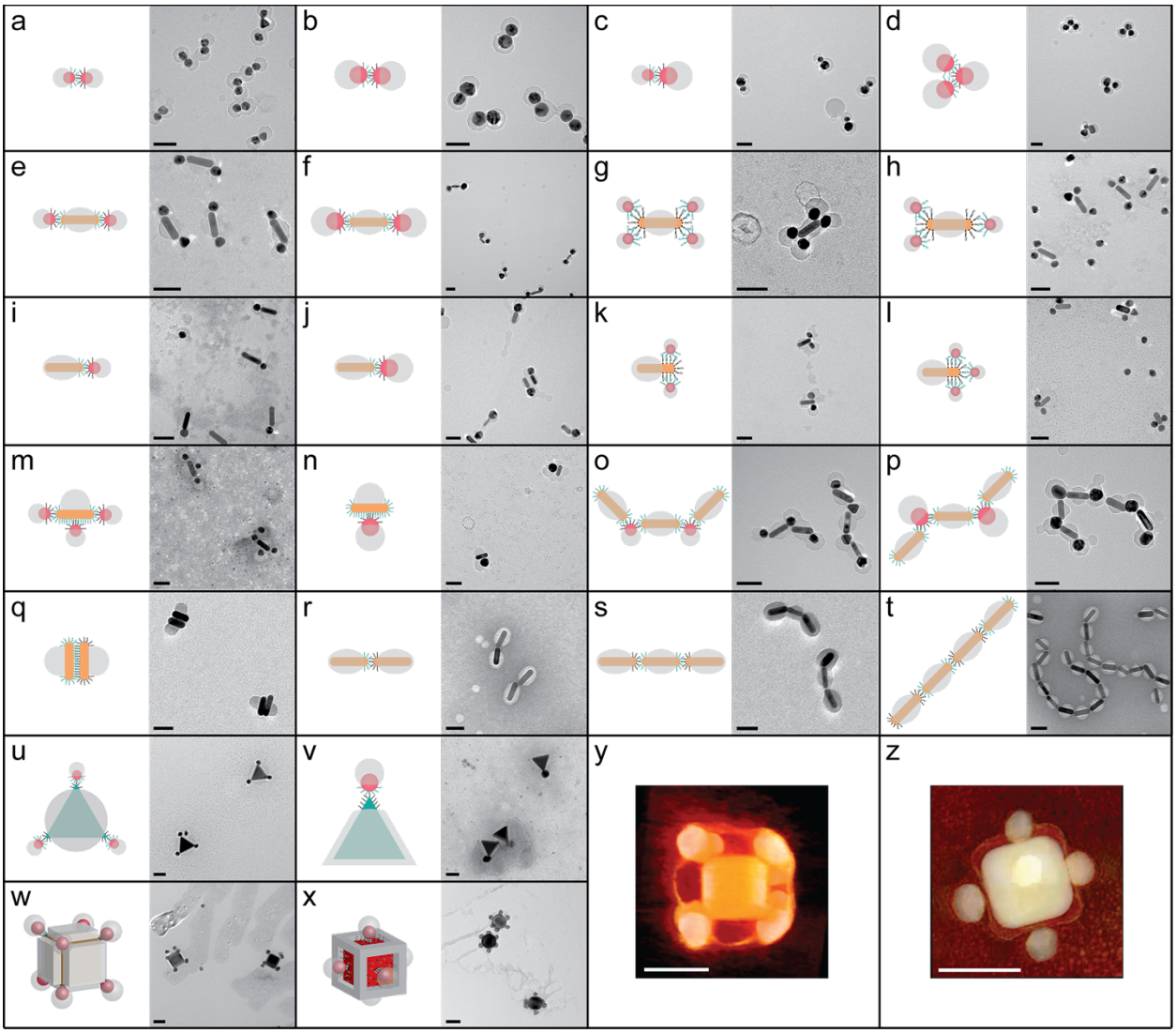

Figure 3.12 Programmable self-assemblies built from rseNPs. a-x) Schemes and corresponding TEM images of the self-assembled structures from the combination of rseNPs listed in Figure 3.1. If it is not specified, each binding site on rseNPs binds only to one complementary rseNPs. In d, g, h, k, l, o, p, NPs with larger polymer-free surface region are used, so more than one complementary rseNPs would bind to the same region. **y, z** show tomogram reconstruction of self-assembled structures corresponding to w and x, respectively. Scale bar, 50 nm.

3.2.5 Self-assembly of rseNPs

After DNA encoding, rseNPs can self-assemble into preconceived structures dictated by the hybridization of DNA. For example, the combination of 0-D *j*-AuNS with two different core sizes (20 and 30 nm) permits three kinds of discrete dimer nanoassemblies: 20-20, 30-30 and 20-

30 (Figure 3.12, a-c). NPs only bound each other via polymer-free surface regions to form dimers with high uniformity, while the surface with polymer attachment had been successfully blocked from binding. The formation of 20-30 heterodimers (Figure 3.12c), without any 20-20 or 30-30 dimers, is attributed to the specificity of DNA hybridization.

Control experiments were performed to show the directionality of the interaction was dictated entirely by the encapsulation. The bare particles were functionalized with complementary DNA strands. TEM images and absorbance spectra were collected of the resultant agglomerations upon DNA hybridization. It can be seen in the inset TEM images that only complementary particles bind, meaning no NR-NR or NP-NP or TP-TP binding. In addition, the lack of directionality and specificity of the binding site results in complete coverage of the nanoparticle in the DNA. Upon DNA hybridization, the formation of extended agglomerates is readily apparent, even by absorbance spectroscopy. The broadened and red-shifted peaks in Figure 3.13c and d are often representative of large-scale aggregation or agglomeration, which is confirmed through the TEM images. Additioanlly, to show the specificity of interaction, the encapsulated nanospheres and nanorods with no DNA functionalization step performed were subjected to the same salt conditions employed for the hybridization step. The additive NaCl forces the aggregation of the exposed gold surface. When mixed and subjected to salt treatment, the nanospheres and nanorods show no preference whatsoever for binding to another nanoparticle. Specifically, there is a statistical mixture of nanorod-nanorod, nanorod-nanosphere, and nanosphere-nanosphere (Figure 3.14). Without the surface DNA-functionlized, there is no specificity of interaction between nanoparticles.

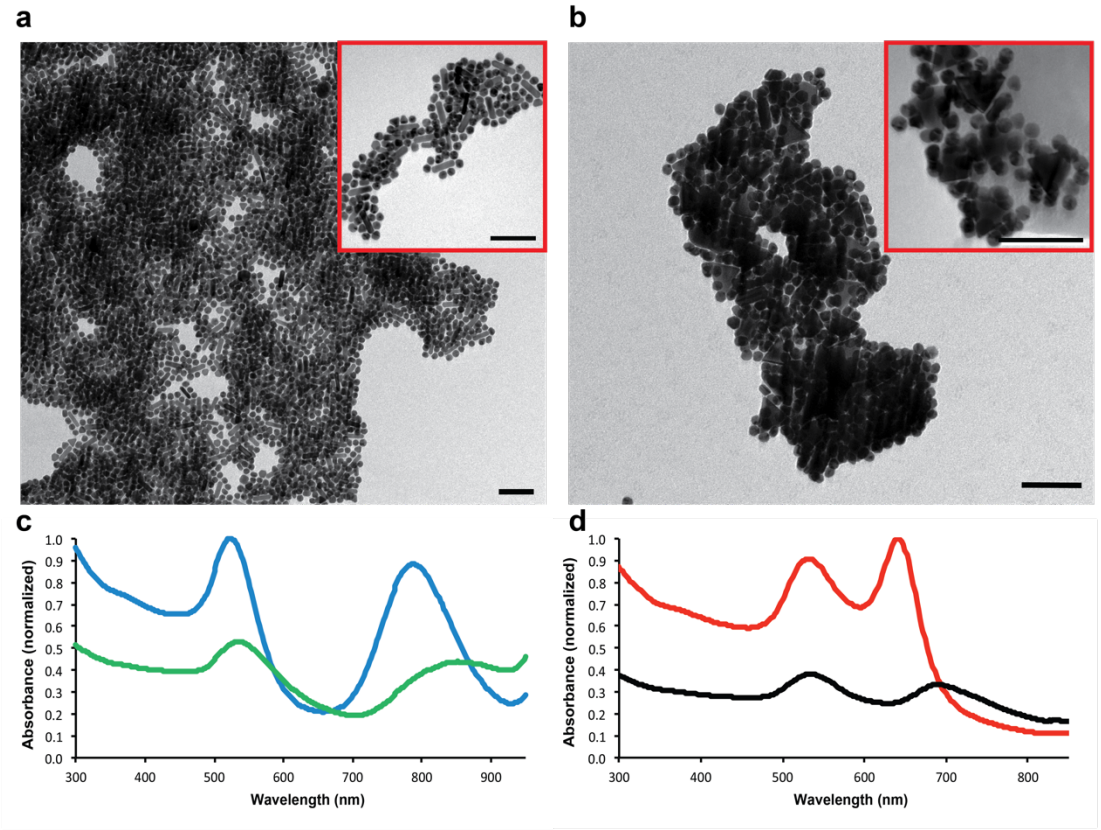

Figure 3.13 | Control experiment showing DNA-mediated binding lacking directionality and specificity of self-assembly for AuNSs, AuNRs, and AuTPs. a) Bare AuNSs functionalized with DNA-1 and bare AuNRs functionalized with DNA-2 were mixed and NaCl was added to make the final concentration 200 mM. After allowing hybridization overnight, TEM images were acquired. Scale bar, 100 nm. **b)** Bare AuNSs functionalized with DNA-1 and bare AuTPs functionalized with DNA-2 were mixed and NaCl was added to make the final concentration 200 mM. After allowing hybridization overnight, TEM images were acquired. Scale bar, 50 nm. **c)** UV-Vis-NIR spectra of the mixed DNA-functionalized AuNRs and AuNSs. The blue line is the normalized curve of the mixture without salt, and the green line is the same sample after salt addition and hybridization, consistent with the agglomeration observed in the TEM images. **d)** UV-Vis-NIR spectra of the mixed DNA-functionalized AuTPs and AuNSs. The red line is the normalized curve of the mixture without salt, and the black line is the same sample after salt addition and hybridization, consistent with the agglomeration observed in the TEM images.

The combination of 0-D (*j*-AuNS) and 1-D (*2e*-AuNR, *1e*-AuNR and *s*-AuNR) rseNPs generated a series of interesting nanoassemblies, such as dumbbell- (Figure 3.12e and 3.12f), exclamation mark- (Figure 3.12i and 3.12j), and pearl necklace-like (Figure 3.12o and 3.12p) structures. Similarly, the combination of complementary 1-D rseNPs created side-by-side dimers (Figure 3.12q), end-to-end dimers (Figure 3.12r), end-to-end trimers (Figure 3.12s) and chain-like

linear oligomers (Figure 3.12t). Besides intermolecular DNA hybridization, there are steric and electrostatic interactions between building blocks, so the configurations of the resulted nanoassembly depend not only on the directionality but also on the saturability of the binding

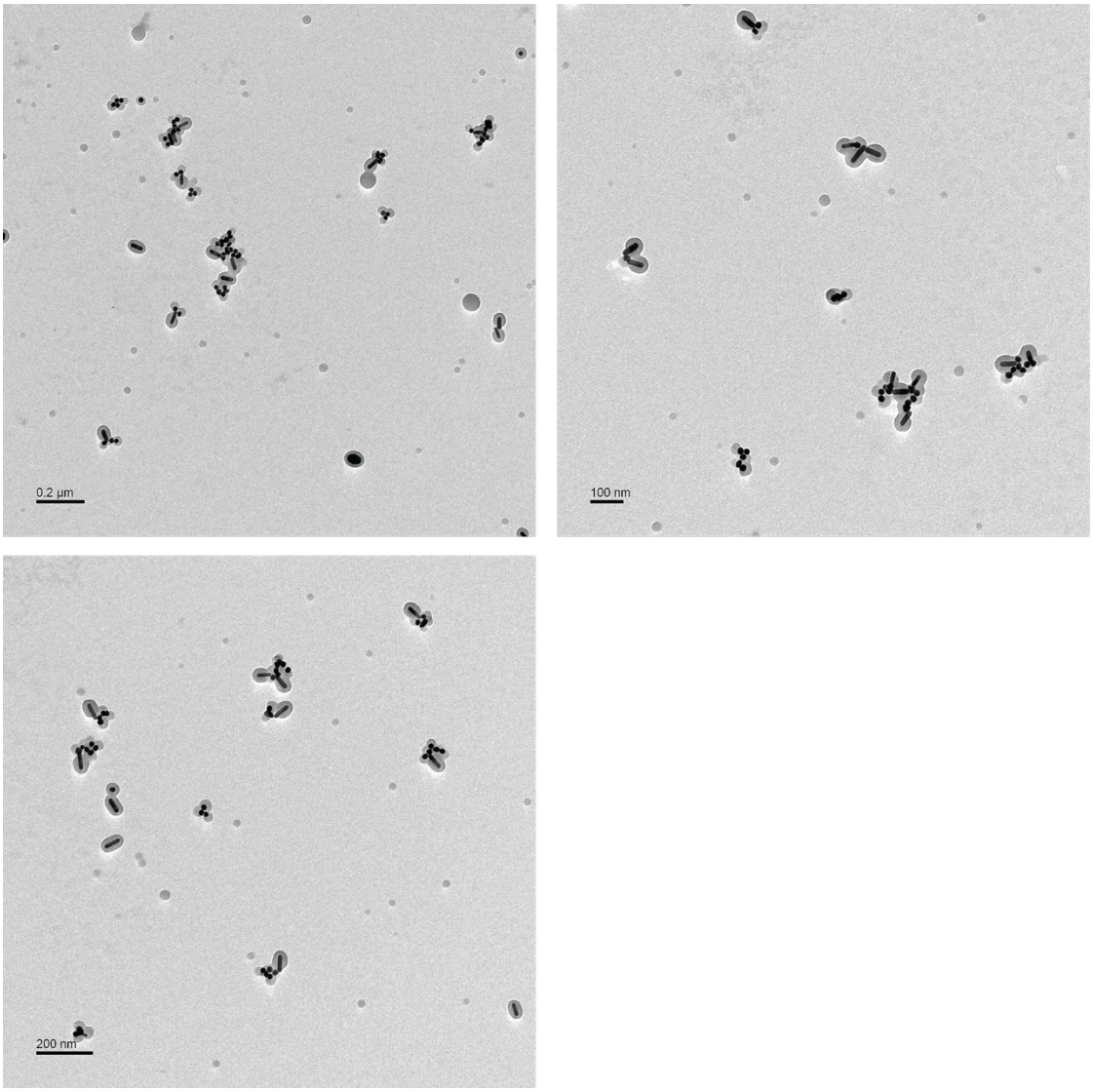

Figure 3.14 | Control experiment using *j*-AuNS and *1e*-AuNR with salt aging and no DNA added. The partially-encapsulated building blocks were exposed to NaCl up to 300 mM with no additional ligands present forcing the aggregation of the exposed surface areas in a non-selective manner. Note the clusters of AuNSs, tip-to-tip AuNRs, and heterostructures present in same sample, indicating that NaCl addition without complementary DNA present causes only a statistical assembly of the building blocks, as opposed to the 1e-AuNR and j-AuNS assembly shown in Figure 3.12i.

region on rseNPs. Small binding regions favor individual linking, and large binding regions permit the linking to multiple complementary rseNPs. For example, when complementary 0-D *j*-AuNS and 1-D *2e*-AuNR were mixed together, the *j*-AuNSs with a small binding region can bind to a single *2e*-AuNR to form dumbbell-like structures (Figure 3.12e and 3.12f) due to the steric effect. However, with a larger binding region, each *j*-AuNS binds more than one *2e*-AuNR to generate a pearl necklace-like structures (Figure 3.12o and 3.12p). Likewise, the 1-D rseNPs with large

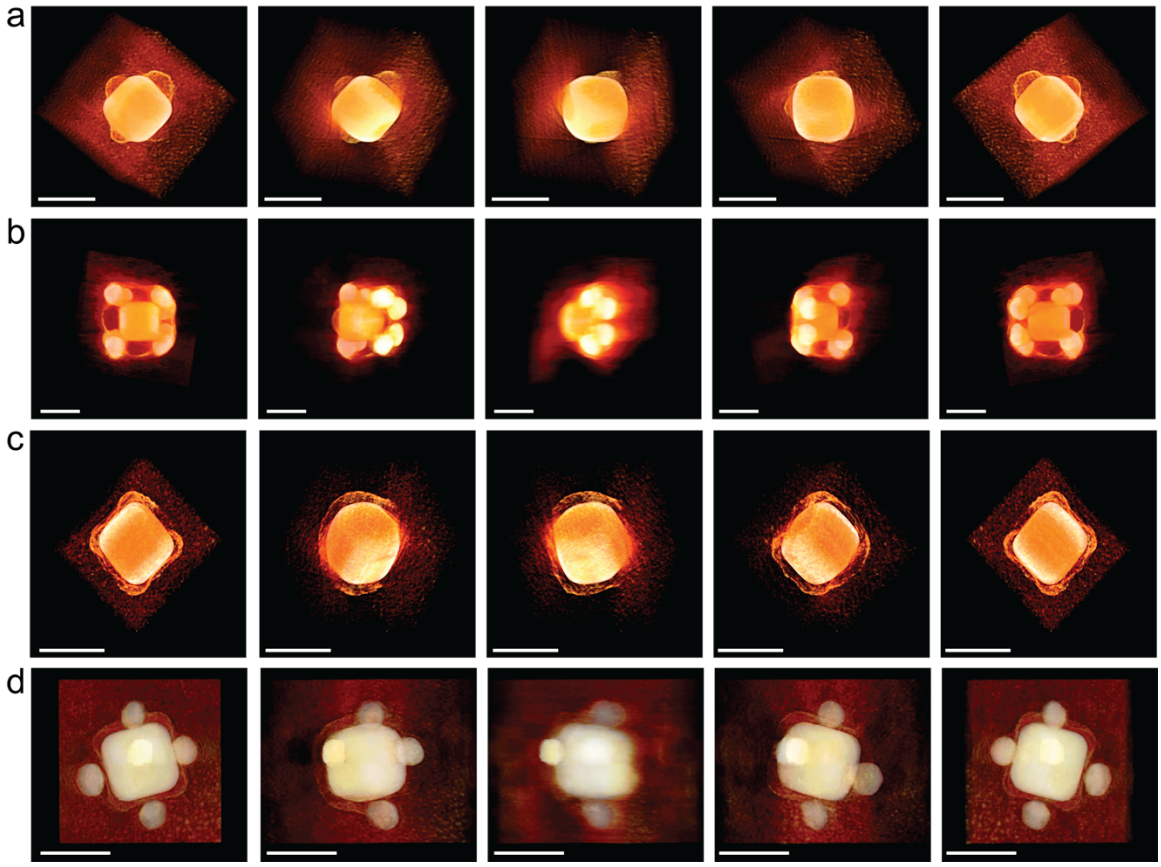

Figure 3.15 Snapshots from 3-D tomography movies showing various rotational angles of AuNC encapsulated building blocks and self-assemblies This figure shows snapshots from the movies of the **a)** v-AuNC, **b)** v-AuNC self-assembly with 20 nm AuNS, **c)** c-AuNC, and **d)** c-AuNC self-assembly with 20 nm AuNS. Each snapshot is a 45-degree rotation from the previous. All scale bars 50 nm.

binding region have enough space to bind with more than one 0-D rseNPs (Figure 3.12g, 3.12h, 3.12k and 3.12l).

In the mixture of complementary 0-D and 2-D rseNPs, *j*-AuNS selectively bound to the polymer-free vertices of *v*-AuTP to form starfish-like or snowman-like nanoassemblies (Figure 3.12u and 3.12v). When the 0-D and 3-D rseNPs were mixed, *j*-AuNS bound only to the center of *c*-AuNC (Figure 3.12x and 3.12d), but the vertices of *v*-AuNC (Figure 3.12w and 3.12b), as

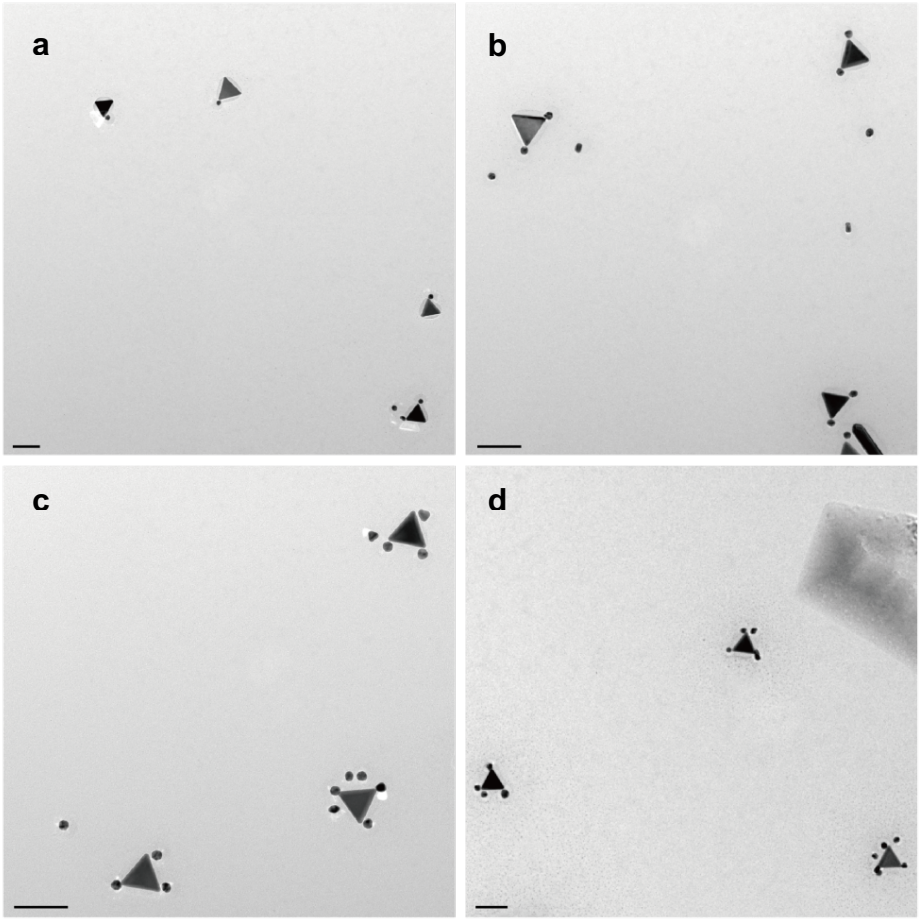

Figure 3.16 Dependence of the nanoassembly of *j*-20AuNS-1 and 3*v*-AuTP on salt concentration TEM images of nanoassembly at different NaCl concentrations: (a), 50; (b), 100; **(c)**, 150; **(d)**, 200 mM. In order to increase the collision frequency of the rseNPs, and therefore increase the chance of ssDNA hybridization and therefore self-assembly, it is necessary to reduce the magnitude of the repulsive interparticle forces that exist between them. Scale bars, 100 nm.

observed by tomography. Furthermore, since the rseNPs are highly negatively charged, the electrostatic interaction should be considered. The Debye screening length, which influences the effective collision between the rseNPs, can be tuned with the ionic

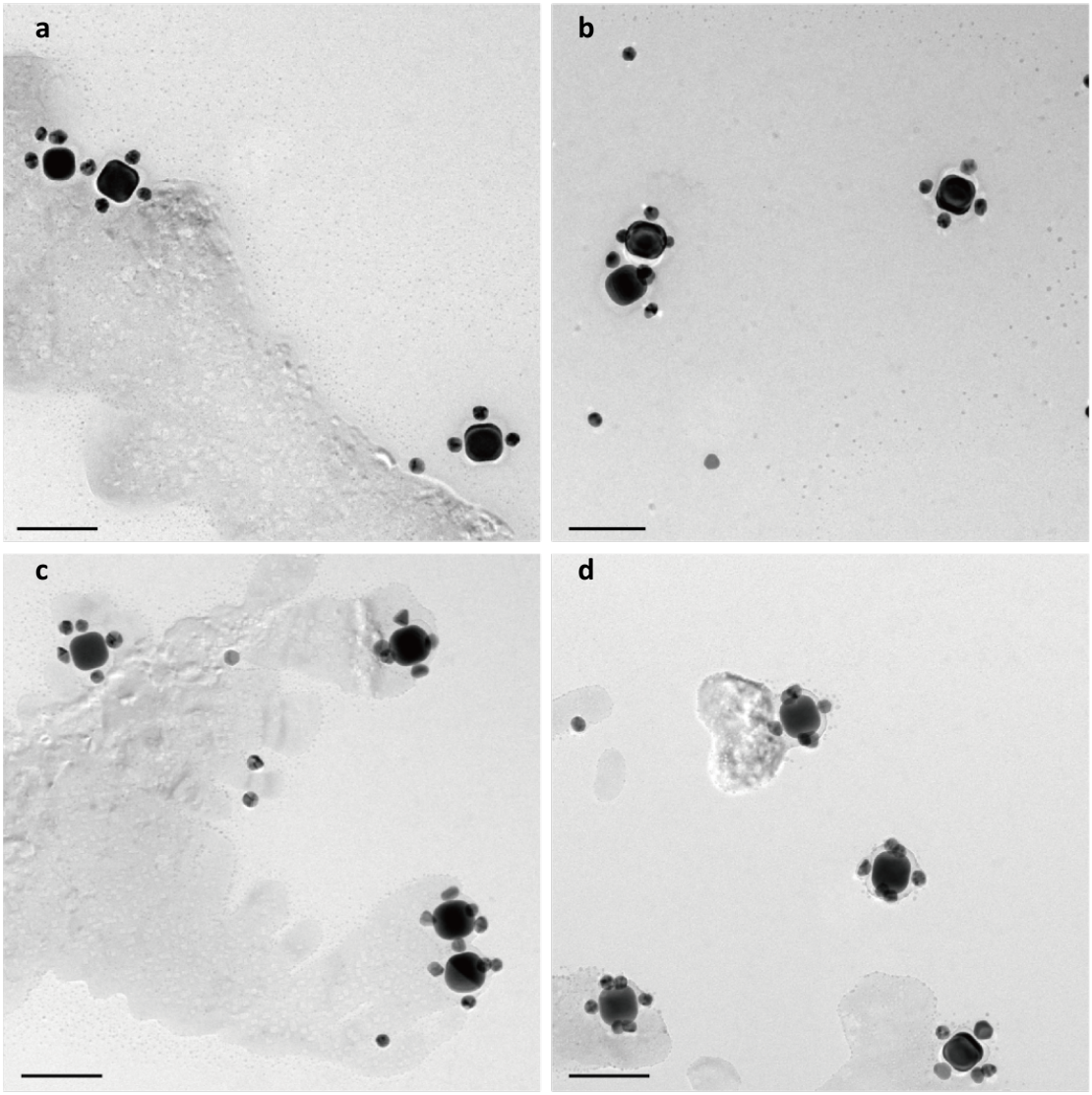

Figure 3.17 Dependence of nanoassembly of *j*-20AuNS-1 and *c*-AuNC on salt concentration TEM images of nanoassembly at different NaCl concentrations: (a), 200; (b)**,** 300; (c), 400; (d)**,** 500 mM. Similar to the nanoassembly of j-20AuNS-1 and 3v-AuTP, an increase in the ionic strength of the medium leads to an increase of the number of j-20AuNS-1 binding to the facet center of c-AuNC. Scale bar, 100 nm.

strength (salt concentration) in the solution[47] (Figures 3.16 and 3.17). The larger the NP, the higher the salt concentration required for self-assembly. For example, with the increase of salt concentration, more j-AuNS bound to the polymer-free surface regions of AuTP and AuNC, until the centric structures were saturated (Figures 3.16 and 3.17).

3.2.6 Conclusions

We have developed here a new strategy for regiospecific surface encoding of colloidal NPs through polymer blocking and subsequent DNA modification. The coverage of the diblock copolymer on the NP surface can be empirically controlled by modifying the ligand ratio as well as the solvent ratio during encapsulation. The change in the ligand ratio leads to adjustments of surface energies of NPs, while the solvent ratio influences the micelle formation of copolymer on NPs surface. After blocking, the polymer-free surface regions of NPs are accessible for ssDNA modification, thus enabling regiospecific surface encoding. This two-step process successfully converts the NPs into rseNPs with a high yield. The location and size of the polymer-free surface regions assure directionality and saturability of the interactions between different rseNPs, and the sequence-specific hybridization of DNA imparts specificity of these interactions. This is a significant step toward NP building blocks with highly addressable surfaces that allow for the deliberate design and synthesis of sophisticated self-assembled nanostructures. The ability to control the binding directionality and specificity on colloidal NPs opens a wide spectrum of new structures for self-assembly of NPs. With our strategy, more rseNPs are expected from NPs with other anisotropic shapes, including tetrahedra, pentagonal prisms, and hexagonal prisms, as well as those of other materials, such as quantum dots, magnetic nanoparticles, and metal oxides. With the various rseNPs, many nanoassemblies that have proven difficult or impossible to make with existing colloidal NPs may be accessible for the first time.

3.3 Methods

3.3.1 Polymer encapsulation of gold nanosphere (AuNS)

The encapsulation was carried out according to the procedure from a previously reported paper with minor modifications[37]. For full encapsulation, citrate stabilized AuNSs (19.8 ± 1.3 nm, 1.5 mL) solution was centrifuged to a volume of ~15 μL using 12500 g for 15 min. The deep red solution collected was then diluted by water to a final volume of 188 μL, which was added into the mixture of 602 μL DMF and 150 μL DMF solution of PS_{144}-b-PAA_{22} (0.25 mM in DMF). Then L_A (60 μL, 2.74 mM in EtOH) was finally added to the reaction mixture giving a total volume of 1.0 mL. The final concentrations of the species are listed in Supplementary Table 1. The mixture was heated at 105 °C for 1.5 hour, and removed from oil bath to cool down at room temperature. Microwave reaction vials (2-5 mL) sealed with aluminum caps were used in the heating process to prevent the leaking of the mixture by evaporation. A similar procedure was used for the partial encapsulation, where different amount of L_B (100 mM in H_2O) was added to the reaction mixture before the addition of L_A.

3.3.2 Polymer encapsulation of gold nanorods (AuNR)

AuNR were prepared using the silver-assisted growth procedure developed by El-Sayed and coworkers[48], with the aspect ratio 3.9 (L=54.3 ± 3.4 nm, W=14.1 ± 1.1 nm. The synthesized AuNRs were spun down (10 min, 10, 000 g) once and resuspended in H_2O, followed by a second centrifugation, and resuspended in 1mM CTAB with the final concentration of 0.2 nM. AuNRs concentration was quantified using optical extinction spectra and the absorbance value at the longitudinal surface plasmon resonance (LSPR) maximum. An extinction coefficient of 4.6×10^9 $M^{-1}cm^{-1}$ [49] was used to estimate concentration. 1.0 mL of AuNRs solution was concentrated to 15 μL by centrifugation and then diluted by water to a final volume of 209 μL, which was added into

the mixture of 581 μL DMF and 150 μL DMF solution of PS_{144}-b-PAA_{22} (0.25 mM in DMF). Then L_A (60 μL, 2.74 mM in EtOH) were finally added to the reaction mixture giving a total volume of 1.0 mL. The mixture was heated at 105 °C for 1.5 hour, and removed from oil bath to cool down at room temperature. A similar procedure was used for the partial encapsulation, where 4 μL of L_B (100 mM in H_2O) was added to the reaction mixture before the addition of L_A to create 2*e*-AuNR-1. The various *e*-AuNRs were created through tuning the ratio of DMF to H_2O and ratio of L_A to L_B in the solvent mixture, as listed in Table 3.1.

3.3.3 Polymer encapsulation of gold triangular nanoprisms (AuTPs) and gold nanocubes (AuNCs)

AuTP and AuNC were synthesized according to Scarabelli et al.[50] and Kou et al.[51], respectively. Before encapsulation, the AuTP of small size was isolated from the as-synthesized mixture of AuNS, pentagonal pyramids, small and large AuTP by depletion flocculation[11,52], which is described below. After purification, the concentration of AuTP was quantified using optical extinction spectra and the absorbance value at the maximal surface plasmon resonance (LSPR). An extinction coefficient of 2.4×10^{10} $M^{-1}cm^{-1}$ was used for AuTP with the edge length of 72.7 ±10.6 nm. 1.0 mL solution of purified AuTP (0.06 nM) was spun down (10 min, 6000 g) once and resuspended in 1 mL of CTAB (1 mM), followed by a second centrifugation to concentrate it into 15uL for the following polymer encapsulation. To determine the concentration of AuNC in the as-synthesized solution, an extinction coefficient of 8.6×10^{9} $M^{-1}cm^{-1}$ [53] was used for AuNC with the edge length of 44.4 ± 2.6 nm. 1.0 mL of as-synthesized AuNC solution (0.03 nM) was spun down (10min, 6000g) twice and resuspended in 1 mM CTAB with the final volume of 15 μL. The polymer encapsulation was carried out according to the procedure on AuNR with minor

modifications to the solvent ratios and ligand amounts and identities, and the detailed experimental conditions are listed in Table 3.1.

3.3.4 Preparation of TEM Samples

150 μL of as-prepared polymer encapsulated NPs solution was diluted by 10 times with SDS (0.01%) and centrifuged twice to remove empty polymer micelle and excess reactants, giving a final volume of 15 μL. $(NH_4)_6Mo_7O_{24}$ was used as the negative stain so that the polymer shells appear white against the stained background. TEM grids were treated with glow discharge for 30 sec to improve the surface hydrophilicity. 4 μL of purified sample solution was carefully mixed with 2 μL of stain solution ($(NH_4)_6Mo_7O_{24}$, 8.6 mM) and then deposited onto the hydrophilic face of the TEM grid, after which filter paper was used to remove excess solution on the TEM grid. The grid was as then dried in vaccuum for 1 hour before analysis.

3.3.5 Functionalization of polymer partially blocked NPs with selected DNA strands

To 45 μL of 100 μM thiolated DNA in TE buffer, 5 μL of 10 mM TCEP in TE buffer was added and mixed. The mixture was shaken at room temperature for 2 hours and then purified by Nanosep centricon (3K) to remove excess TCEP and the cleaved residue with thiol group. 150 μL of as-prepared partially blocked NPs was diluted by 10 times with SDS (0.01%) and centrifuged twice to remove empty polymer micelle and excess reactants, and the pellet was dispersed into 20 μL Tris-HCl buffer (pH=8) with SDS (0.01%). 10 μL of purified thiol-DNA solution was added to 20 μL purified NP solution and allowed to react for 2 hours. The mixture of thiolated-DNA and NP solution was then treated with a modified salt-aging procedure to allow for electrostatic screening between neighboring DNA strands, and allowing for greater saturation of DNA on the surface. Specifically, solutions were brought to 0.05 M, 0.1 M, 0.2 M, 0.3 M, 0.4 M, and 0.5 M NaCl sequentially with approximately 30 min between each addition of salt solution (1M NaCl,

pH=8 Tris-HCl, 0.01% SDS). After the increase in salt concentration was complete, NPs were left overnight to maximize the loading of DNA. In order to remove unbound DNA from solution, particle suspensions were centrifuged, the supernatant was removed, and the pellet was re-suspended in Tris-HCl buffer (pH=8) with 0.01% SDS three times. The final suspension was concentrated to 30 μL to allow for a concentrated solution of NPs.

3.3.6 Determination of DNA loading

The experimental procedure was based on a report from the Mirkin group in 2007. In detail, seven samples were analyzed for DNA loading: bare AuNSs, *j*-AuNSs, *f*-AuNSs, bare NRs, *1e*-AuNR, *2e*-AuNR, and *f*-AuNR. DNA was purchased from IDT with a 3'-functionalized FAM fluorophore and the 5'-thiol linker present on all other DNA strands used in this project. The DNA was cleaved using 0.1M DTT and purified from the excess using a NAP-5 column, as presented in section 3.3.5. All samples, once purified from other materials using centrifugation, were concentrated to 25 μL and subjected to treatment of 25 μL of the cleaved and purified FAM-DNA. The salt aging of the DNA-nanoparticle mixture was carried out as per the Methods. After allowing the solution to shake overnight at room temperature, the solutions were purified from the excess DNA by centrifugation 5 times at 10,000 *g* for 10 min. Once cleaned from the excess DNA, 50 μL of a 0.1 M DTT solution was added to each sample to cleave the DNA from the surface of the nanoparticles, which was then allowed to shake overnight at room temperature. Then each sample was centrifuged at 12,000 *g* for 15 mins to remove all the nanoparticles from solution, leaving the cleaved DNA in the supernatant. All the supernatant was then collected, and the fluorescence of each was measured using the ELYSA plate reader (excitation: 490 nm, emission: 508 nm to 600 nm at 1 nm resolution). The peak emission spectrum was then recorded, each reading at approximately 525 nm. A control experiment of the FAM-DNA was performed to create a Beer's

Law plot by treating the DNA identical to the nanoparticle trials, including the salt aging and DTT treatment, before measuring the emission spectra at varying concentrations. Extinction coefficients were used to calculate the AuNS and AuNR concentrations, and the extinction coefficient of 239800 L mol^{-1} cm^{-1} was used to estimate the concentration of the DNA. The fluorescence values for each nanoparticle sample were then used along with the Beer's Law formula to determine the DNA concentration. When compared to the nanoparticle concentrations, a loading density for each could be determined. For comparison, the bare AuNS was well within reason to what Mirkin's group measured for similar size spheres (citation) and the AuNRs, which they did not measure at the time, also have a similar loading density. The fully-encapsulated nanoparticles, which serve as a control, show no signs of fluorescence, confirming that the polymer prevents any binding of the thiolated DNA to the surface of the nanoparticle, and that the functionalization and washing steps completely remove any residual DNA from the solutions. Although the fluorescence peaks of the partially-encapsulated nanoparticles appear to be much less than their corresponding bare nanoparticles, that can be explained by a low exposed surface area (only ~10-40% of the surface area is exposed from the partial encapsulation) and the lower packing density, which we believe to be due to incomplete ligand exchange, despite the salt aging procedure.

3.3.7 Assembly of rseNPs

10 μL of each rseNPs with complementary DNA strands were mixed with 10 μL Tris-HCl buffer (pH=8, 0.01% SDS) with different salt concentrations and incubated at room temperature overnight. 25 μL of assembly sample was employed for UV-Vis absorbance measurement and 5 μL was used to prepare the TEM grid. To achieve best performance, the grids were treated with glow discharge to increase their hydrophilicity.

3.3.8 Electron Microscopy Tomography

The electron tomography tilt series were acquired in a thermionic TEM operated at 120 keV. Bright-field TEM images were acquired from -70 degrees to +70 degrees with 2-degree intervals. The electron dose was controlled to be less than 200 electrons/$Å^2$ for a full tilt series. No obvious polymeric mass loss, contraction, or dilation was observed under this dose condition. The 3-D tomograms were reconstructed using a standard filtered back projection method implemented by a custom written code in Matlab and visualized by Avizo.

3.4 References

1. Xia Y, Xiong Y, Lim B, Skrabalak SE. Shape-Controlled Synthesis of Metal Nanocrystals: Simple Chemistry Meets Complex Physics? *Angewandte Chemie-International Edition* 2009, **48**(1)**:** 60-103.

2. Huang X, Neretina S, El-Sayed MA. Gold Nanorods: From Synthesis and Properties to Biological and Biomedical Applications. *Advanced Materials* 2009, **21**(48)**:** 4880-4910.

3. Prodan E, Radloff C, Halas NJ, Nordlander P. A Hybridization Model for the Plasmon Response of Complex Nanostructures. *Science* 2003, **302**(5644)**:** 419-422.

4. Sun YG, Xia YN. Shape-controlled synthesis of gold and silver nanoparticles. *Science* 2002, **298**(5601)**:** 2176-2179.

5. Xia YN, Yang PD, Sun YG, Wu YY, Mayers B, Gates B, *et al*. One-dimensional nanostructures: Synthesis, characterization, and applications. *Advanced Materials* 2003, **15**(5)**:** 353-389.

6. Langille MR, Zhang J, Personick ML, Li S, Mirkin CA. Stepwise Evolution of Spherical Seeds into 20-Fold Twinned Icosahedra. *Science* 2012, **337**(6097)**:** 954-957.

7. Jin RC, Cao YC, Hao EC, Metraux GS, Schatz GC, Mirkin CA. Controlling anisotropic nanoparticle growth through plasmon excitation. *Nature* 2003, **425**(6957)**:** 487-490.

8. Zhu M, Aikens CM, Hollander FJ, Schatz GC, Jin R. Correlating the crystal structure of A thiol-protected Au-25 cluster and optical properties. *Journal of the American Chemical Society* 2008, **130**(18)**:** 5883-5884.

9. Alivisatos AP, Johnsson KP, Peng X, Wilson TE, Loweth CJ, Bruchez Jr MP, *et al*. Organization of'nanocrystal molecules' using DNA. *Nature* 1996, **382**(6592)**:** 609-611.

10. Sun SH, Zeng H. Size-controlled synthesis of magnetite nanoparticles. *Journal of the American Chemical Society* 2002, **124**(28)**:** 8204-8205.

11. Lee J-H, Gibson KJ, Chen G, Weizmann Y. Bipyramid-templated synthesis of monodisperse anisotropic gold nanocrystals. *Nature Communications* 2015, **6**.

12. Nie Z, Petukhova A, Kumacheva E. Properties and emerging applications of self-assembled structures made from inorganic nanoparticles. *Nat Nanotechnol* 2010, **5**(1)**:** 15-25.

13. Li F, Josephson DP, Stein A. Colloidal assembly: the road from particles to colloidal molecules and crystals. *Angew Chem Int Ed Engl* 2011, **50**(2)**:** 360-388.

14. Kuzyk A, Schreiber R, Fan Z, Pardatscher G, Roller EM, Hogele A, *et al*. DNA-based self-assembly of chiral plasmonic nanostructures with tailored optical response. *Nature* 2012, **483**(7389)**:** 311-314.

15. Park SY, Lytton-Jean AKR, Lee B, Weigand S, Schatz GC, Mirkin CA. DNA-programmable nanoparticle crystallization. *Nature* 2008, **451**(7178)**:** 553-556.

16. Shevchenko EV, Talapin DV, Kotov NA, O'Brien S, Murray CB. Structural diversity in binary nanoparticle superlattices. *Nature* 2006, **439**(7072)**:** 55-59.

17. Whitesides GM, Grzybowski B. Self-assembly at all scales. *Science* 2002, **295**(5564)**:** 2418-2421.

18. Nykypanchuk D, Maye MM, van der Lelie D, Gang O. DNA-guided crystallization of colloidal nanoparticles. *Nature* 2008, **451**(7178)**:** 549-552.

19. Singh G, Chan H, Baskin A, Gelman E, Repnin N, Kral P, *et al*. Self-assembly of magnetite nanocubes into helical superstructures. *Science* 2014, **345**(6201)**:** 1149-1153.

20. Alivisatos AP, Johnsson KP, Peng XG, Wilson TE, Loweth CJ, Bruchez MP, *et al*. Organization of 'nanocrystal molecules' using DNA. *Nature* 1996, **382**(6592)**:** 609-611.

21. Edwardson TGW, Lau KL, Bousmail D, Serpell CJ, Sleiman HF. Transfer of molecular recognition information from DNA nanostructures to gold nanoparticles. *Nature Chemistry* 2016, **8**(2)**:** 162-170.

22. Xu X, Rosi NL, Wang Y, Huo F, Mirkin CA. Asymmetric functionalization of gold nanoparticles with oligonucleotides. *Journal of the American Chemical Society* 2006, **128**(29)**:** 9286-9287.

23. Liu W, Halverson J, Tian Y, Tkachenko AV, Gang O. Self-organized architectures from assorted DNA-framed nanoparticles. *Nat Chem* 2016, **8**(9)**:** 867-873.

24. Liu W, Tagawa M, Xin HL, Wang T, Emamy H, Li H, *et al*. Diamond family of nanoparticle superlattices. *Science* 2016, **351**(6273)**:** 582-586.

25. Shen C, Lan X, Lu X, Meyer TA, Ni W, Ke Y, *et al*. Site-Specific Surface Functionalization of Gold Nanorods Using DNA Origami Clamps. *Journal of the American Chemical Society* 2016, **138**(6)**:** 1764-1767.

26. Walther A, Mueller AHE. Janus Particles: Synthesis, Self-Assembly, Physical Properties, and Applications. *Chemical Reviews* 2013, **113**(7)**:** 5194-5261.

27. Maye MM, Nykypanchuk D, Cuisinier M, van der Lelie D, Gang O. Stepwise surface encoding for high-throughput assembly of nanoclusters. *Nature Materials* 2009, **8**(5)**:** 388-391.

28. Pan Y, Gao JH, Zhang B, Zhang XX, Xu B. Colloidosome-based Synthesis of a Multifunctional Nanostructure of Silver and Hollow Iron Oxide Nanoparticles. *Langmuir* 2010, **26**(6)**:** 4184-4187.

29. Chen Q, Whitmer JK, Jiang S, Bae SC, Luijten E, Granick S. Supracolloidal Reaction Kinetics of Janus Spheres. *Science* 2011, **331**(6014)**:** 199-202.

30. Xing H, Wang Z, Xu Z, Wong NY, Xiang Y, Liu GL, *et al*. DNA-Directed Assembly of Asymmetric Nanoclusters Using Janus Nanoparticles. *Acs Nano* 2012, **6**(1)**:** 802-809.

31. Wang F, Cheng S, Bao Z, Wang J. Anisotropic Overgrowth of Metal Heterostructures Induced by a Site-Selective Silica Coating. *Angewandte Chemie-International Edition* 2013, **52**(39)**:** 10344-10348.

32. Chen T, Wang H, Chen G, Wang Y, Feng Y, Teo WS, *et al*. Hotspot-induced transformation of surface-enhanced Raman scattering fingerprints. *Acs Nano* 2010, **4**(6)**:** 3087-3094.

33. Li YL, Liu ZY, Yu GM, Jiang W, Mao CD. Self-Assembly of Molecule-like Nanoparticle Clusters Directed by DNA Nanocages. *Journal of the American Chemical Society* 2015, **137**(13)**:** 4320-4323.

34. Liu K, Nie Z, Zhao N, Li W, Rubinstein M, Kumacheva E. Step-Growth Polymerization of Inorganic Nanoparticles. *Science* 2010, **329**(5988)**:** 197-200.

35. Walker DA, Leitsch EK, Nap RJ, Szleifer I, Grzybowski BA. Geometric curvature controls the chemical patchiness and self-assembly of nanoparticles. *Nature Nanotechnology* 2013, **8**(9)**:** 676-681.

36. Choueiri RM, Galati E, Thérien-Aubin H, Klinkova A, Larin EM, Querejeta-Fernández A, *et al*. Surface patterning of nanoparticles with polymer patches. *Nature* 2016, **538:** 79.

37. Chen T, Yang M, Wang X, Tan LH, Chen H. Controlled assembly of eccentrically encapsulated gold nanoparticles. *Journal of the American Chemical Society* 2008, **130**(36)**:** 11858-11859.

38. Torza S, Mason SG. Three-phase interactions in shear and electrical fields. *Journal of Colloid and Interface Science* 1970, **33**(1)**:** 67-83.

39. Love JC, Estroff LA, Kriebel JK, Nuzzo RG, Whitesides GM. Self-Assembled Monolayers of Thiolates on Metals as a Form of Nanotechnology. *Chemical Reviews* 2005, **105**(4)**:** 1103-1170.

40. Zhang L, Eisenberg A. Morphogenic Effect of Added Ions on Crew-Cut Aggregates of Polystyrene-b-poly(acrylic acid) Block Copolymers in Solutions. *Macromolecules* 1996, **29**(27)**:** 8805-8815.

41. Hurst SJ, Lytton-Jean AKR, Mirkin CA. Maximizing DNA Loading on a Range of Gold Nanoparticle Sizes. *Analytical chemistry* 2006, **78**(24)**:** 8313-8318.

42. Liu M, Guyot-Sionnest P, Lee TW, Gray SK. Optical properties of rodlike and bipyramidal gold nanoparticles from three-dimensional computations. *Physical Review B - Condensed Matter and Materials Physics* 2007, **76**(23).

43. Zhang L, Eisenberg A. Multiple morphologies of" crew-cut" aggregates of polystyrene-b-poly (acrylic acid) block copolymers. *Science* 1995, **268**(5218)**:** 1728-1731.

44. Zhang L, Eisenberg A. Multiple morphologies and characteristics of “crew-cut” micelle-like aggregates of polystyrene-b-poly (acrylic acid) diblock copolymers in aqueous solutions. *Journal of the American Chemical Society* 1996, **118**(13)**:** 3168-3181.

45. Zhang L, Yu K, Eisenberg A. Ion-induced morphological changes in “crew-cut” aggregates of amphiphilic block copolymers. *Science* 1996, **272**(5269)**:** 1777-1779.

46. Yu Y, Zhang L, Eisenberg A. Morphogenic effect of solvent on crew-cut aggregates of apmphiphilic diblock copolymers. *Macromolecules* 1998, **31**(4)**:** 1144-1154.

47. Yang M, Chen G, Zhao Y, Silber G, Wang Y, Xing S*, et al*. Mechanistic investigation into the spontaneous linear assembly of gold nanospheres. *Physical Chemistry Chemical Physics* 2010, **12**(38)**:** 11850-11860.

48. Nikoobakht B, El-Sayed MA. Preparation and Growth Mechanism of Gold Nanorods (NRs) Using Seed-Mediated Growth Method. *Chemistry of Materials* 2003, **15**(10)**:** 1957-1962.

49. Orendorff CJ, Murphy CJ. Quantitation of Metal Content in the Silver-Assisted Growth of Gold Nanorods. *The Journal of Physical Chemistry B* 2006, **110**(9)**:** 3990-3994.

50. Scarabelli L, Coronado-Puchau M, Giner-Casares JJ, Langer J, Liz-Marzán LM. Monodisperse Gold Nanotriangles: Size Control, Large-Scale Self-Assembly, and Performance in Surface-Enhanced Raman Scattering. *ACS Nano* 2014, **8**(6)**:** 5833-5842.

51. Kou X, Sun Z, Yang Z, Chen H, Wang J. Curvature-Directed Assembly of Gold Nanocubes, Nanobranches, and Nanospheres. *Langmuir* 2009, **25**(3)**:** 1692-1698.

52. Park K, Koerner H, Vaia RA. Depletion-Induced Shape and Size Selection of Gold Nanoparticles. *Nano Letters* 2010, **10**(4)**:** 1433-1439.

53. Chen H, Sun Z, Ni W, Woo KC, Lin H-Q, Sun L*, et al*. Plasmon Coupling in Clusters Composed of Two-Dimensionally Ordered Gold Nanocubes. *Small* 2009, **5**(18)**:** 2111-2119.

Chapter 4 – Gold Nanosphere and Nanorod Homo- and Heterodimers as pH-responsive Plasmonic Actuators

4.1 Introduction

Self-assembly of nanoparticles was first reported in 1996 simultaneously by the groups of Alivisatos and Mirkin [1, 2]. Since then advances in nanoparticle synthesis regarding shape, monodispersity, and yield [3, 4, 5, 6, 7, 8] as well as DNA structural design and synthesis [9, 10, 11, 12, 13] have presented numerous opportunities in the field of programmable self-assembly through the integration of the metal nanoparticles with DNA ligands. Most often self-assemblies of metal nanoparticles result in large aggregates or agglomerations [14] as few methods exist to limit the amount of or location of the surface functionalization, resulting in full surface coverage and uncontrollable continuation of self-assembly [14, 15, 16]. Recently, it has been shown that the use of very specific DNA assemblies can be used to control how the nanoparticles are functionalized or assembled [17, 18, 19]. However, these methods require large amounts of DNA relative to the nanoparticles, making these methods difficult to use on any sort of large scale, as well as requiring specific matching of the size of the DNA motif to the nanoparticle employed. There is still a need for methods of site-specific functionalization that can lead to discrete nanoparticle self-assembly.

The creation of devices on the nanoscale represents a vastly unexplored potential in the scientific community. These nanomachines are contained within a size-scale between that of molecular and bulk material and results in greatly different properties than either. Machinery on this size-scale has the potential for sensing, drug delivery, cargo payload, and much more, all of which could be done inside of a cell interacting with proteins or organelles. Much like a modern-day factory, fully autonomous cells could be synthesized entirely out of nanoscale machinery. However, this future depends on the incorporation of multiple materials into responsive and

functional devices. One of the first steps to take would be in the creation of DNA-nanoparticle hybrid nanomachines. Nanoparticles and optical molecules have been incorporated into DNA nanomachines in the past, but the isotropic nanoparticles typically employed only serve to aid in visualization through microscopy[20, 21]. The use of anisotropic nanoparticles and the utilization of their unique shapes is a hurdle in self-assembly that currently limits most nanomachines.

The use of DNA as a material in nanoparticle self-assembly allows for programmability and specificity unmatched by other ligands. Due to the unique properties of DNA, materials responsive to external stimuli can also be created [9, 10, 22, 23, 24]. The use of stimuli-responsive materials is an important step in creating nanomachinery, and DNA-nanoparticle hybrid systems represent the most promising prospect for the future of nanomachinery. Therefore, it remains critical for advances to be made in creating discrete self-assemblies of nanoparticles, especially those involving stimuli-responsive materials.

Herein, I present a method to functionalize both isotropic and anisotropic gold nanoparticles in a site-specific manner with different DNA strands, each encoded with part of a triple helix moiety. The strands contain a complementary segment separate from the triple helix sequences that allows them to hybridize, effectively connecting two nanoparticles into a discrete dimer which will remain hybridized regardless of pH. When the conditions of the solution are changed between acidic and basic, the triple helix closes and opens, respectively, bringing the nanoparticles in closer proximity of one another, invoking plasmonic coupling that results in a shift of the UV-Vis-NIR absorbance peak. In the case of the spherical gold nanoparticle dimer, the plasmonic coupling shift results in a color change that is visible by eye. Because the nanoparticle-DNA hybrid building blocks are universal, both homodimers and heterodimers can be assembled with the nanospheres and nanorods. I demonstrate that the triple-helix response to pH is fast-acting

and completely reversible for several cycles. This approach presents a method for creating universal building blocks for nanoparticle self-assembly capable of creating discrete, novel, and interesting structures that allow for future study of nanoparticle-nanoparticle interactions and nanoparticle-DNA hybrid nanomachinery.

4.2 Results and Discussion

4.2.1 Synthesis of Encapsulated Building Blocks

To begin, gold nanorods were synthesized according to literature precedent[6]. The synthesized rods were 49 nm in length and 12 nm in width with an aspect ratio of 4.1. The purchased gold nanoparticles were measured as 22.1 nm in diameter. The gold nanoparticles and gold nanorods undergo minor spectral changes upon the partial encapsulation and again with the subsequent DNA functionalization (Figure 4.1). These small shifts can be attributed to changes to the dielectric constant of the immediate surroundings by the ligands and polymer, and these are similar to other measured shifts of ligand exchanges[25, 26].

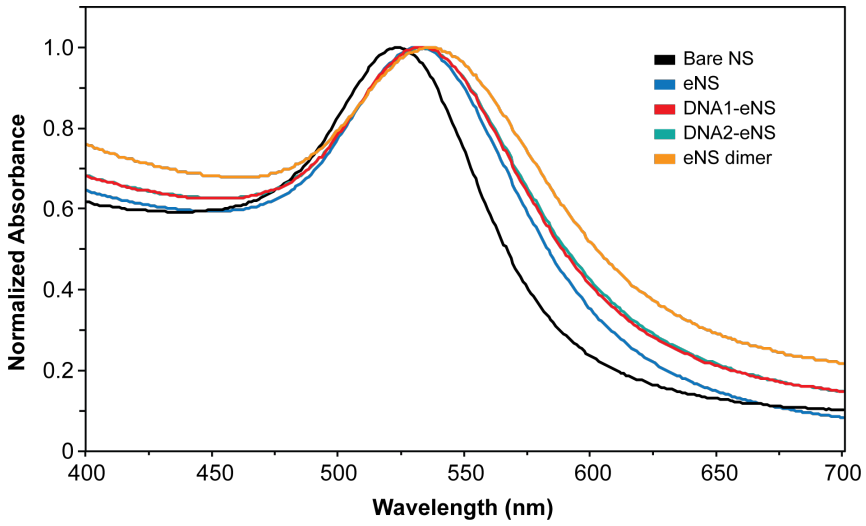

Figure 4.1 UV-Vis absorbance of AuNS building blocks and functionalized eNS Normalized absorbance spectra of all AuNS related nanoparticles are shown overlaid. The absorbance peak position changes slightly as the surrounding medium changes, in this case the ligands and the polymer.

We optimized the method of partial polymer encapsulation of gold nanoparticles and nanorods to limit the amount of exposed area to small patch of surface, as shown in Chapter 3 (Figure 3.6). The encapsulation of the nanoparticles was optimized to limit the amount of area exposed so that hybridization with multiple nanoparticles could not occur, but enough surface area was still allowed so that there would be no steric hindrance of the triple helix folding from the polymer. Gold nanorods were eccentrically encapsulated so that only one end was exposed from the polymer shell (hereby referred to as 1eNR). This encapsulation ensures that any further surface modification can only occur at the tip of the nanorod and is limited to only the singular exposed tip.

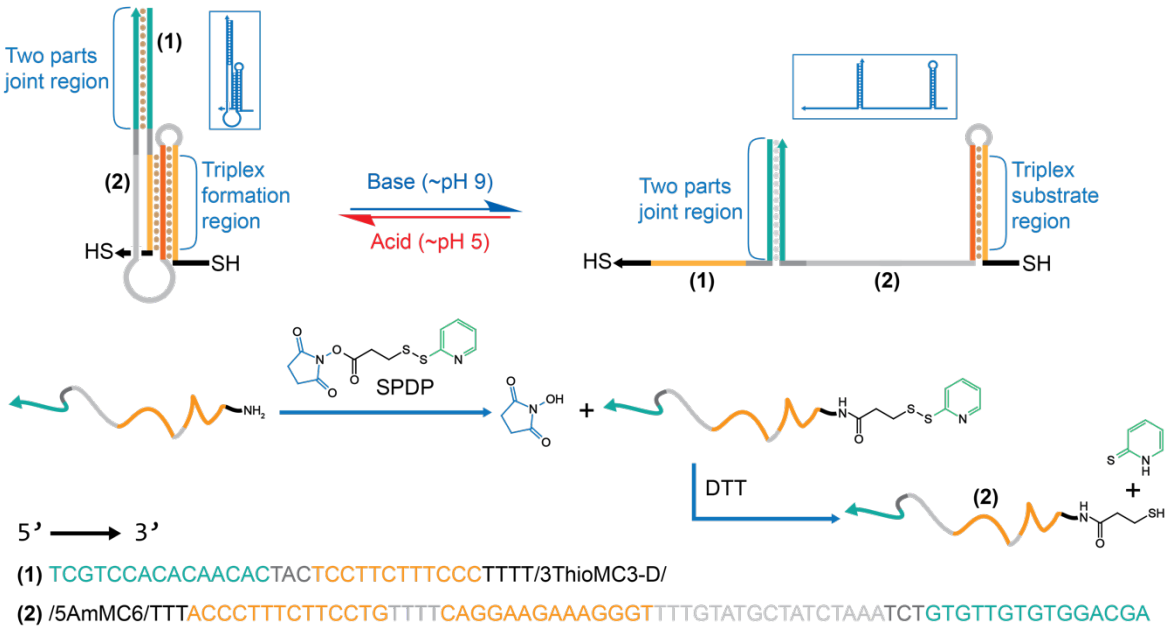

Figure 4.2 Design of the triple-helix DNA sequences capable of reversible formation The scheme of the reversible switching of the triple helix. The design was centered on keeping the strands hybridized at all times while maintaining minimal crossover between non-hybridized strands. The specific sequence for each strand are listed at the bottom.

4.2.2 Design of the DNA sequence

The DNA sequences were designed in a unique manner from those previously shown. Specifically, the design allows that sequences to remain hybridized at all times, but minimizes the possibility of triple helix formation between strands that are not already hybridized, which could cause knotting and twisting of the strands ultimately limiting the potential reversibility. Since the DNA remains at least partially hybridized at all times, the particles will be permanently tethered to one another, allowing the triple helix portion of the DNA to rapidly respond to any changes in

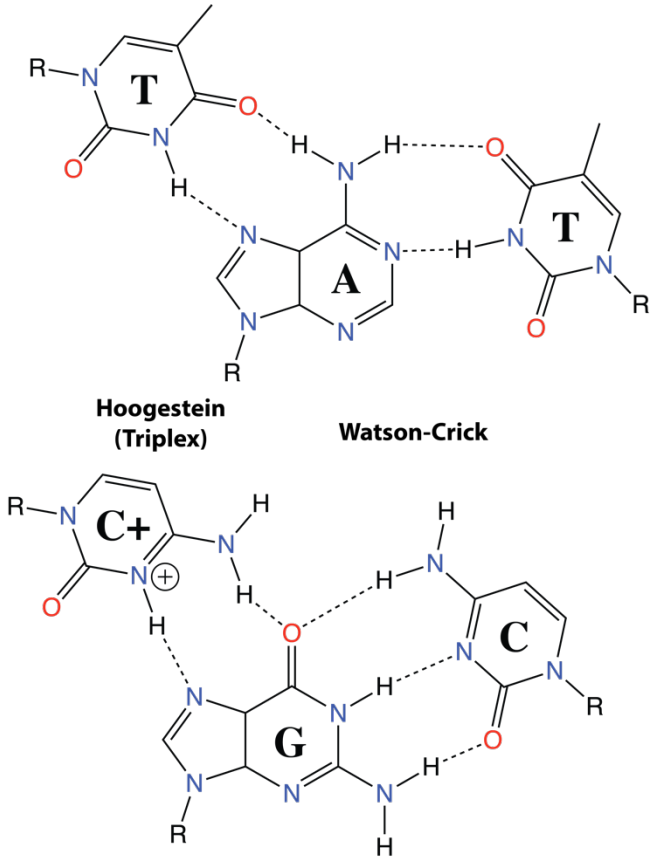

Figure 4.3 DNA base hydrogen bonding to form triplex. The hydrogen bonding is shown where the TAT and C^+GC triplets form. The TAT forms in any pH while the C^+GC triplet only forms in acidic conditions.

the solution pH. As seen in Figure 4.2, in neutral or basic conditions, the triple helix remains in the "open" conformation. In this state, the particles remain far enough apart that very little or no plasmonic coupling occurs, and the absorbance spectrum most closely reflects the spectrum of the monomeric particle. By lowering the pH of the solution to ~5, the protonation of cytosine bases allows for Hoogestein base pairing along the entirety of the triple helix sections, thus forming the "closed" conformation (Figure 4.3). When the DNA is in the closed conformation, the particles are brought well within range for plasmonic coupling to occur, causing a spectral shift of the relevant absorbance peak. These plasmonic peak shifts have been well studied and have become the basis for plasmonic rulers [27]. The pH range that the triple helix responds to is tunable through a wide range[10]. The pH range for our system was selected to respond close to neutral and biologically relevant conditions. In addition, low pH was avoided because the exterior of the polymer shell is negatively charged, and acidic conditions could neutralize this shell and cause the

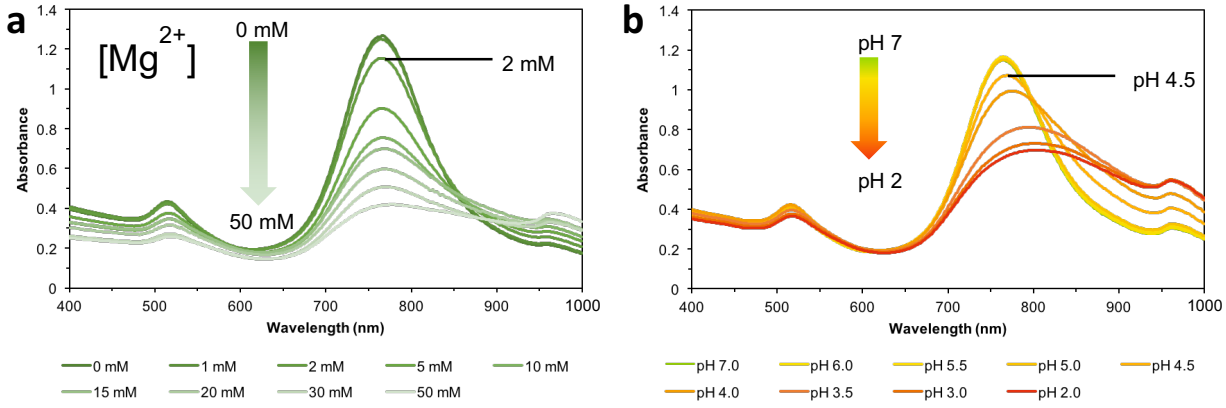

Figure 4.4 Mg^{2+} and H^{+} stability of the polyacrylic acid shell of the encapsulated nanorods a) UV-Vis-NIR absorbance spectra with increasing Mg2+ concentration in a solution. The spectrum begins to shift around 2mM concentration of Mg2+, at which point aggregation-like spectral features begin to appear. **b)** UV-Vis-NIR spectra with decreasing solution pH are shown. Spectral features common with aggregation of the nanorods begin to appear as the solution pH drops to 4.5 and below. Acidic conditions will protonate the polyacrylic acid shell, which forces the loss of electrostatic repulsion and allows hydrogen-bonding between shells.

nanoparticles to aggregate in solution. The polymer shell was shown to be stable at pH 4.5 and above (Figure 4.4), meaning the nanoparticle shells will be stable at the pH range that was selected.

4.2.3 Assembly of seNPs

Once the building blocks were obtained through partial encapsulation, further functionalization was performed using thiolated DNA strands. A modified salt aging procedure based on the one developed by Mirkin's group[28] and shown in Chapter 3 was performed to load the DNA onto the exposed surfaces of the gold nanoparticles (Figure 3.9). Because a large excess of DNA relative to particle is used in addition to the salt aging, equilibrium drives the ligand exchange process to favor the thiolated DNA strands occupying the surface. The nanoparticles were purified from the excess DNA and salt by repeated centrifugation. Hybridization of the surface DNA was performed by heating the solution to 45 °C for 15 min followed by cooling at a rate of 1 °C/min. The buffer was chosen to include a high concentration of NaCl to stabilize the compact packing of the folded triple helix DNA[16]. Mg^{2+} was found to cause irreversible aggregation of the polyanionic polymer shells (Figure 4.4) and was therefore not used in the buffer.

4.2.4 pH switching of self-assembled dimers

Once the DNA is hybridized, discrete dimers of the nanoparticles are easily accessible, as seen in Figures 4.5b, 4.7b, and 4.9b**.** Due to the simplicity and design of the building blocks, both eNS-eNS and 1eNR-1eNR homodimers as well as eNS-1eNR heterodimers can be assembled with the universal materials. With the nanoparticle dimers functionalized with the triplex-capable DNA, pH switching experiments were performed and measured by UV-Vis-NIR spectroscopy to observe the induced plasmonic coupling caused by the change in interparticle distance. In acidic conditions, the triplex folds, bringing the nanoparticles close together and inducing the plasmonic coupling. In basic conditions, the triplex unfolds allowing the DNA to open back up. The distance between

the nanoparticles when the DNA is in the open conformation is on the order of the nanoparticle diameter, large enough to minimize any plasmonic coupling and causing the UV-Vis-NIR absorbance peak to closely resemble that of the nanoparticle monomers.

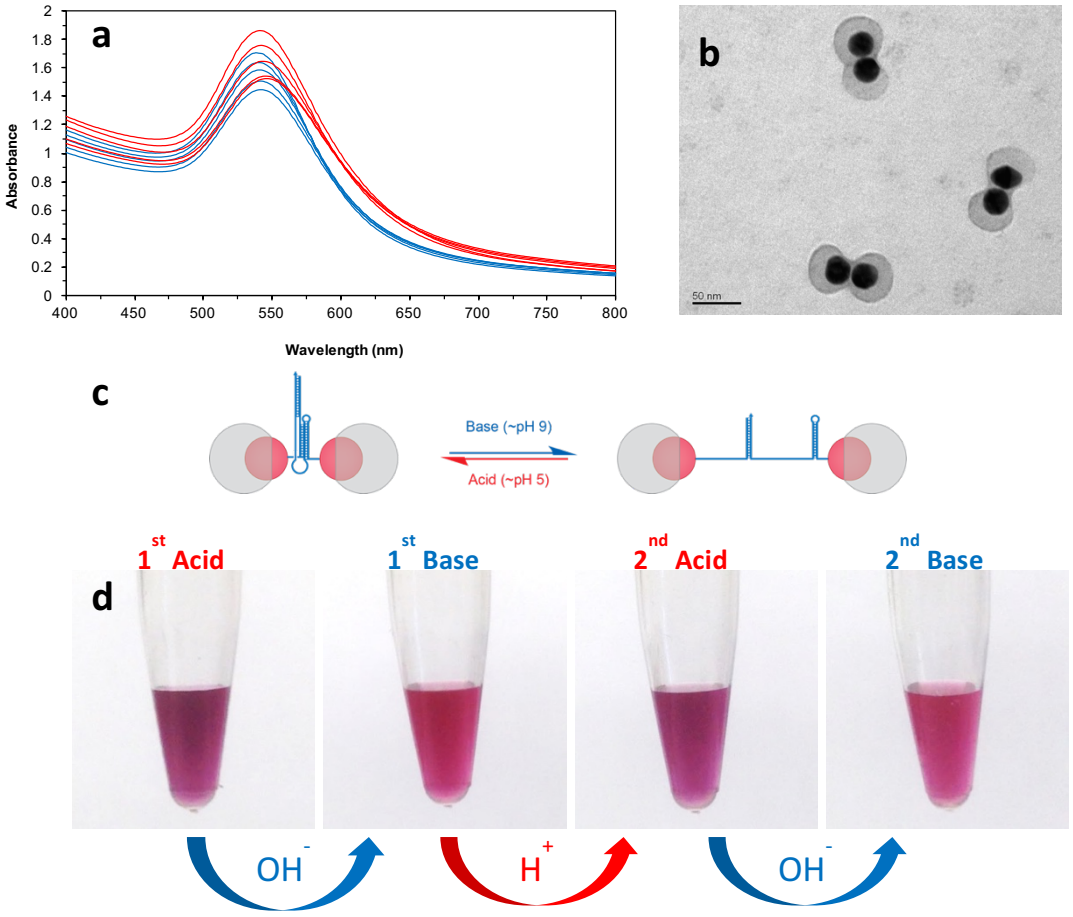

Figure 4.5 pH switching of triple helix-functionalized nanospheres a) The UV-Vis absorbance spectra of the NS dimers: pH=5 is shown in blue and pH=9 is shown in red. **b)** TEM image of the self-assembled sphere dimer. Scale bar, 50 nm. **c)** The scheme of the sphere dimer with DNA triple helix shown. **d)** The change in solution color is visible to the naked eye. The acidic solution is slightly purple in color while the basic solution is pink/red, typical of bare gold nanospheres.

The spherical gold nanoparticle dimers shown in Figure 4.5 exhibit the reversible and consistent response to changes in pH. The dimers are assembled in good yield and show an initial absorbance peak at 537 nm, which in neutral pH has the DNA in the open conformation. Addition of acid to the solution to lower the pH results in consistent shifts of the absorbance peak of three

to four nanometers as well as increased absorbance on the red side of the absorbance peak. The changes in the absorbance peak, although small, result in a visible color change, shown in Figure 4.5d. The closed conformation present in acidic presents as a red-purple color while the open conformation in basic conditions is a pink color, similar to the bare gold nanoparticles. The shift was shown to be reversible over 15 times.

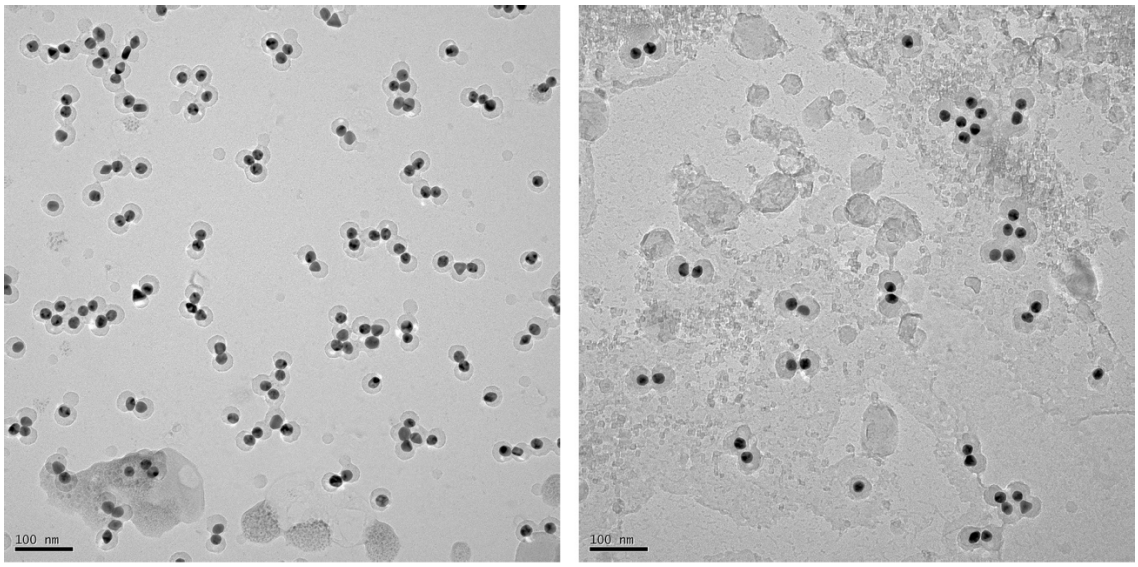

Figure 4.6 High field-of-view TEM images of eNS dimer self-assembly Scale bars, 100 nm.

The eNS building blocks were optimized to promote the formation of strictly dimers through tuning of the polymer encapsulation. In accordance with the conditions listed in Table 3.1, the conditions employed limited the exposed surface area to the smallest possible. An increase in the exposed surface area allows for the formation of self-assembled trimers, tetramers, and more, as seen in Figure 3.12d.

The sphere-rod heterodimers shown in Figure 4.7 show a difference in the peak shift in both size and location in the absorbance spectrum. Because the gold sphere is localized to the tip of the gold nanorod, the plasmonic coupling shifts the longitudinal peak of the rod. The initial

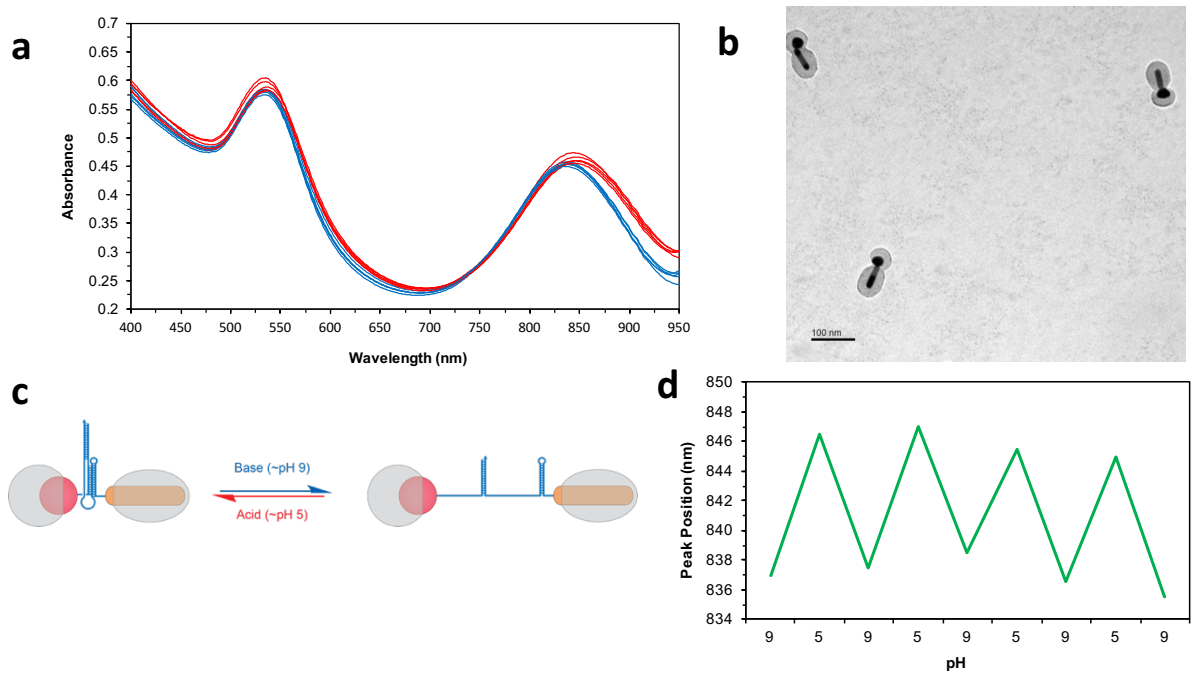

Figure 4.7 pH switching of triple helix-functionalized sphere-rod heterodimer a) The UV-Vis absorbance spectra of the heterodimers: pH=5 is shown in blue and pH=9 is shown in red. **b)** TEM image of the self-assembled heterodimer. Scale bar, 100 nm. **c)** The scheme of the sphere-rod heterodimer with DNA triple helix shown. **d)** The peak position of the longitudinal plasmon for the respective shifts. The average peak shifts are between 8 and 10 nm.

longitudinal absorbance peak is located at 837 nm, and the pH switches show consistent peak shifts between eight and ten nanometers (Figure 4.7d), over double the shift observed in the sphere dimers. The absorbance peak corresponding to both the gold spheres and transverse peak of the nanorods exhibits little change resulting from the pH switches. The majority of light waves passing through the nanosphere are unaffected by the proximity of the nanorod. Only light waves passing through both the nanosphere and the long axis of the nanorod are affected by the plasmonic coupling, which results in a very slight reduction in the overall absorbance at that peak around 530 nm (Figure 4.7a).

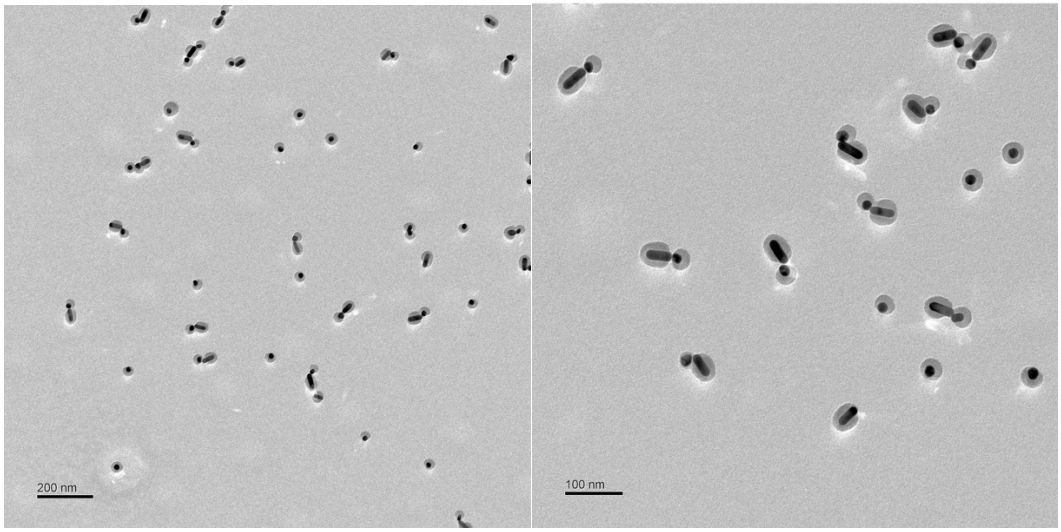

Figure 4.8 High field-of-view TEM image of 1eNR and eNS self-assembly Scale bars, left 200 nm, right 100 nm.

Similar to above with the eNS encapsulation, the 1eNR encapsulation was also optimized to limit the possibility of multiple binding modes. The desired self-assembled structure is one eNS bound to one tip of the 1eNR, so the encapsulation of the 1eNR is optimized to limit the exposed surface area to as small a region as possible so that only one eNS can bind. Similarly, the same eNS encapsulation conditions used for the eNS homodimer self-assembly are also employed for these eNS structures.

The gold nanorod homodimers shown in Figure 4.9b exhibit the most impressive shifts in absorbance peak. The initial longitudinal absorbance peak is located at 854 nm, which shifts to 941 nm upon addition of acid the first time. Reversible pH switches result in peak shifts of 80 to 90 nm consistently (Figure 4.9d). Again, only the light waves traveling through the longitudinal axis of the nanorod are affected by the proximity of the other nanorod, and thus the only absorbance shifts occur in that region of the spectrum. No observable shift occurs in the transverse peak of the spectrum, further confirming that all nanorods are linked by the tips and not through the sides.

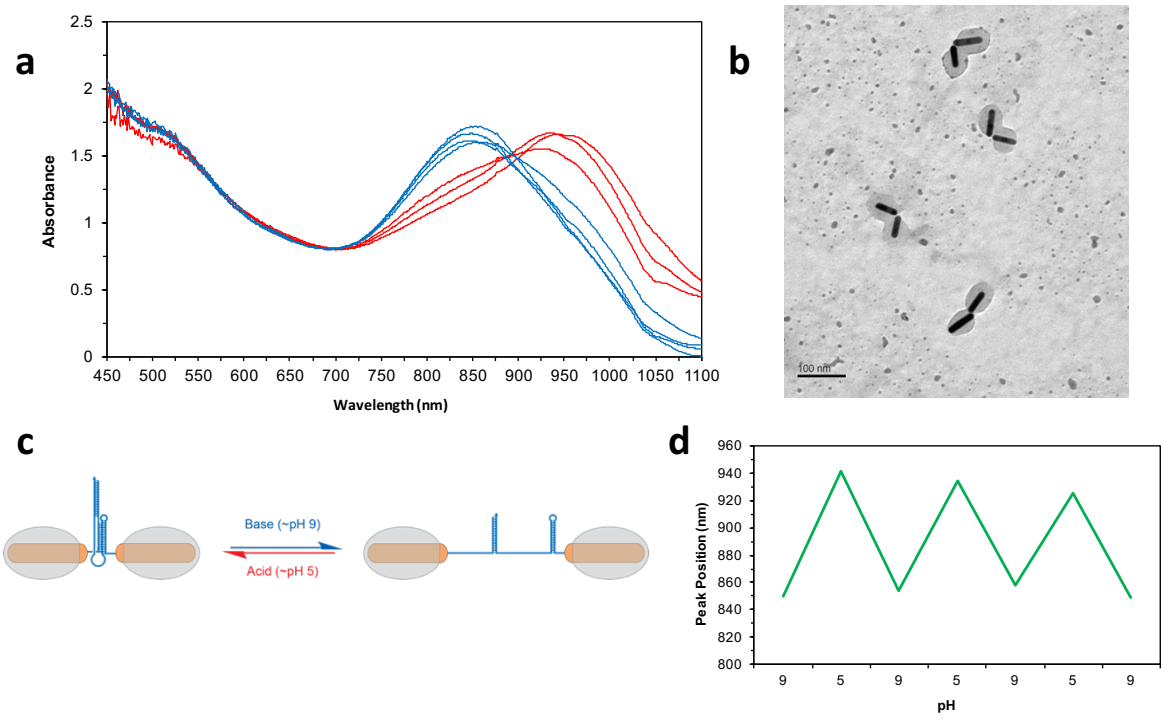

Figure 4.9 pH switching of triple helix-functionalized nanorod dimer a) The UV-Vis absorbance spectra of the nanorod dimers: pH=5 is shown in blue and pH=9 is shown in red. **b)** TEM image of the self-assembled nanorod dimer. Scale bar, 100 nm. **c)** The scheme of the nanorod dimer with DNA triple helix shown. **d)** The peak position of the longitudinal plasmon for the respective shifts. The average peak shifts are between 80 and 90 nm.

Finally, the optimization of the 1eNR encapsulation was identical to the encapsulation conditions employed above for the 1eNR-eNS heterodimer. Although the stringency of the limited exposed area is likely less in this case as the probability of multiple 1eNR binding to the tip of another 1eNR is quite low based on the steric hindrance of the bound nanoparticles, especially with the size of the polymer encapsulation. Likewise, examples of multiply-bound 1eNRs on a single tip are not present in any meaningful quantity as impurities in the TEM images.

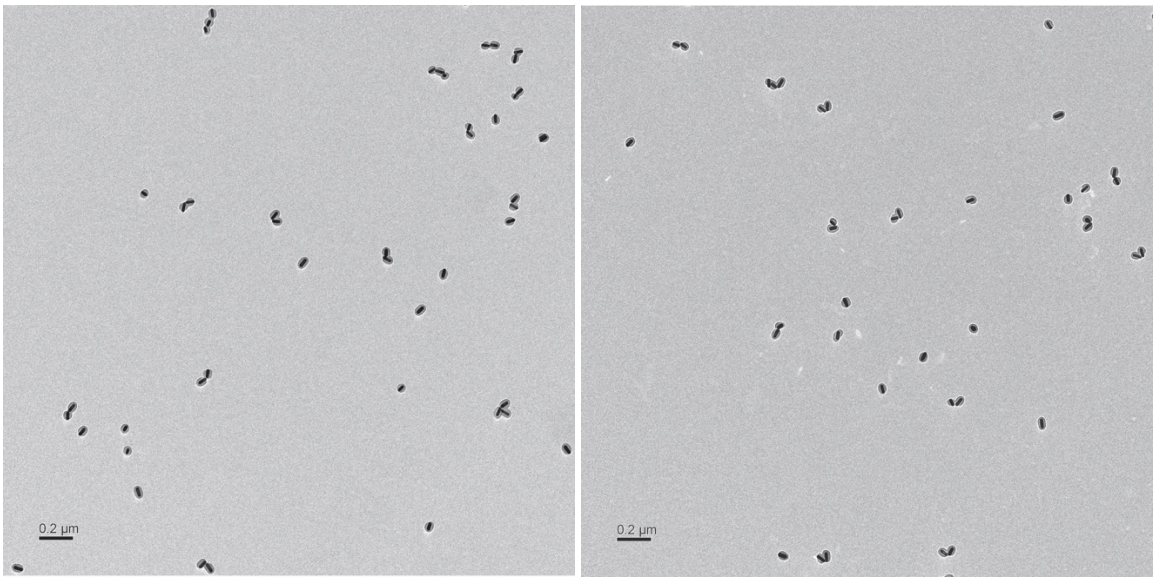

Figure 4.10 High field-of-view TEM image of 1eNR homodimer self-assembly Scale bars, 200 nm.

4.2.5 Observation of the rate of conformation switching

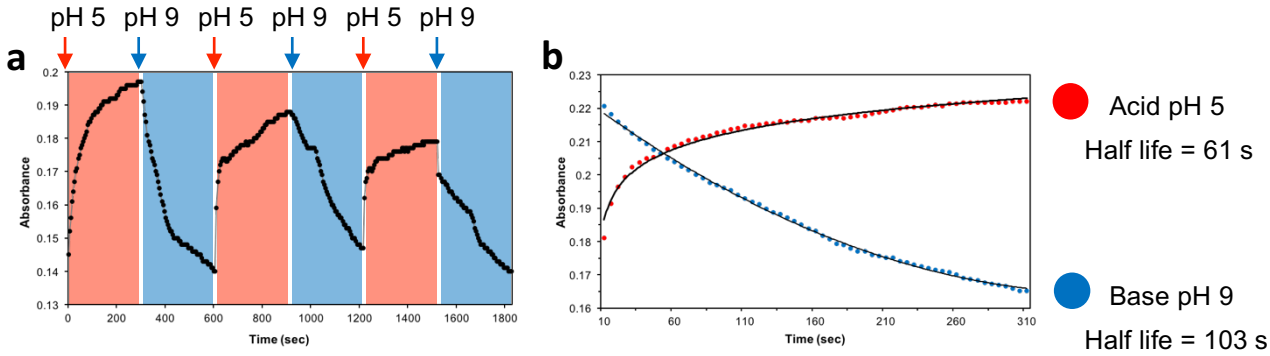

Figure 4.11 Kinetic data for the triple helix switching a) The absorbance of the acidic solution (closed conformation) nanorod dimer over time through 3 total cycles. The absorbance was measured at the 944 nm, roughly the location of the of the red longitudinal peaks from Figure 4.9a. The pH switches were performed every 250 seconds. **b)** The average values of the 3 switches from part a were plotted and fit to first-order kinetics. The half-life of each was extracted from the fit curve and is shown to the right of the graph.

The rate of the triple helix switching was also measured using UV-Vis-NIR absorbance with the 1eNR homodimer. The absorbance values at the two longitudinal peak wavelengths

(Figure 4.11a) were measured at 5 second intervals following the addition of either acid or base. The absorbance of one peak acts inversely to the absorbance of the other, so as the absorbance of one peak increases, the other peak decreases. The rate of the base-to-acid switch (closing the conformation) was found to be noticeably faster than the acid-to-base switch (opening the conformation), 61-second half-life compared to 103 seconds for the latter (Figure 4.11b). This discrepancy has been observed with other triple helix systems[9], however our nanoparticle-DNA hybrid system shows a considerably slower rate than the DNA alone. We believe this can attributed to the payload of the nanoparticles tethered to the ends of the DNA. Rather than simply waiting for the Brownian motion of the DNA strands to move close enough to form the triple helix, the

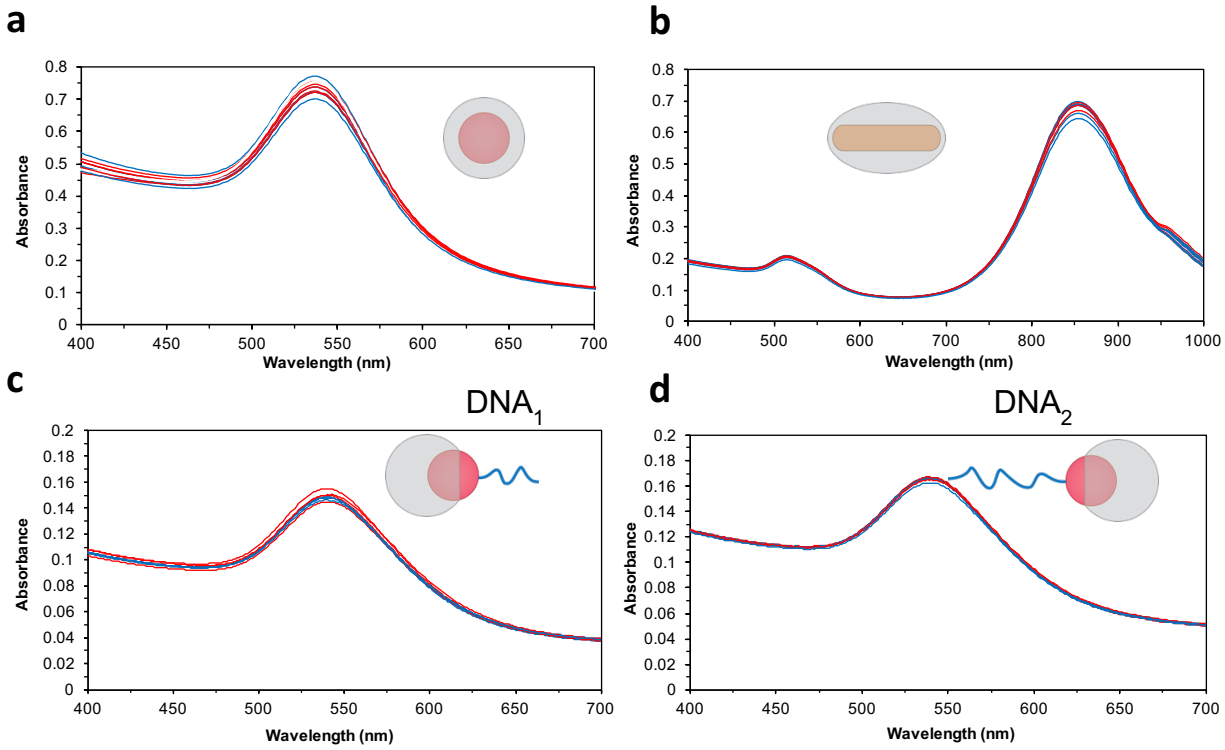

Figure 4.12 Control experiments for triple-helix functionalized nanoparticles a) pH switching experiment was performed on the fully encapsulated nanosphere. **b)** pH switching experiment was performed on the fully encapsulated nanorod. **c)** pH switching experiment was performed on eNP functionalized with DNA_1 strand. **d)** pH switching experiment was performed on eNP functionalized with DNA_2 strand.

nanoparticles have to move close enough together to allow the DNA strands to be in proximity to then form the correct conformation, which can take a couple orders of magnitude longer in this case[9]. However, it should be noted that the rate of the triple-helix DNA-nanoparticle hybrid system is still much faster than hybrid systems employing other DNA motifs[29].

4.2.6 Controls of DNA-functionalized and encapsulated nanoparticles

To confirm the triple helix moiety of the DNA sequence is solely responsible for the action of the DNA-nanoparticle hybrid spectral observation, several control experiments were performed. As mentioned above, the polyacrylic acid shell could become compromised if the solution conditions become too acidic or too electrostatic (Figure 4.4). Using both the fully-encapsulated nanorods and nanospeheres, the acid-base switching experiment was performed and the UV-Vis-NIR spectra were collected after each switch. Additionally, both DNA-functionalized nanosphere samples were also subjected to the same switching experiment individually. All spectra show unshifting peaks, which reveals that the DNA moiety is solely responsible for the peak shifts in the experiment.

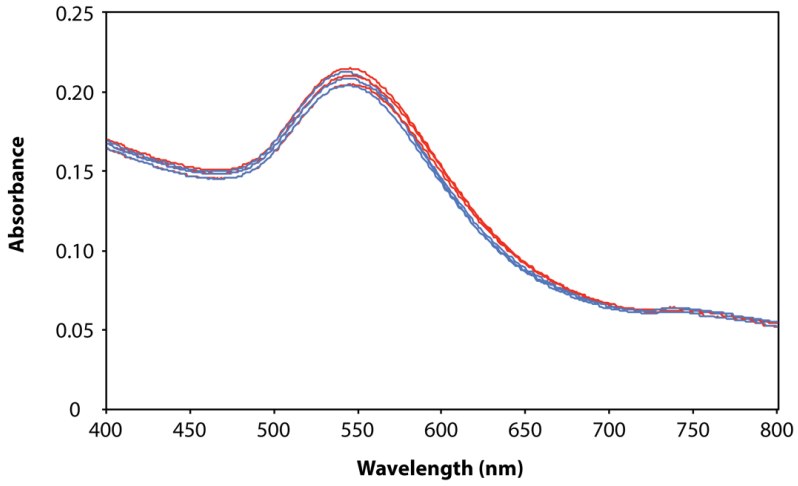

Figure 4.13 Absorbance spectrum of AuNS dimers with non-triplex active DNA AuNS with DNA ligands used in chapter 3, with no pH-responsive triplex regions. Note the lack of shift for the peak absorbance.

Additionally, a control experiment was performed where the AuNS dimers were synthesized according the procedure in chapter 3 with the DNA strands also used in chapter 3. The strands contain only a poly-T segment 10 bps long and a 15-bp complementary region. No portion of the DNA strand is pH responsive and should elicit no conformational changes in acidic or basic solution. Accordingly, as shown in Figure 4.13, there is no change in the absorbance spectrum in changing pH, further confirming the action of the DNA on the triplex-functionalized dimer.

4.2.7 Conclusions

Here we demonstrated a new synthetic strategy for the creation of discrete nanoparticle dimers, including the localization of spherical gold nanoparticles and gold nanorods to the tip of another gold nanorod. This was accomplished by a partial encapsulation process using a diblock copolymer in the presence of both a hydrophobic and a hydrophilic ligand. The exposed surface remaining on the partially encapsulated nanoparticles were then functionalized with DNA sequences coded with a triple helix moiety that responds to solution pH between 5 and 9. With the nanoparticle homo- and heterodimers, the optical response to the plasmonic coupling, as controlled by the solution pH, was measured with UV-Vis-NIR spectroscopy. Highly reversible and consistent peak shifts were observed in the sphere dimers, the rod dimers, and the sphere-rod heterodimer with the largest peak shifts of 80-90 nm being present in the nanorod homodimer. The partial encapsulation method enabling site-specific functionalization and discrete self-assembly will allow future studies of nanoparticle interactions, including field enhancement effects and plasmonic coupling between different noble metals and quantum dots.

4.3 Methods

4.3.1 Synthesis and encapsulation of nanoparticles

All syntheses and encapsulations were performed according to the procedures in Section 3.4. Encapsulations were optimized to minimize the exposed surface area of the gold, in accordance to the conditions listed in Table 3.1.

4.3.2 Reduction of the thiolated DNA

The DNA was purchased with a terminal disulfide modification. To 30 μl of a 100 μM stock solution of the DNA was added 30 μl of a freshly prepared 100 mM solution of DTT in nanopure H_2O. The solution was wrapped in foil and gently shaken at room temperature for 1 h. The reduced DNA was then purified in a NAP5 column with the fractions collected in a 96-well plate. The absorbance measured at 260 nm was used to determine the fractions containing the DNA.

4.3.3 Functionalization of the nanoparticles with thiolated DNA

To a concentrated solution of the partially encapsulated gold nanoparticles was added an amount of the reduced thiolated DNA in an amount where the DNA:nanoparticle ratio was roughly 400:1. The solution was gently shaken at room temperature for 2 h. After 2 h, a salt-aging procedure modified from the Mirkin group was used to ensure efficient and complete packing of the DNA onto the exposed surface.[28] Amounts of 400 mM NaCl, 0.01% SDS, pH=9 solution were added to the solution. Six additions were performed, each separated by 15 min, to raise the concentration of NaCl in solution to about 200 mM total. After the final addition, the solution was left to shake at room temperature overnight. To remove the excess DNA, the solution was centrifuged 5 times at 9,000 g for 10 min and washed with 0.01% SDS, pH=9 solution.

4.3.4 Self-assembly of the DNA-functionalized nanoparticles

UV-Vis was used to determine the relative concentrations of each NP-DNA solution. An equal molar amount of each solution was mixed in a centrifuge tube. An equal volume of 600 mM NaCl, 0.2x TAE buffer was added to the sample to give a final concentration of 300 mM NaCl, 0.1x TAE with a pH around 8. The sample was heated to 45 °C for 15 min and then cooled by 1 °C/min until the temperature reached 15 °C to allow complete hybridization.

4.3.5 pH switching experiments

To 50 μl of the self-assembled NP solution, volumes of 0.1 M HCl and NaOH were added. The solution was kept in a well of 96-well plate for a Synergy H4 microplate spectrophotometer. Upon addition of acid or base, the solution was gently mixed for a few seconds and allowed 5 minutes to equilibrate before obtaining the absorbance spectrum.

4.4 References

1. Alivisatos AP, Johnsson KP, Peng X, Wilson TE, Loweth CJ, Bruchez Jr MP, *et al*. Organization of'nanocrystal molecules' using DNA. *Nature* 1996, **382**(6592)**:** 609-611.

2. Mirkin CA, Letsinger RL, Mucic RC, Storhoff JJ. A DNA-based method for rationally assembling nanoparticles into macroscopic materials. *Nature* 1996, **382**(6592)**:** 607-609.

3. Lee J-H, Gibson KJ, Chen G, Weizmann Y. Bipyramid-templated synthesis of monodisperse anisotropic gold nanocrystals. *Nature communications* 2015, **6**.

4. Liu M, Guyot-Sionnest P. Mechanism of silver (I)-assisted growth of gold nanorods and bipyramids. *The Journal of Physical Chemistry B* 2005, **109**(47)**:** 22192-22200.

5. Jana NR, Gearheart L, Murphy CJ. Wet Chemical Synthesis of High Aspect Ratio Cylindrical Gold Nanorods. *The Journal of Physical Chemistry B* 2001, **105**(19)**:** 4065-4067.

6. Nikoobakht B, El-Sayed MA. Preparation and Growth Mechanism of Gold Nanorods (NRs) Using Seed-Mediated Growth Method. *Chemistry of Materials* 2003, **15**(10)**:** 1957-1962.

7. Scarabelli L, Coronado-Puchau M, Giner-Casares JJ, Langer J, Liz-Marzán LM. Monodisperse Gold Nanotriangles: Size Control, Large-Scale Self-Assembly, and Performance in Surface-Enhanced Raman Scattering. *ACS Nano* 2014, **8**(6)**:** 5833-5842.

8. Sau TK, Murphy CJ. Room Temperature, High-Yield Synthesis of Multiple Shapes of Gold Nanoparticles in Aqueous Solution. *Journal of the American Chemical Society* 2004, **126**(28)**:** 8648-8649.

9. Iacovelli F, Idili A, Benincasa A, Mariottini D, Ottaviani A, Falconi M, *et al*. Simulative and Experimental Characterization of a pH-Dependent Clamp-like DNA Triple-Helix Nanoswitch. *Journal of the American Chemical Society* 2017, **139**(15)**:** 5321-5329.

10. Idili A, Vallée-Bélisle A, Ricci F. Programmable pH-Triggered DNA Nanoswitches. *Journal of the American Chemical Society* 2014, **136**(16)**:** 5836-5839.

11. Liu D, Chen G, Akhter U, Cronin TM, Weizmann Y. Creating complex molecular topologies by configuring DNA four-way junctions. *Nat Chem* 2016, **8**(10)**:** 907-914.

12. Rothemund PWK. Folding DNA to create nanoscale shapes and patterns. *Nature* 2006, **440**(7082)**:** 297-302.

13. Seeman NC. DNA in a material world. *Nature* 2003, **421**(6921)**:** 427-431.

14. Auyeung E, Li TI, Senesi AJ, Schmucker AL, Pals BC, de La Cruz MO, *et al*. DNA-mediated nanoparticle crystallization into Wulff polyhedra. *Nature* 2014, **505**(7481)**:** 73-77.

15. Li Z, Mirkin CA. G-quartet-induced nanoparticle assembly. *Journal of the American Chemical Society* 2005, **127**(33)**:** 11568-11569.

16. Chen Y, Mao C. pH-Induced Reversible Expansion/Contraction of Gold Nanoparticle Aggregates. *Small* 2008, **4**(12)**:** 2191-2194.

17. Li Y, Liu Z, Yu G, Jiang W, Mao C. Self-Assembly of Molecule-like Nanoparticle Clusters Directed by DNA Nanocages. *Journal of the American Chemical Society* 2015, **137**(13)**:** 4320-4323.

18. Shen C, Lan X, Lu X, Meyer TA, Ni W, Ke Y, *et al*. Site-Specific Surface Functionalization of Gold Nanorods Using DNA Origami Clamps. *Journal of the American Chemical Society* 2016, **138**(6)**:** 1764-1767.

19. Pal S, Deng Z, Ding B, Yan H, Liu Y. DNA-Origami-Directed Self-Assembly of Discrete Silver-Nanoparticle Architectures. *Angewandte Chemie International Edition* 2010, **122**(15)**:** 2760-2764.

20. Shimron S, Cecconello A, Lu C-H, Willner I. Metal nanoparticle-functionalized DNA tweezers: from mechanically programmed nanostructures to switchable fluorescence properties. *Nano letters* 2013, **13**(8)**:** 3791-3795.

21. Wang Z-G, Elbaz J, Willner I. DNA machines: bipedal walker and stepper. *Nano letters* 2010, **11**(1)**:** 304-309.

22. Pelossof G, Tel-Vered R, Liu XQ, Willner I. Amplified Surface Plasmon Resonance Based DNA Biosensors, Aptasensors, and Hg2+ Sensors Using Hemin/G-Quadruplexes and Au Nanoparticles. *Chemistry–A European Journal* 2011, **17**(32)**:** 8904-8912.

23. Wang C, Du Y, Wu Q, Xuan S, Zhou J, Song J, *et al*. Stimuli-responsive plasmonic core–satellite assemblies: i-motif DNA linker enabled intracellular pH sensing. *Chemical Communications* 2013, **49**(51)**:** 5739-5741.

24. Cheglakov Z, Weizmann Y, Basnar B, Willner I. Diagnosing viruses by the rolling circle amplified synthesis of DNAzymes. *Organic & biomolecular chemistry* 2007, **5**(2)**:** 223-225.

25. Malachosky EW, Guyot-Sionnest P. Gold Bipyramid Nanoparticle Dimers. *The Journal of Physical Chemistry C* 2014, **118**(12)**:** 6405-6412.

26. Gole A, Murphy CJ. Azide-derivatized gold nanorods: functional materials for "click" chemistry. *Langmuir* 2008, **24**(1)**:** 266-272.

27. Sönnichsen C, Reinhard BM, Liphardt J, Alivisatos AP. A molecular ruler based on plasmon coupling of single gold and silver nanoparticles. *Nature biotechnology* 2005, **23**(6)**:** 741-745.

28. Hurst SJ, Lytton-Jean AK, Mirkin CA. Maximizing DNA loading on a range of gold nanoparticle sizes. *Analytical chemistry* 2006, **78**(24)**:** 8313-8318.

29. Wang W, Liu H, Liu D, Xu Y, Yang, Zhou D. Use of the Interparticle i-Motif for the Controlled Assembly of Gold Nanoparticles. *Langmuir* 2007, **23**(24)**:** 11956-11959.

Chapter 5 – Concluding Thoughts

5.1 Summary of the body of work

The work presented within this thesis can be divided into two main topics: advancements in synthetic procedures to develop novel gold nanostructures with very high purity and monodispersity and new methodology to controllably functionalize nanoparticles in a site-specific manner allowing for unprecedented control over discrete, programmable self-assemblies. In chapter, I discussed the application of BDAC surfactant to purify bipyramid nanoparticles that had not been previously possible to purify with existing purification techniques. The use of BDAC surfactant is non-destructive to the nanoparticle and capable of purifying the desired shape to >99% in some cases. Synthetic techniques have since shown capable of producing shape purity in excess of 90%, but this purity still falls short of desirable for many applications. In addition, I've shown the use of the bipyramid as a platform for further nanoparticle growth shows a variety of novel structures as well as valuable insight into the use of different surfactants as growth conditions, utilizing their different binding affinities to exploit localized and controlled growth.

In chapter 3, I show a method of partial polymer encapsulation of nanoparticles to generate localized and directional functionalization of the nanoparticles. The encapsulation uses a dual-ligand functionalization in the presence of a diblock copolymer in a binary solvent system to control the location of the polymer and total surface coverage on the nanoparticle. A subsequent surface functionalization with thiolated ssDNA yields a nanoparticle with localized and directional binding as well as yielding complete specificity from the DNA. The building blocks obtained through the partial polymer encapsulation include several shapes with different binding modes, and the empirical method can be applied across many more nanoparticles of varying shape, size, and composition.

Furthermore, the DNA-functionalized partially-encapsulated nanoparticles can be self-assembled into preconceived structures. I show an array of 24 nanoassemblies, most of which are not possible by any other published method. The self-assemblies shown are also only a selection of what is possible by our method. Any permutation of the partially-encapsulated nanoparticles can be combined into a self-assembly.

Finally, in chapter 4, I show that the self-assemblies can be used as nanomachinery, capable of eliciting specific responses to external stimuli, that are both consistent and reversible. Likewise, any permutation of the above self-assemblies could be combined with the use of triplex DNA to create nanomachinery, which provides a platform for further studies of nanoparticle interactions.

5.2 Perspective of work within the greater context of the field

As technology advances, there is an obvious trend toward smaller and more powerful devices. This forces the conclusion that control over materials at smaller size scales is imperative for future developments within the field. The creation of useful devices in any size scale is dependent on two things: the use of a high-quality material and reliable and consistent assembly of the constituent pieces. Analogously, my research is focused on improved synthetic techniques to create high purity and highly monodisperse nanomaterials as well as improving the methods available to assembling these materials in highly controllable, consistent, and useful ways.

A huge proportion of the community has devoted themselves to the improvement of synthetic techniques for nanoparticles. The number of publications over the past two decades has exploded with advancements made across all aspects of synthesis, improving size, shape, purity, metallic makeup, and optical and catalytic properties[1,2]. These synthetic improvements cover every possible aspect of synthesis from conditions to reagents to additives to post-synthesis processing. My work specifically looked, in some degree, at all of these parts. Ideally, the synthetic technique

alone would produce 100% shape purity of any nanoparticle, but this is not always the case. Most syntheses will produce some quantity of unwanted impurities, and the ability to remove these to yield a pure product is a hallmark of chemistry. Purification by depletion flocculation is, I believe, a powerful tool in nanomaterial chemistry. While having a theoretical model as well as a few publications showing the power of depletion as a purification technique[3, 4], it still represents a largely unexplored space. The model is not perfect, and its application to somewhat complex shapes, such as bipyramids, is lacking. The model assumes that close-packing between the nanoparticles will most efficiently create the flocculate. However, close-packing of bipyramids is not a simple geometry and is most likely not the process by which these nanoparticles flocculate. There is a need for greater study into these processes and the forces that govern them in order for there to be a greater application of depletion as a purification technique for nanoparticles of complex shape.

Furthermore, there are many methods available for self-assembling nanoparticles. Many techniques lack the specificity to do discrete self-assemblies, simply coating the nanoparticle in a ligand and allowing the nanoparticles to create large-scale agglomerates. These structures can be highly periodic and provide plenty of insight into nanoparticle interactions[5]. In addition, highly complex DNA structures can be used to assemble nanoparticles through a variety of methods. But these techniques require a huge amount of DNA as the DNA confers all the directionality to the nanoparticle[6, 7]. Essentially, the assembly is a DNA assembly with nanoparticles anchored to it. These assemblies are not conducive to large-scale reactions as DNA is typically used in nanogram quantities, which is not a quantity typically allowable for bulk reactions. In addition, DNA assemblies are typically very size-specific whereas nanoparticle syntheses typically have monodispersities on an appreciable size scale that may not accommodate the DNA for all

nanoparticles in a given synthesis. Furthermore, a designed DNA structure would have to be changed to accommodate any other nanoparticle size and shape, making any minor changes to the nanoparticles have much more complex implications from the DNA standpoint. This is starkly contrasted to the work presented here, where changing the nanoparticle might require minor changes to the encapsulation procedure, slight changes to the ligand ratio or solvent ratio, but all steps further down the procedure remain the same.

5.3 Future directions for improvements to nanoparticle syntheses

The field of nanoparticle synthesis has made a lot of advances in the last decade, and therefore it is challenging to find areas in which meaningful and impactful advancements can be made. Nanoparticle syntheses are all limited, however, in one very specific factor: all wet synthetic methods to produce nanoparticles create shapes that have symmetry element. That is, it is not feasible to create nanoparticles that have two distinct sides with no symmetry, also referred to in literature as Janus particles[8]. There are methods to create Janus-like nanoparticles through the functionalization of the surface using things like oil-water interface[9, 10]. The segregation of ligands into the two phases and the isolation of nanoparticles at the interface between them causes functionalization on both sides.

However, to consider having a dual metal nanoparticle with the two metals on distinct sides, segregated, and still capable of synthesizing discrete and monodisperse structures is very difficult. If we were to consider our polymer-encapsulated structures, however, it is easy to see how one might overgrow a secondary metal onto the surfaces exposed from the polymer. Similar systems already exist[11, 12, 13], mostly with spherical nanoparticles as more complex geometries with anisotropic nanoparticles were previously not shown before our method.

We can now see that synthesizing gold nanorods with one end exposed can be done with incredibly high yield. With that structure, it may be possible to grow a rod structure extending off of the original rod but with a different metal. For example, there are a class of microparticles known as micromotors from the group of Joseph Wang[14, 15, 16]. These microparticles are binary rods with one side gold and the other platinum. These motors are so called because, when exposed to hydrogen peroxide, a redox reaction occurs that provides thrust to the nanorod that always moves the motor in the direction of the gold to the platinum.

Beyond that, the realm of nanoparticle interactions goes far beyond the plasmonic coupling that was discussed at length within this thesis. Direct contact between two metals provides an even more intense interaction between the nanoparticles. So overgrowth on the nanoparticle surface can be a powerful method to fine-tune properties of the nanoparticle to exact desired specifications. Now, with the partial-encapsulated structures, we could look to grow whole new classes of multi-metal nanoparticles on any of the shapes we have encapsulated thus far.

5.4 Future directions for programmable self-assembly

The work of partial polymer encapsulation leading to programmable self-assembly is a significant advancement in the field with several new and interesting developments. However, with this project especially, there are many possible directions of research that could arise from this work.

First, as was discussed in part in section 3.2.4, there are so many possibilities available for encapsulation of other nanoparticles. In this work, it was shown that Au spheres, rods, cubes, and triangles could be partially encapsulated and this was also extended to Pd cubes, showing that other compositions could behave in a similar manner. It was discussed how changes in the polymer size could prove useful in extension of the encapsulation to nanoparticles of differing shape and

especially of different size. Likewise, it seems hopeful that partial encapsulation could extend to nanoparticles of any composition. The change from gold to palladium did require the use of a different hydrophilic ligand. Similarly, changing the composition to another metal or semiconductor material would result in vastly different surface chemistries, which could very likely require the use of different hydrophilic and hydrophobic ligands. However, the concept of partial polymer encapsulation to block the surface of the nanoparticle to grant directionality and specificity would still remain despite the changes to the actual surface chemistry.

Furthermore, the entirety of the self-assembly projects was done with ssDNA, but any ligand sufficient in undergoing the ligand exchange process could be used to functionalize the nanoparticle surface. These ligands could include biological molecules and polymers and could be used to drive directional and site-specific self-assembly in unprecedented ways, including the creation of new stimuli-responsive materials.

Finally, the methodology presented could also be extended to create discrete assemblies of plasmonic-excitonic nanoparticles. It has been documented that the effect of a plasmonic nanoparticle on a fluorophore coating the surface results in longer radiative decay processes and decreased photobleaching rates, both of which plague all fluorophores, including quantum dots[17]. In addition, the bipyramid was shown to actually increase the emission of the fluorophore. The ability to localize the fluorophore solely to the tip of a bipyramid or nanorod could even further enhance these properties, but until now, the site-specific functionalization needed for such measurements was not possible. I believe we now have the tools to do solution-based self-assembly of gold nanoparticle-quantum dot binary systems, which could enable some really interesting studies in the future.

5.5 Concluding Remarks

The field of nanotechnology and nanomaterials has rapidly evolved over the last few decades. Many of the discoveries and advancements have been brought to the forefront of everyday life. It has been exciting to follow the field so closely over the last few years and even play a role in it by publishing the work I have been able to be a part of. I look forward to seeing my career takes me within this field and how far these projects in particular push the limits.

5.6 References

1. Eustis S, El-Sayed MA. Why gold nanoparticles are more precious than pretty gold: noble metal surface plasmon resonance and its enhancement of the radiative and nonradiative properties of nanocrystals of different shapes. *Chemical society reviews* 2006, **35**(3)**:** 209-217.

2. Daniel M-C, Astruc D. Gold nanoparticles: assembly, supramolecular chemistry, quantum-size-related properties, and applications toward biology, catalysis, and nanotechnology. *Chemical reviews* 2004, **104**(1)**:** 293-346.

3. Park K, Koerner H, Vaia RA. Depletion-induced shape and size selection of gold nanoparticles. *Nano letters* 2010, **10**(4)**:** 1433-1439.

4. Asakura S, Oosawa F. On interaction between two bodies immersed in a solution of macromolecules. *The Journal of Chemical Physics* 1954, **22**(7)**:** 1255-1256.

5. Auyeung E, Li TI, Senesi AJ, Schmucker AL, Pals BC, de La Cruz MO*, et al*. DNA-mediated nanoparticle crystallization into Wulff polyhedra. *Nature* 2014, **505**(7481)**:** 73-77.

6. Tian Y, Zhang Y, Wang T, Xin HL, Li H, Gang O. Lattice engineering through nanoparticle–DNA frameworks. *Nature materials* 2016, **15**(6)**:** 654.

7. Lu F, Yager KG, Zhang Y, Xin H, Gang O. Superlattices assembled through shape-induced directional binding. *Nature communications* 2015, **6:** 6912.

8. Lattuada M, Hatton TA. Synthesis, properties and applications of Janus nanoparticles. *Nano Today* 2011, **6**(3)**:** 286-308.

9. Perro A, Reculusa S, Ravaine S, Bourgeat-Lami E, Duguet E. Design and synthesis of Janus micro-and nanoparticles. *Journal of materials chemistry* 2005, **15**(35-36)**:** 3745-3760.

10. Perro A, Meunier F, Schmitt V, Ravaine S. Production of large quantities of “Janus” nanoparticles using wax-in-water emulsions. *Colloids and Surfaces A: Physicochemical and Engineering Aspects* 2009, **332**(1)**:** 57-62.

11. Choueiri RM, Galati E, Thérien-Aubin H, Klinkova A, Larin EM, Querejeta-Fernández A, *et al*. Surface patterning of nanoparticles with polymer patches. *Nature* 2016, **538:** 79.

12. Galati E, Tebbe M, Querejeta-Fernández A, Xin HL, Gang O, Zhulina EB, *et al*. Shape-Specific Patterning of Polymer-Functionalized Nanoparticles. *ACS nano* 2017, **11**(5)**:** 4995-5002.

13. Liu B, Thanneeru S, Lopes A, Jin L, McCabe M, He J. Surface Engineering of Spherical Metal Nanoparticles with Polymers toward Selective Asymmetric Synthesis of Nanobowls and Janus-Type Dimers. *small* 2017, **13**(20)**:** 1700091.

14. Gao W, Pei A, Wang J. Water-driven micromotors. *ACS nano* 2012, **6**(9)**:** 8432-8438.

15. Gao W, Pei A, Feng X, Hennessy C, Wang J. Organized self-assembly of Janus micromotors with hydrophobic hemispheres. *Journal of the American Chemical Society* 2013, **135**(3)**:** 998-1001.

16. Gao W, D'Agostino M, Garcia-Gradilla V, Orozco J, Wang J. Multi-fuel driven janus micromotors. *Small* 2013, **9**(3)**:** 467-471.

17. Navarro J, Lerouge F, Micouin G, Cepraga C, Favier A, Charreyre M-T, *et al*. Plasmonic bipyramids for fluorescence enhancement and protection against photobleaching. *Nanoscale* 2014, **6**(10)**:** 5138-5145.